Escuela Politécnica Superior de Jaén
Máster Universitario en Ingeniería Industrial

UNIVERSIDAD DE JAÉN
Escuela Politécnica Superior (Jaén)

Trabajo Fin de Máster

BUBBLE DYNAMICS IN COMPLEX FLOWS: EFFECT OF A SOLID SURFACE ON THE RISING MOVEMENT

Alumna: Estepa Cantero, Cecilia

Tutora: Prof. D. Rocío Bolaños Jiménez
Dpto.: Departamento de Ingeniería Mecánica y Minera, Área de Mecánica de Fluidos

Septiembre, 2021

Universidad de Jaén
Escuela Politécnica Superior de Jaén
Departamento de Ingeniería Mecánica y Minera
Área de Mecánica de Fluidos

Doña Rocío Bolaños Jiménez, tutora del Proyecto Fin de Máster titulado: Bubble dynamics in complex flows: effect of a solid surface on the rising movement, que presenta Cecilia Estepa Cantero, autoriza su presentación para defensa y evaluación en la Escuela Politécnica Superior de Jaén.

Jaén, septiembre de 2021

La alumna:

Cecilia Estepa Cantero

ESTEPA CANTERO CECILIA - 77376258A

Firmado digitalmente por ESTEPA CANTERO CECILIA - 77376258A
Fecha: 2021.09.05 18:04:31 +02'00'

La tutora:

Rocío Bolaños Jiménez

BOLAÑOS JIMENEZ MARIA ROCIO - 77329190Q

Firmado digitalmente por BOLAÑOS JIMENEZ MARIA ROCIO - 77329190Q
Fecha: 2021.09.05 18:07:06 +02'00'

Content

List of figures

Figures chapter 1

Figures chapter 2

Figures chapter 3

Figures chapter 4

List of tables

Tables chapter 3

Tables chapter 4

1. INTRODUCTION

This study aims to analyse the rising movement of a bubble and how it may be modified due to its interaction with solid vertical walls. The problem of a freely rising bubble inside a quiescent liquid has been widely studied previously. However, the presence of such walls may cause complex changes in the bubble's trajectory by inducing a force that is determining for its position. In this case, Galileo and Bond numbers (Ga and Bo respectively) are to be considered, as well as the influence of a separation parameter L^*.

1.1. Motivation

The topic which this study addresses is of great interest both in industrial and medical applications. Hence multiple works have been developed in the last decades concerning the dynamics of bubble formation, movement and collapse [1]. Bubbles size distribution and their movement govern mass transfer processes in many industrial operations involved in food, chemical, material, biomedical or pharmaceutical industries among many others [2]. In particular, the knowledge of their dynamics inside complex flows has special significance in the fields of engineering (fuel synthesis [3], polymerization [4], reactors aeration [5]) or medicine (ultrasounds applications [6], in-body drug transportation [7]).

These processes might be optimized if the path of the bubbles could be precisely predicted. However, flow conditions in these applications are commonly complex and convey interference among bubbles, with solid surfaces or shear flows. For instance, bubble interference may affect nucleation boiling processes [8] and shear flows are relevant to industrial lubricating fluids confined to ultrathin molecular layers or natural phenomena such as waterfalls [9] – [10] because if the shear is strong enough, it can deform the bubble, and the feedback of this deformation on the hydrodynamic forces may be very important [11]. Many phenomena involving these conditions are critically relevant for the aforementioned applications, although they have not been accurately explored yet, thus cannot be successfully implemented.

Consequently, this work has the purpose to extend previous studies where the bubble could rise freely by studying the effect of the presence of a vertical wall to the different regimes previously observed. These regimes have been found to happen within specific values of bubble size and fluid properties, which can be summarized mainly by two dimensionless parameters: Galileo (Ga) and Bond (Bo) numbers. In this manner, paths for rectilinear and planar zigzagging rising bubbles (those which happen for high values of Ga and low values of Bo) as well as three-dimensional spiral regimes (for high values of Ga and Bo) have been precisely characterized and will be held as reference when introducing a wall in the proximity of the rising path. Thereby, the influence of the wall will be characterized also for different regimes through the Ga-Bo plane, adding a necessary wall distance parameter (L^*). This study will act as the natural continuation of previous investigations that leaded to the author's undergraduate thesis [12], which analysed the same topic on a more basic level.

1.2. Objectives

The main aim of this work is to identify and characterize the mechanisms that govern the movement of an individual bubble in presence of a close vertical wall, especially for high values of Ga and Bo, which characterize mainly non-linear trajectories. The spiralling path will be of great interest, as no evidence has been found in the literature for experimental observations of this phenomenon, most likely due to the difficulty found in the performance of this type of experiments, as empirical methods are usually intrusive and introduce impurities that may affect strongly the instability development [13].

For this reason, the study also intends to determine the influence of the vertical surface in the transitions between different regimes, considering Ga and Bo and the additional distance parameter L^*. By observing the bubbles trajectories, we expect to describe the forces induced by the flow too, which may lead to the determination of wakes and vorticity structures produced downstream of the bubble and how they influence its movement.

1.3. Previous research

1.3.1. Bubbling process

The bubble formation, or bubbling process can be described by a two-stage phenomenon: an expansion is followed by a collapse stage [2]. After expansion, the upwards buoyancy force overtakes the downwards surface tension force. At this moment, a neck appears in the vicinity of the nozzle on the bubble surface, the bubble equilibrium shape becomes unstable, and the dynamic collapse stage starts. In this phase, the neck accelerates radially inwards while it propagates downwards until it collapses, producing the release of the main bubble. This break-up phenomenon is commonly known as pinch-off [2].

Although this work will not focus on bubble formation, but on their behaviour after they have fully developed their paths, an important parameter concerning bubbling which will affect our experiments is critical air flow rate (Q_c). For bubbles formed at a flow rate under this value, their volumes at detachment can be considered independent of the air flow rate or, in other words, bubbles are formed under quasi – static conditions [2]. This value was found by Oğuz and Prosperetti [14], who stated that, under purely hydrostatic conditions ($Q < Q_c$) the volume of the released bubble is determined, in a first approximation, by equating the buoyancy and the surface tension forces, and can be usually approximated by the Fritz volume (V_F) [15] and also by the volume of an equivalent sphere. Under constant flow rate injection conditions, the instantaneous bubble volume is proportional to time and air flow rate, and the instantaneous vertical position of the bubble centroid measured from the injector exit is $z(t) = gt^2/2$ (for a detailed derivation, see Oğuz & Prosperetti [14]). It is further assumed that, at the instant of bubble detachment (t_f), the vertical position of the bubble centroid equals the final bubble radius (R_f), whence the desired equation for Q_c can be finally deduced, where Q_c stands for the critical flow rate, g for gravity acceleration, R_i is the injector radius, σ is the surface tension of the fluid and ρ is its density [14] – [16].

$$\left.\begin{array}{c}\rho g V_F = 2\pi\sigma R \\ V(t) = Qt = \dfrac{4}{3}\pi R(t)^3 \\ z(t) = gt^2/2 \\ z(t_f) = R_f, V(t_f) = V_F\end{array}\right\} \rightarrow Q = \sqrt[6]{\frac{\pi}{6} V_f^5 g^3} \rightarrow Q_c = \pi\left(\frac{16}{3g^2}\right)^{\frac{1}{6}}\left(\frac{\sigma R_i}{\rho}\right)^{\frac{5}{6}}$$

Equation 1.1: Critical air flow rate for bubble formation under quasi-static conditions [14] – [16].

The volume of bubbles formed under quasi-static is constant and can be approximated by the aforementioned Fritz volume hypothesis. For this reason, we will use it for nozzle calculation, hence for bubbles' volume assurance. This hypothesis, formulated by W. Fritz in 1935 [15], consists on evaluating an equilibrium between surface tension and gravitational forces and considering the bubble is a perfect sphere, what stands as a reasonable approximation in the first instants after detachment:

$$\pi\ d\ \sigma = \frac{\pi}{6}\ \rho\ g\ D^3\ \ ;\ \ d = \sqrt[3]{\frac{\rho\ g\ D^3}{6\ \sigma}}$$

Equation 1.2: Fritz volume hypothesis for injector diameter calculation [15].

Where d is the diameter of the injector, D is the diameter of the bubble, g is gravity acceleration and ρ and σ are fluid density and surface tension respectively.

Another aspect regarding bubble formation when using a common injector or nozzle is the surface tension limit of the fluid. This limit is expressed by Laplace equation and indicates the maximum bubble that can be formed inside a certain liquid, which mainly depends on the surface tension of this fluid:

$$\tau_{nt} - (\tau_{nt})_p = \nabla_s \sigma \xrightarrow{for\ a\ sphere} \Delta p = \frac{4\sigma}{D}$$

Equation 1.3: Laplace equation for surface tension limit of a bubble due to capillarity [17].

Where τ_{nt} stands for the shearing stresses and ∇_s refers to the surface gradient, which can be reduced as an expression involving the sphere radius when bubbles are almost spherical. When the bubble is larger than this limit, the liquid will enter into the

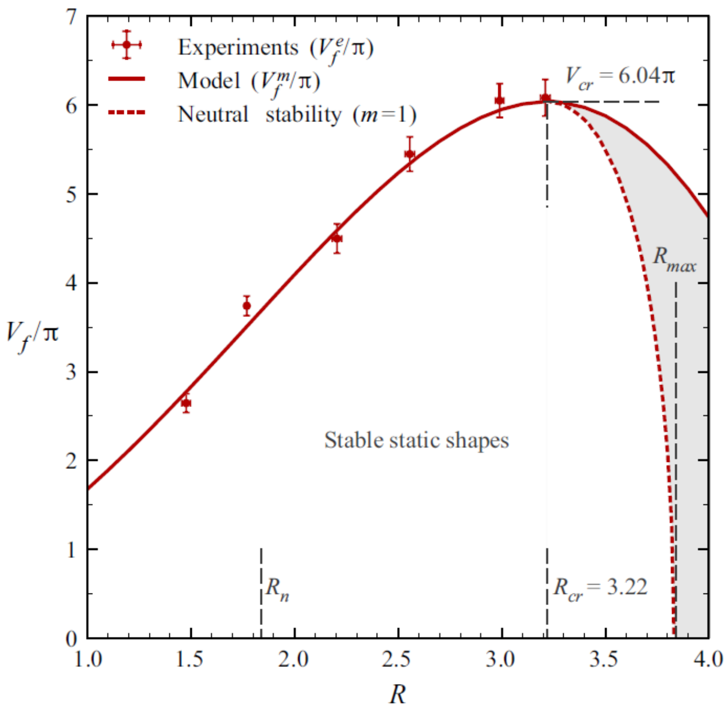

Figure 1.1: Correlation between dimensionless bubbles' volumes and dimensionless hydrophobic radii [16].

air nozzle due to capillarity and the formed bubble will not have the expected size, but will be smaller. We encountered this situation along this work and resolved it by the usage of superhydrophobic substrates. In particular, instead of a nozzle, the bubbles were injected through an orifice made on a superhydrophobic surface. Under these conditions, although Fritz volume hypothesis is a fair approximation for treated area determination also in this scene, Rubio-Rubio et al. propose a detailed analysis on the formation of giant quasi-static bubbles on superhydrophobic substrates in [16]. Figure 1.1shows the correlation between the bubble target volume and the radius of the hydrophobic surface.

1.3.2. Freely rising bubbles

After the bubble detaches from the injector and its rising stage starts, it will tend to follow a certain path. Literature points that three main types of paths can be found, namely rectilinear, planar zigzag and spiral, although a flattened spiralling regime that eventually turns into either a planar zigzagging or a helical regime is also frequently observed as well as a chaotic regime in which the bubble experiences small horizontal displacements when no standing eddy exists at the back of the bubble [18]. The path followed by the bubble depends mainly on the gravitational acceleration, the pair of fluids involved and the interfacial properties, as well as on the bubble size [13].

Hence, the problem of a bubble freely rising inside a still liquid can be described using three dimensionless parameters, (see section 2 for further details), and only two of them, namely Galileo and Bond numbers (Ga and Bo respectively), are enough to characterize the path that the bubble will follow in its rise, as shown in the following figure [18].

Consequently, different behaviours of the bubbles can be observed depending on the values of Bo and Ga, defining different regimes in the Ga – Bo plane.

Figure 1.2 (b) shows the areas where the predicted paths are stable or unstable and a transition area where an incipient path instability exists. In the work by Cano-Lozano et al. [18] 26 numerical simulations where performed within these regimes, some of which will be held as a reference and will be replicated experimentally in this work. This procedure will allow us to contrast the differences and similarities between the numerical and experimental work as well as between the cases with or without the influence of the vertical wall.

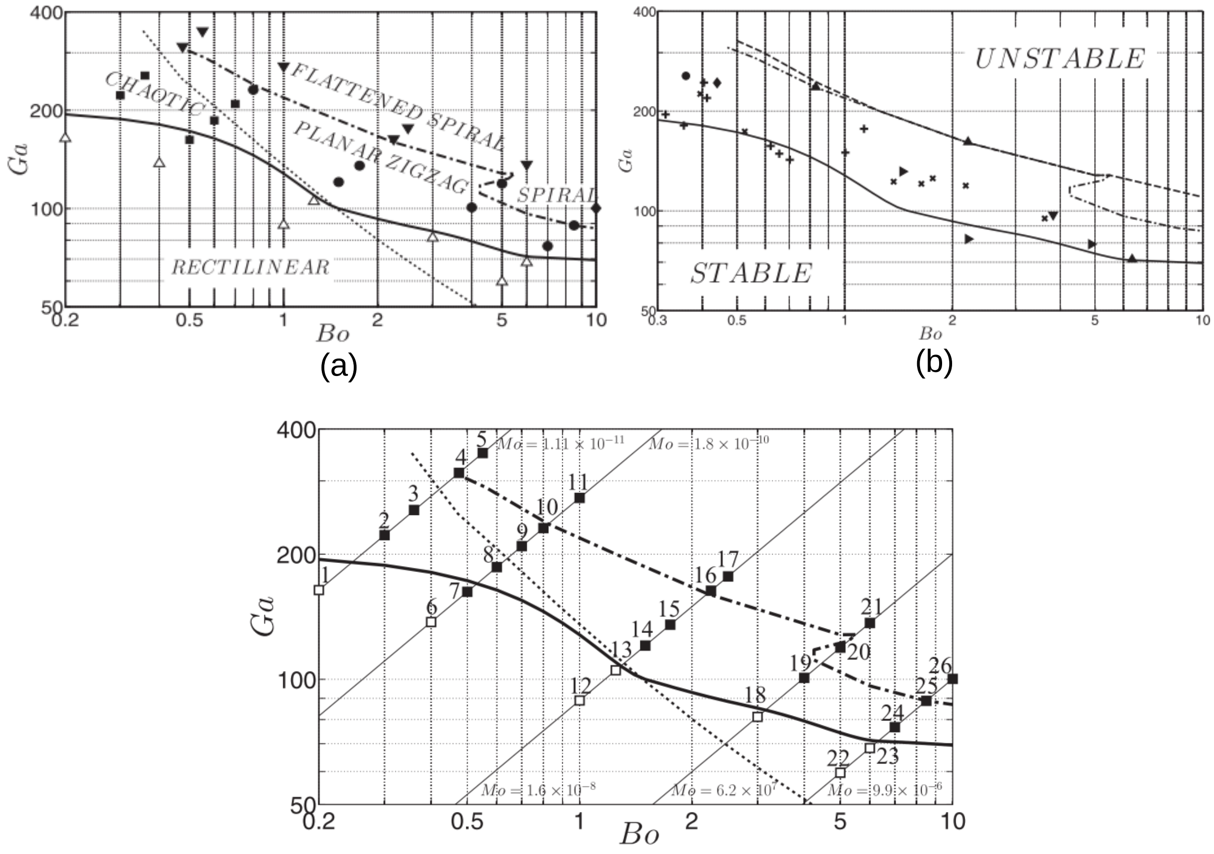

(c)

Figure 1.2: (a) Phase diagram summarizing the different styles of path observed in simulations in Cano-Lozano et al. [18] (rectilinear, ∆; planar zigzag, ●; flattened spiral, ▼; spiral (helical), ♦; and chaotic, ■). (b) Phase diagram in the (Bo-Ga) plane: solid line, approximate critical curve determined from three-dimensional simulations performed using frozen realistic bubble shapes in Cano-Lozano et al. [13], taken from [18]. (c) Phase diagram showing the entire set of simulations by Cano-Lozano et al. and positioning them in the (Bo, Ga) plane. Open (closed) symbols refer to runs in which the rectilinear bubble path was found to be stable (unstable). The thin solid lines correspond to iso-Mo lines [18].

Although all bubbles appear to follow a rectilinear path right after detachment, the onset of zigzag motion occurs when the flow loses the axisymmetry as a consequence of the development of a pair of counter-rotating streamwise vortices, as reported by Cano-Lozano et al. [13]. Similar findings regarding bubble paths were achieved by Saffman [19], who reported the shape, path and stability of small bubbles in water both theoretically and empirically. In his work, only rectilinear and zigzagging trajectories could be observed experimentally, raising doubt concerning the causes of the spiralling motion and whether they have anything to do with the onset of turbulence in the wake.

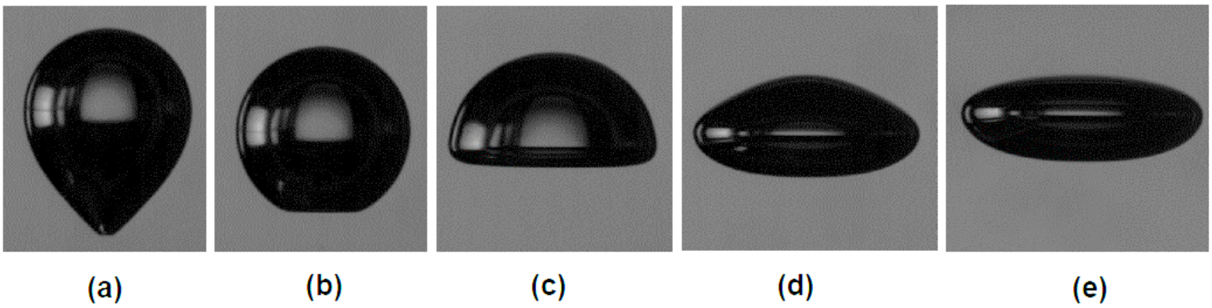

Figure 1.3: Time evolution of the shape of a bubble in the rectilinear regime after detachment. Pictures (a) and (b) show a nearly spherical shape while in (c) to (e) the bubble tends to become oblate. Taken from [12].

Another aspect worth mentioning for isolated rising bubbles is their velocity, as it has been found that the bubble experiences different phases while it rises. First, when the bubble detaches from the injector, its shape is essentially spherical and it rapidly accelerates in the vertical direction (see Figure 1.3 a, b). After some time, it becomes oblate (see Figure 1.3 c, d, e), displacing more fluid and increasing the drag force. Note that the terminal velocity and final shape of the bubbles are independent of the initial shape [20]. However, the aspect ratio (relation between minor and major axis length of the bubble) does increase monotonically with Ga and Bo [13], and thus for some of the bubbles studied in this work the shape indeed deviates noticeably from spheroidal (see Figure 1.4).

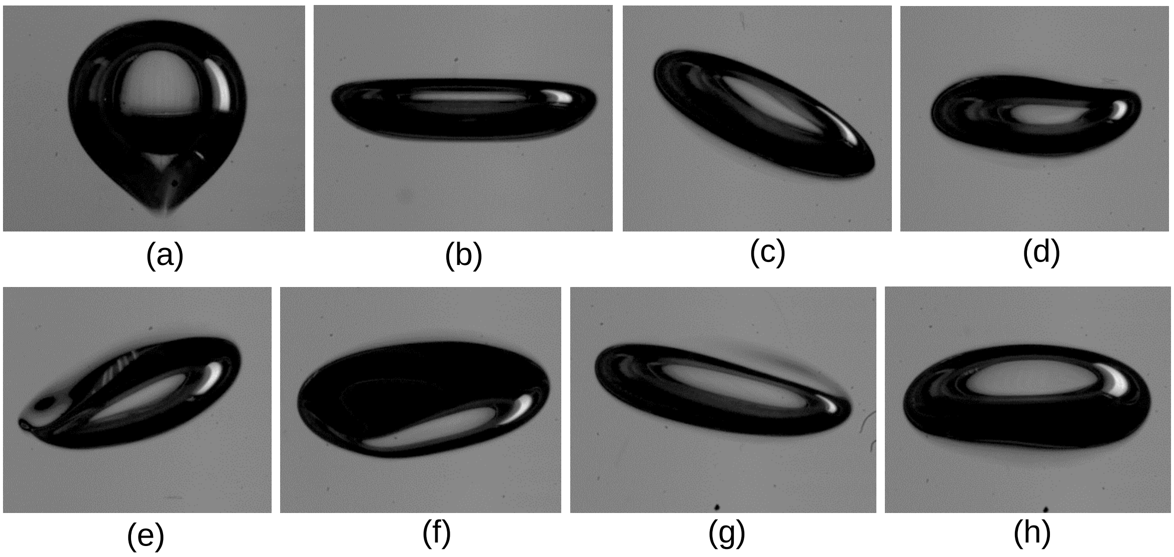

Figure 1.4: Frontal view of the shape evolution of a spiralling rising bubble (left to right, top to bottom). Images belonging to the present experimental work.

Finally, a balance between buoyancy and drag forces results in a quasi-terminal rise velocity that remains constant indefinitely [18], as explains Figure 1.5, in which cases depicted by pictures a, c and f are the reproduced experiments in this work (bubbles 22, 19 and 26). Although zigzagging and spiralling regimes show slight peaks due to the deformation caused on the bubble when it oscillates horizontally, we can still find a constant average vertical velocity, what aligns with the common wisdom in the literature assuring a unique rise velocity to a bubble of a given volume in a given liquid or, more generally, a unique value of the drag coefficient for given Weber and Morton numbers once the flow has become steady [17] – [20] – [21].

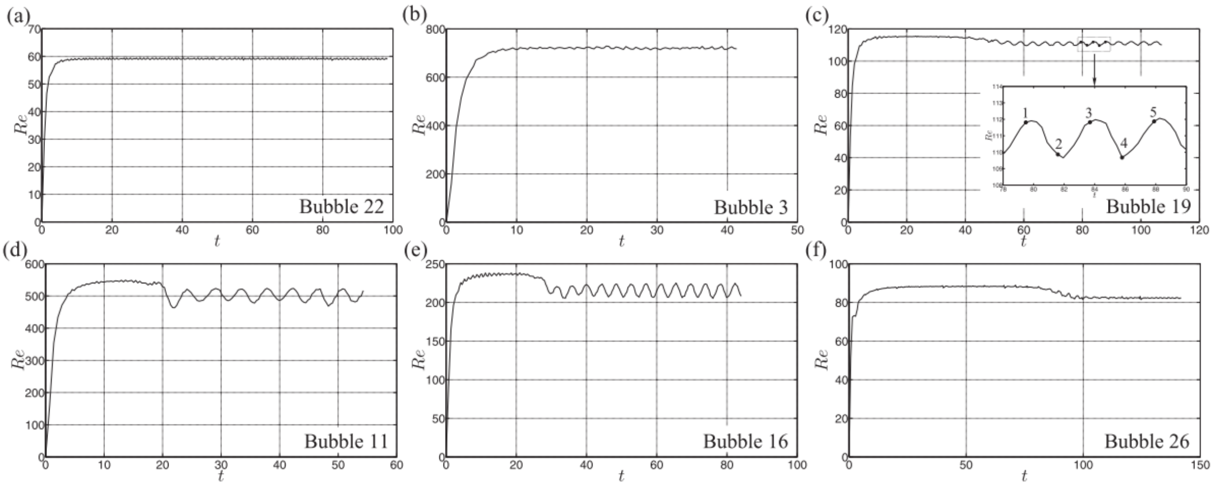

Figure 1.5: Evolution of Reynolds number (equivalent to velocity evolution) for different bubbles in Cano-Lozano et al.: (a) rectilinear regime, (b) chaotic regime, (c) planar zigzagging regime, (d) and (e) flattened spiralling and then planar zigzagging regime, and (f) spiralling (helical) regime [18].

1.3.3. Wall – bubble interaction

The problem involving the effect that a vertical wall causes in the path of an isolated bubble has been also studied both numerically and experimentally. The case of a rising oscillating zigzagging bubble close to a vertical wall was studied by Lee and Park [22]. Their findings concluded that if the bubble collides with the wall, the bubble migrates away from the wall very fast to later quickly slow down moving back towards the wall. This change of direction occurs because as the bubble moves away from the wall, the vortex-induced force becomes more influential than the inertial force (the latter becomes smaller due to viscous dissipation through the wake-wall interaction); thus, the bubble decelerates and changes its direction [23]. Figure 1.6 shows that de Vries et al. [24] reached similar findings.

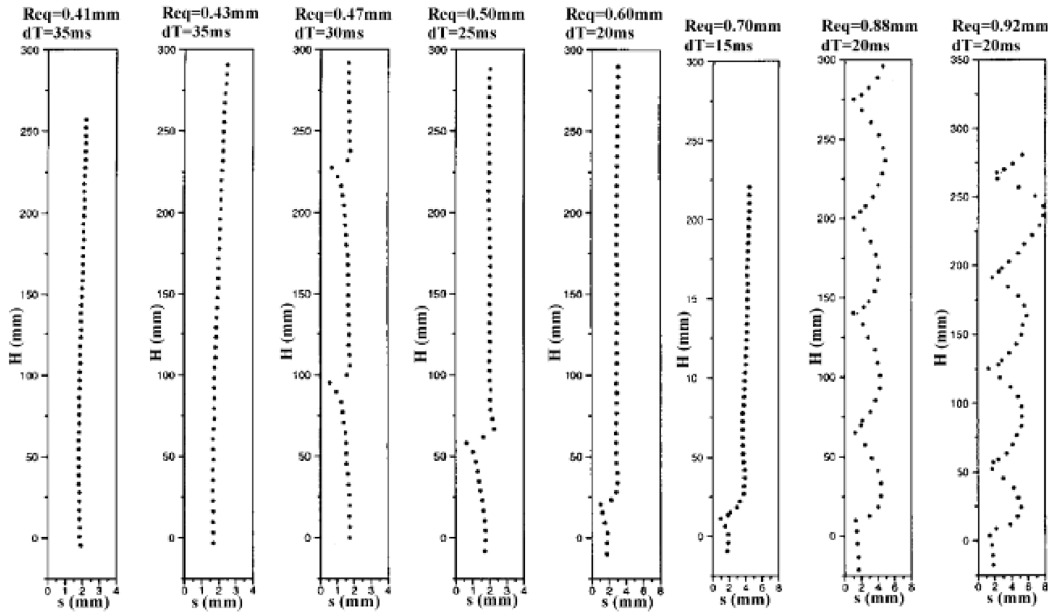

Figure 1.6: Trajectories of bubbles of different sizes as they interact with a vertical wall, determined experimentally by de Vries et al. in [24]. In all cases the initial separation L = 1.57 mm.

However, much smaller wall effects were found for the case without collision (bubble-wall distance of 1.9 times the bubble diameter, $L^*=1.9$). Literature points that the presence of the wall imposes a repulsion on the bubble and that the bubble migrates away from the wall upon release even if no collision exists, as described by Zhang et al. [25] (see section 4.2 for further details on this work).

In this work we will focus mainly in cases without wall collision, as the minimum distance set between the wall and the initial centroid position will be of one bubble diameter ($L^*=1$). Nevertheless, effects of collisions will not be irrelevant. For the tested regimes where horizontal oscillations occur (mainly zigzagging and spiralling paths), we encounter that bubbles suffer a remarkably robust deformation, becoming strongly oblate. This shape modification along with the horizontal displacement that the bubble experiences may provoke a collision with the wall.

Furthermore, Lee and Park [22] found that the wall induces more complex behaviour by cause of increased vorticity or boundary-layer like secondary flow structures. The horizontal movement of the bubble, which is caused due to surface energy is reduced in amplitude (damping effect) because of the wall interference causing energy waste. Interestingly, the vertical wall seems to serve as a destabilizing factor in the wall-normal direction but a stabilizing factor in the spanwise direction [25].

Concerning the changes in the bubble’s wake, the main differences induced by the wall regard to a faster transition to the detached vortex ring structures and an interference in the growth of the streamwise vortex. All these conditions may lead to more complex shape and path instabilities for the rising bubble, for instance, bounce or sliding motions may happen depending on the bubble size and the initial distance between the wall and the bubble [25] (see the results of these simulations in Figure 4.12).

All these conditions may find their reasoning in the hydrodynamic forces behind the problem. Shi et al. [26] studied numerically how Reynolds number, wall distance and shear rate influence the drag and lift forces experienced by the bubble. Different combinations of the aforementioned parameters may lead the bubble to be repelled or attracted by the wall. For the bubbles present in this work (either $Re \approx 50$ or $Re \approx 110$) the wall-shear interaction is significant only when the bubble moves very close to the wall and, as Re decreases, wall boundary layer effect becomes negligibly small and viscous effects gradually inhibit the bending of the wake, reducing the overall repulsive force.

As for the literature mentioned hitherto, many numerical results have explained the problem of a bubble rising in the proximity of a wall. However, only few experimental works have been developed and they are limited to really modest Bo-Ga ranges. For this reason, this work has the aim to analyse unexplored regimes and the transitions between them. For instance, a spiralling bubble has never been reproduced experimentally to the best of the author knowledge except for one work by Shew et al. [27], but this spiral was not in the “spiralling regime”, but in the regime of low Bond number (“flattened spirals”), what connotes the innovation and novelty entailed in this work, which will explore spirals formed by large bubbles in the high Ga – Bo region.

1.3.4. High-speed imaging and digital postprocessing

Digital imaging is a non-intrusive method and does not require direct contact with the flow field, thus can achieve a high spatial and temporal resolution. With the major development of digital imaging technique in recent years, image processing combined with high speed cameras has become an attractive technique for its capability in obtaining high spatial and temporal resolution bubbly flow data [28].

Concerning bubble recording, the most typical imaging system implies large bubbles being back-lit by a diffuse source. According to Bongiovanni et al. [29], this set – up is genuinely useful because some of the rays reach the lens of the camera directly without touching the bubble, forming the background illumination and thus capturing the bubble shadow as a dark disk. On the other side, doubly refracted rays produce a clear spot in the centre of the bubble which may lead to a wrong shape detection. The clear spot radius depends on the size and distance of the source, and will be maximum for an infinite source. In this work we solve this problem digitally during images postprocessing by filling all pixels inside the external bubble contour with dark values, so that the image of a spherical bubble is detected as a dark ring on a clear background.

The reflected rays also form a bright ring inside the bubble shadow, very close to the bubble edge. The brightness of this external ring is very close to the background brightness and so cannot be distinguished from it. Due to this, the volume of gas may be underestimated, typically, the error made on the volume measurement will exceed 5% when a very large light source is utilized or when the bubble is very close to the source [29]. Both conditions occur in our experimental set-up, as shown in section 3.2, so the mask applied during bubble edge detection is slightly dilated to mend this volume underestimation.

After capturing these bubble images, postprocessing will consist on extracting the bubble contour from its background. Fu and Liu [28] assure brightness correction and noise reduction are critical to provide a correct edge detection. Subtracting the background and the average image intensities, part of the noise can be removed. A global threshold can then be used to convert the grey scale image to binary image. The Canny edge detector is used to acquire the outer and inner boundaries of bubbles for further processing [28]. In this work, these techniques were not enough to eliminate all noise, so different filters were applied to the images, including a Gaussian filter and a median filter among others. Only small effect could be appreciated though, so this technique of noise elimination was discarded and different filters were applied to the postprocessed raw data instead.

The mentioned threshold should be carefully selected. N. Otsu [30] derived a method based on integration of the grey-level histogram of an image. This is a global property of the image, unlike differentiation, which is used in other methods such as valley detection and is a local property. This method consists on defining the probability of a pixel with a certain grey level being part of the "class" background or the "class" object by a certain threshold. Then, in order to evaluate the "goodness" of the threshold discriminant criterion measures are introduced. Thus, the problem is reduced to an optimization problem to search for a threshold that maximizes one of the criterion measures. This standpoint is motivated by a conjecture that well thresholded classes would be separated in grey levels, and conversely, a threshold giving the best separation of classes in grey levels would be the best threshold. These characteristics and the utilization of integration make Otsu method quite general, covering a wide scope of unsupervised decision procedure and opting for one automatic, stable, optimal threshold for each image.

In previous works, Otsu method was applied to this kind of images, obtaining reasonably accurate results. However, for this work we tried to apply an adaptive threshold based on integration, as proposed by Bradley and Roth [31], who an extended a previous method by Wellner [32]; the main difference here is that a distinct threshold value is computed for each pixel in the image.

The main idea in Wellner's algorithm [32] is that each pixel is compared to an approximate moving average of the last s pixels seen while traversing the image. If the value of the current pixel is t percent lower than the average then it is set to black, otherwise it is set to white. This method works because comparing a pixel to the average of nearby pixels will preserve hard contrast lines and ignore soft gradient changes. The advantage of this method is that only a single pass through the image is required, but a problem with it is that it is dependent on the scanning order of the pixels. In addition, the moving average is not a good representation of the surrounding pixels at each step because the neighbourhood samples are not evenly distributed in all directions.

By using the integral image [31], the same output can be obtained independently of how the image is processed. Instead of computing a running average of the last s pixels seen, the average of an s x s window of pixels centred around each pixel is computed. This is a better average for comparison since it considers neighbouring pixels on all sides. The integral image is calculated in the first pass through the input image while in a second pass the s x s average is computed using the integral image for each pixel in constant time and then the comparison is performed. If the value of the current pixel is t percent less than this average then it is set to black, otherwise it is set to white. This technique demonstrated to work accurately for all the images in this work and performed a better distinction of the bubble shape than Otsu method when the wall’s shadow interfered with the bubble.

2. DESCRIPTION OF THE PROBLEM

The problem of an isolated bubble rising in the proximity of a solid vertical wall is described as shown in Figure 2.1 (b). As reported by Cano- Lozano et al. [18], the problem of an isolated rising bubble can be described using three dimensionless parameters. Adding variable L, which stands for the distance between the bubble centroid after pinch of and the wall surface, the resulting problem variables are the ones shown in Figure 2.1 (a), namely fluid properties (density ρ, dynamic viscosity μ and surface tension σ), equivalent bubble diameter (D), gravity acceleration (g), rise velocity (v) and distance to the wall (L).

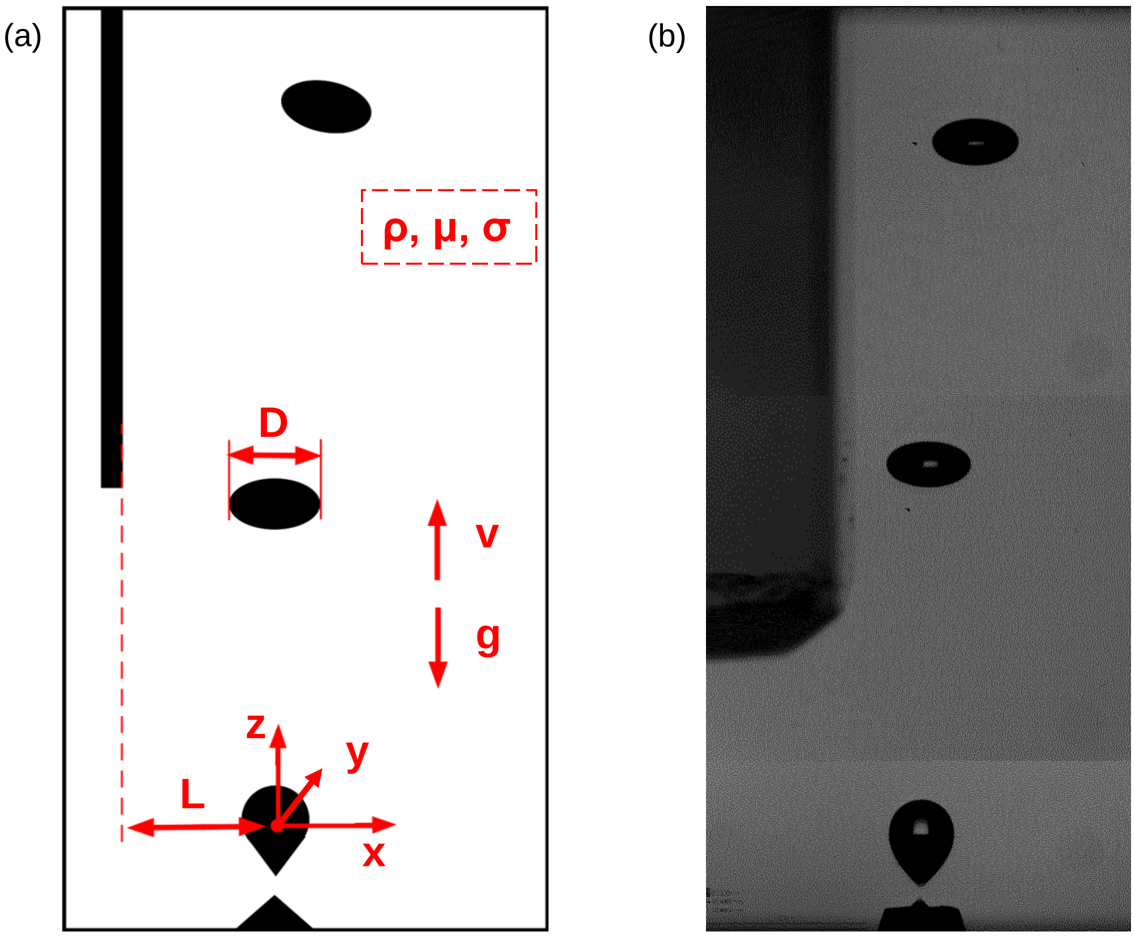

Figure 2.1: (a) Scheme of the variables of the problem, where ρ stands for fluid density; σ, for fluid surface tension; μ, for fluid viscosity; g is gravity acceleration; s is the distance between the surface of the wall and the bubble centroid; D is the equivalent diameter of the bubble and v, which is the main unknown, stands for the rising terminal velocity of the bubble. The coordinates' origin is on the centre of the injector. (b) Sequence of pictures of the experiments developed at three different levels of the tank (lowest, medium, and highest).

Note that the characteristic length that will be used to define the dimensionless parameters is the equivalent bubble diameter. Bubbles are not perfect spheres; hence, this diameter is defined as the diameter of a sphere of same volume as the bubble.

This criteria was chosen in accordance to the reference cases in Cano-Lozano et al. [18] for an easier and more direct comparison. The used reference frame is fixed in the bubble's centroid position right after detachment.

Applying Buckingham Π theorem for the variables involved in the problem and using a base compound of density (ρ), gravity acceleration (g) and equivalent diameter (D), the obtained dimensionless numbers which describe the problem are:

$$\Pi_0 = \frac{v}{\sqrt{gD}} = Fr \qquad \Pi_1 = \frac{\rho g D^2}{\sigma} = Bo \qquad \Pi_2 = \frac{\rho D\sqrt{gD}}{\mu} = Ga \qquad \Pi_3 = \frac{L}{D} = L^*$$

$$\Pi_0 = F(\Pi_1, \Pi_2, \Pi_3) \rightarrow \frac{v}{\sqrt{gD}} = F\left(\frac{\rho g D^2}{\sigma}, \frac{\rho D\sqrt{gD}}{\mu}, \frac{L}{D}\right) \rightarrow \boldsymbol{Fr = F(Bo, Ga, L^*)}$$

Equation 2.1: Dimensionless numbers resulting from Buckingham Π theorem for a bubble rising near to a vertical wall.

Hence the problem of a bubble rising close to a vertical surface can be described by Froude (Fr), Bond (Bo) and Galileo (Ga) numbers along with the aforementioned L^* parameter, which stands for the dimensionless distance to the wall. However, Froude number will not provide as clear an information for cases classification in literature as Reynolds number (Re) would, thus we operate with Froude and Galileo numbers to obtain Re = Ga Fr. Note that we will keep Froude number as Π_0 because it is a useful means of expressing dimensionless velocity.

$$Re = Ga \cdot Fr = \frac{\rho D\sqrt{gD}}{\mu} \cdot \frac{v}{\sqrt{gD}} = \frac{\rho v D}{\mu}$$

Equation 2.2: Expression for Reynolds number as the product of Galileo and Froude numbers.

Finally, we will introduce Morton number. It can de deduced from the previous theorem that no more dimensionless parameters are necessary to describe the problem. Nevertheless, Morton number (Mo), which can be expressed as a combination of Galileo and Bond numbers, will be useful for this analysis, especially when trying to set certain accurate conditions in our experiments.

$$Mo = \frac{Bo^3}{Ga^4} = \frac{g\mu^4}{\rho\sigma^3} \rightarrow \begin{cases} Fr = F'(Bo, Mo, L^*) \\ Fr = F''(Mo, Ga, L^*) \end{cases}$$

Equation 2.3: Morton number expression, Buckingham Π theorem based on Reynolds and Morton number for a bubble rising near to a vertical wall.

As shown in the equation for Morton number, this parameter only depends on the fluid properties, thus it will be certainly useful to assure the fluid conditions for each experiment. Although it may substitute either Bond or Galileo numbers in Buckingham Π theorem, we will keep both of them, as they depend on the bubble diameter, which is a critical parameter for the description of the problem; Morton number only will be used as an additional criterion for fluid conditions setting and description. Furthermore, Morton number may not be a clear indicator of the experimental conditions, as fluid properties appear raised to high exponents in its definition, thus even small instrument errors may lead to Morton numbers really far from target.

3. EXPERIMENTAL METHOD

3.1. Overview of studied bubbles and fluids

For this study, we will refer to the cases analysed by Cano-Lozano et al. [18], who performed a numerical analysis of freely rising bubbles in different conditions. We will focus on one case in each regime, namely bubbles 22 (rectilinear), 26 (spiral) and 19 (planar zigzag) as in

Figure 1.2 (c).

Assuming known fluid properties, the bubble diameter which assures the required conditions can be derived from the dimensionless numbers which describe the problem, namely Bo and Ga. They are summarized in Table 3.1.

Case	Liquid	Mo	Bo	Ga	St	Path	Wake	Regime
19	T05	6.2×10^{-7}	4.0	100.8	0.108	planar zigzag	2CRV 2R	zigzagging
22	T11	9.9×10^{-6}	5.0	59.61		rectilinear	axisymmetric	rectilinear
26	T11	9.9×10^{-6}	10.0	100.25	$0.136 \rightarrow 0.174$	planar zigzag $\rightarrow$ helix (spiral)	spiral	spiraling

Table 3.1: Characteristic properties of the flow conditions considered in Cano-Lozano et al. for the bubbles considered in this study. Here 2CRV stands for two counterrotating vortices. The term 2R refers to the number of vortex loops per period in the wake of zigzagging bubbles [18].

Achieving these specific conditions will require a precise control of the fluid properties and the bubble diameter. As a first approach, we decided to reproduce the same conditions involved in the simulations by utilizing the same fluids considered, which, for the bubbles here analysed, consisted of silicon oils of different viscosities. Their properties can be visualized in Table 3.2.

Liquid	ρ (kg/m^3)	μ (mPa s)	σ (mN/m)	Mo$=g\mu^4/(\rho\sigma^3)$
DMS-T05	918	4.59	19.7	6.2×10^{-7}
DMS-T11	935	9.35	20.1	9.9×10^{-6}

Table 3.2: Fluid properties for silicon oils used in the reference case, T05 for bubble 19 (planar zigzag, Mo $6.2 \cdot 10^{-7}$) and T11 for bubbles 22 and 26 (rectilinear and spiralling regimes respectively, Mo $9.9 \cdot 10^{-6}$) [18] – [33].

3.2. Set-up and measurement procedure

3.2.1. Description of experimental facility

The experiments were performed in the facility depicted in the descriptive picture in Figure 3.1 and the scheme in Figure 3.2. In the following, the different parts of which it is compound will be described and justified.

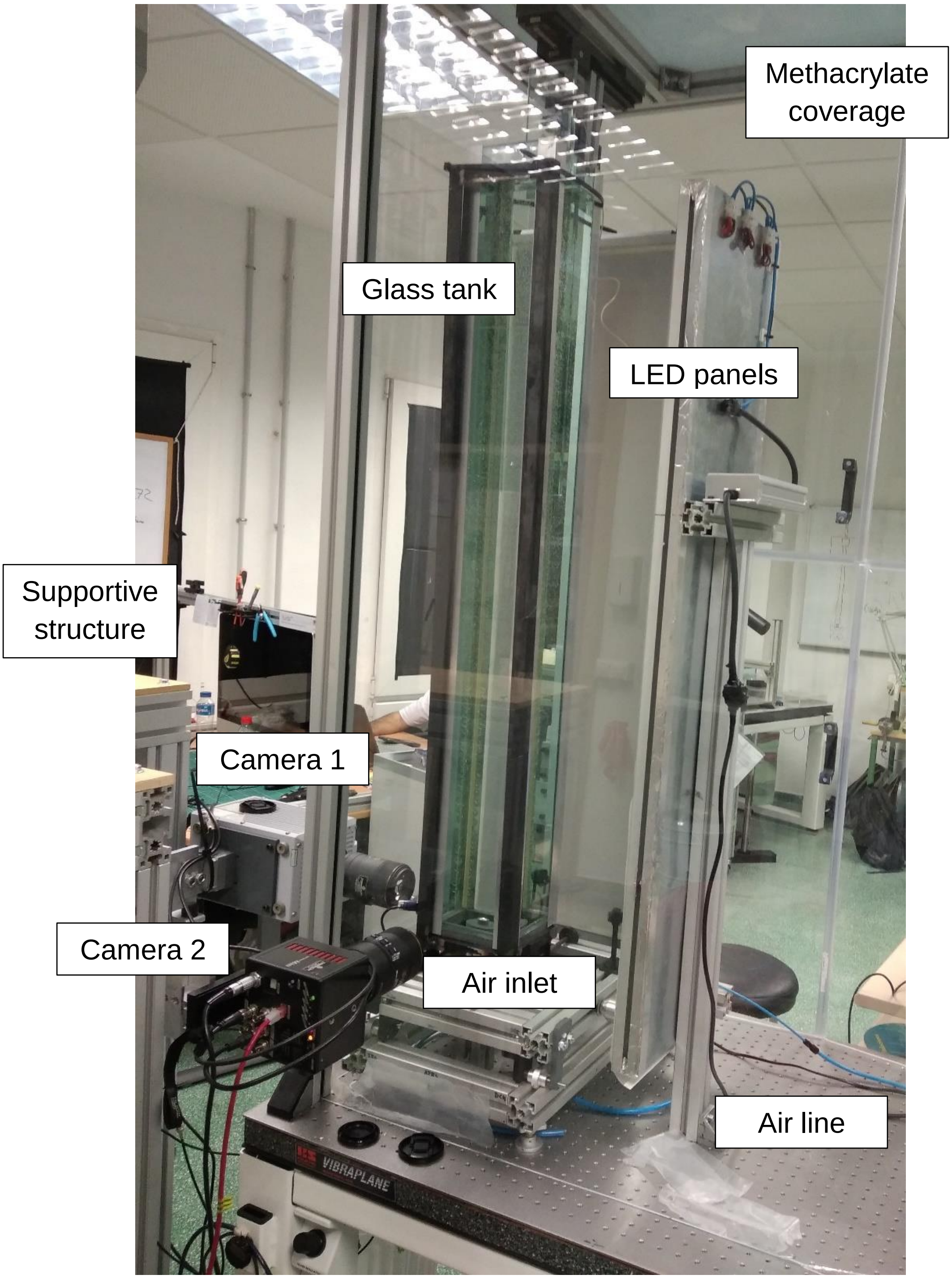

Figure 3.1: Experimental facility

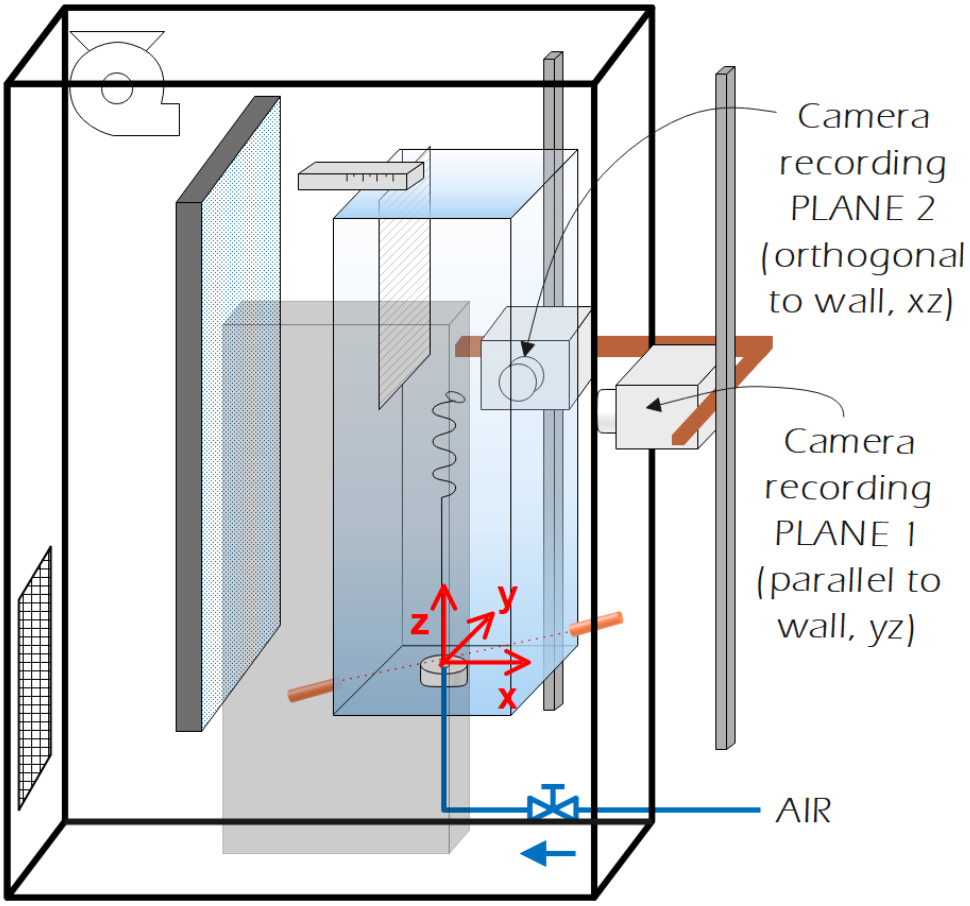

Figure 3.2: Scheme of experimental facility.

The main part of the facility is the hexahedral glass tank depicted in Figure 3.3. The dimensions of this tank (120x15x15 mm^3) were enlarged in comparison with the one used in previous experiments in order to allow the largest bubbles to develop their paths and terminal velocities before encountering the vertical surface. Due to this, solid walls of different lengths had to be utilized.

The tank was laid on a platform which allowed for movement in two directions so that the window captured by the cameras could be easily moved and spatial resolution could be maximized without changing the position of the cameras. Note also that metal guides were placed around the tank in order to keep it as vertical as possible and to avoid tumbling (see Figure 3.3). Glass was selected as the tank material because of its resistance to ethanol as a means of cleaning. This was mandatory because elimination of surfactants was vital for the experiments, as their presence may affect the gas-liquid interface, changing the shear-free boundary condition satisfied by the liquid into a no-slip one at least on a part of the interface, therefore modifying the flow structure past the bubble, hence the threshold of the instability [11] – [34]. Surfactants

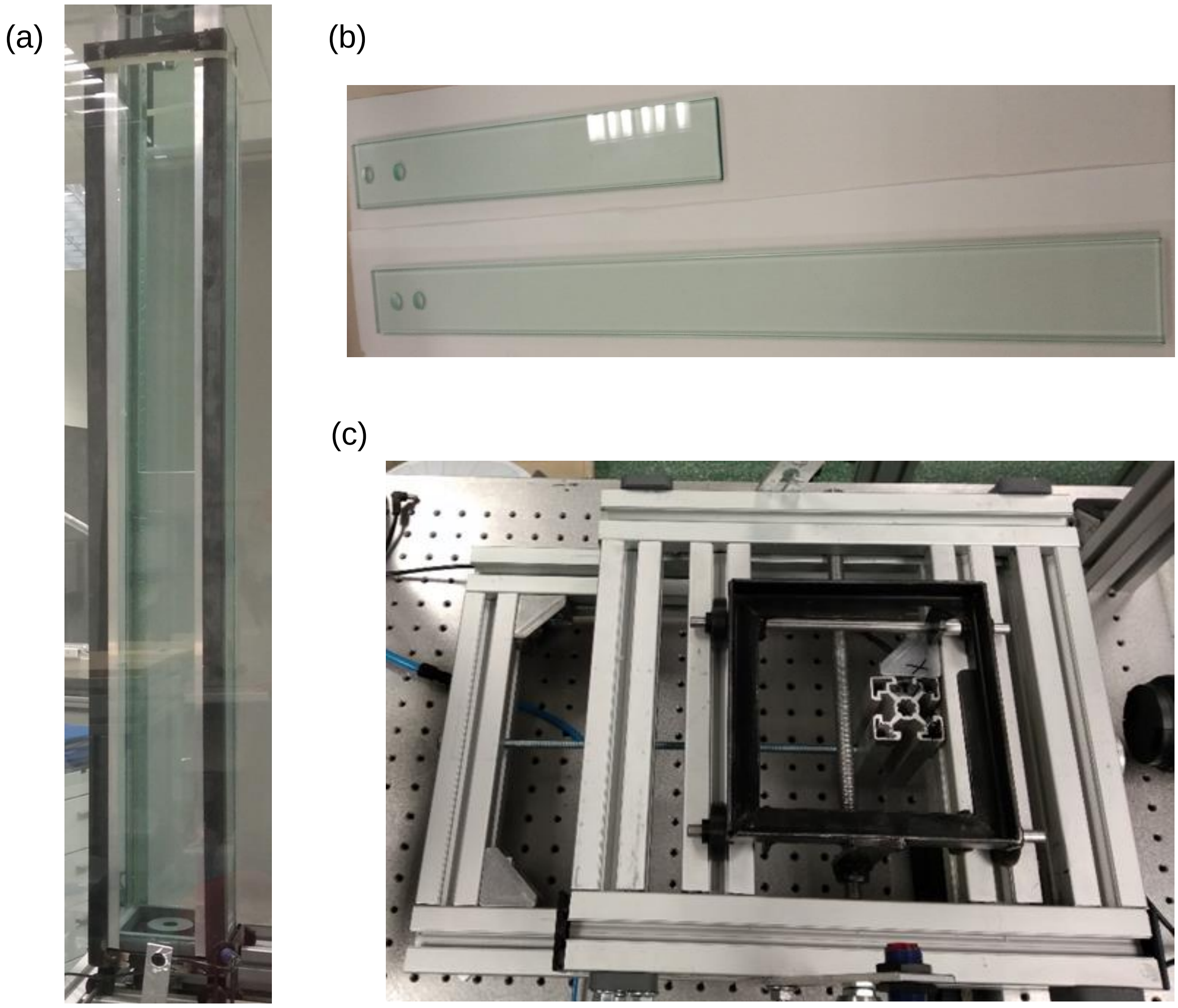

Figure 3.3: (a) Glass tank with metal guides, (b) Different glass walls used as vertical surface, (c) Base platform for tank movement.

are not that determining when using nonpolar fluids, but they are for water-based mixtures. To avoid soiling, the facility was completely confined inside a methacrylate coverage.

The tank has an open end both at the top and the bottom for improving and aiding cleaning tasks. At the bottom, a removable lid with a cylindric hole is incorporated. This hollow section provides for easy installation and removal of different nozzles where the air inlet can be placed, even if the tank is full, avoiding cyclic fluid movements which may cause its soiling, degradation or aeration. This was accomplished thanks to a screwed mechanism which pressed the injector into the tank with the help of a packing ring, providing secure adherence and preventing leakage (Figure 3.4 c). With the same purpose, a pump for introducing the fluid into the tank was incorporated, avoiding the formation of multiple bubbles inside the fluid which could have distorted the wanted trajectories (Figure 3.5 b).

(a) (b) (c)

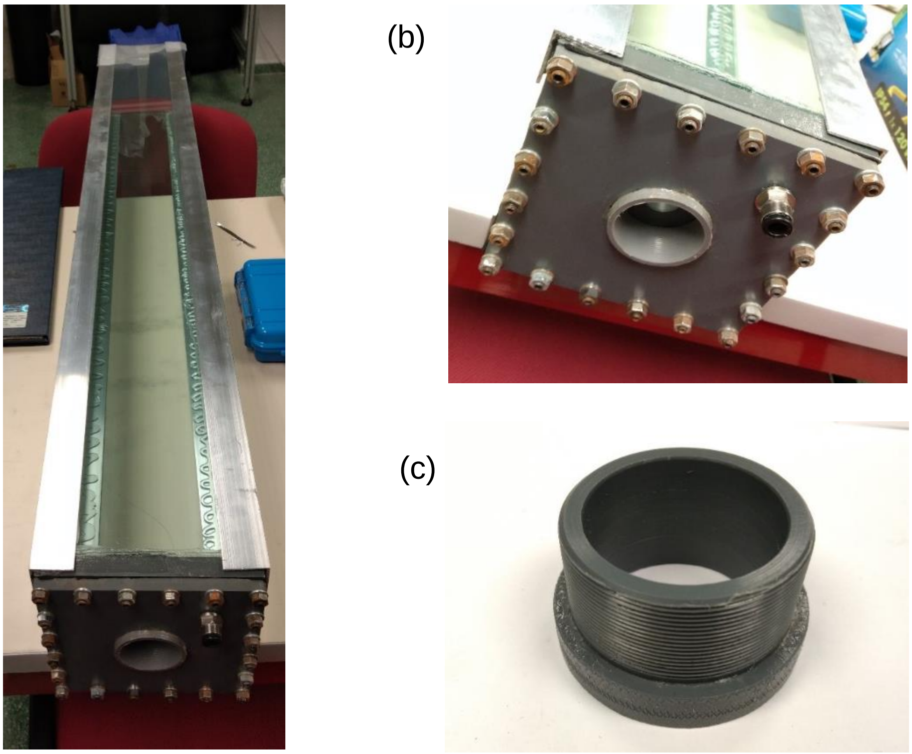

Figure 3.4: (a), (b) Open tank and removable lid with central overture for air inlet positioning, (c) Threaded pressure mechanism for nozzle installation.

The installation for bubbles formation and rise can be completed by adding an air line, which includes a precise manual valve (Figure 3.5 a), allowing for flow rate control. Although air flow rate is not a critical parameter in this problem, it is essential that it is kept low enough for quasi-static conditions to be satisfied. In this way, a moderate flow rate will avoid previous or subsequent bubbles affecting each other's movement or the fluid's.

A crucial concern in our experiments is the manipulation of the distance between the wall and the bubble, hence L^* control. A flat glass plate was introduced and hanged over the tank. The hanging device consisted on a rack and pinion mechanism (Figure 3.6 a) which allowed for wall displacement towards and away from the nozzle, hence

(a) (b)

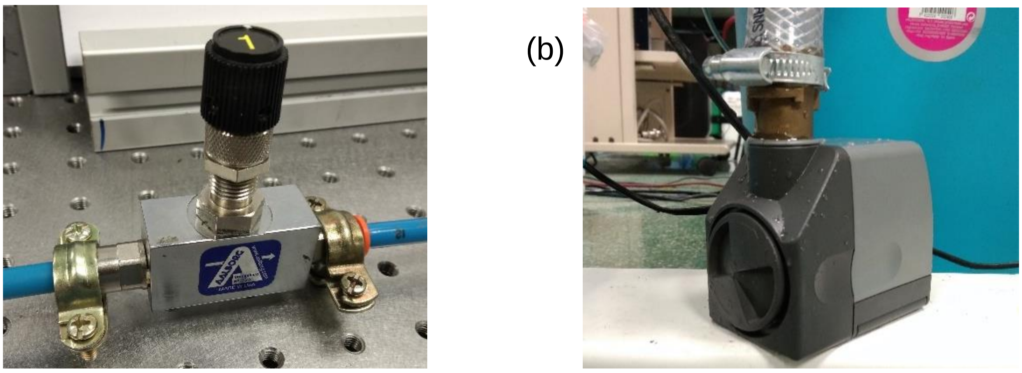

Figure 3.5: (a) Valve for air flow rate control, (b) Pump for tank filling.

from the bubble, what allowed us to perform experiments for three values of L^* (namely 1, 2 and 4 for every bubble). Before hanging the wall, a precision goniometer was installed after this system so that verticality could be assured (Figure 3.6 b).

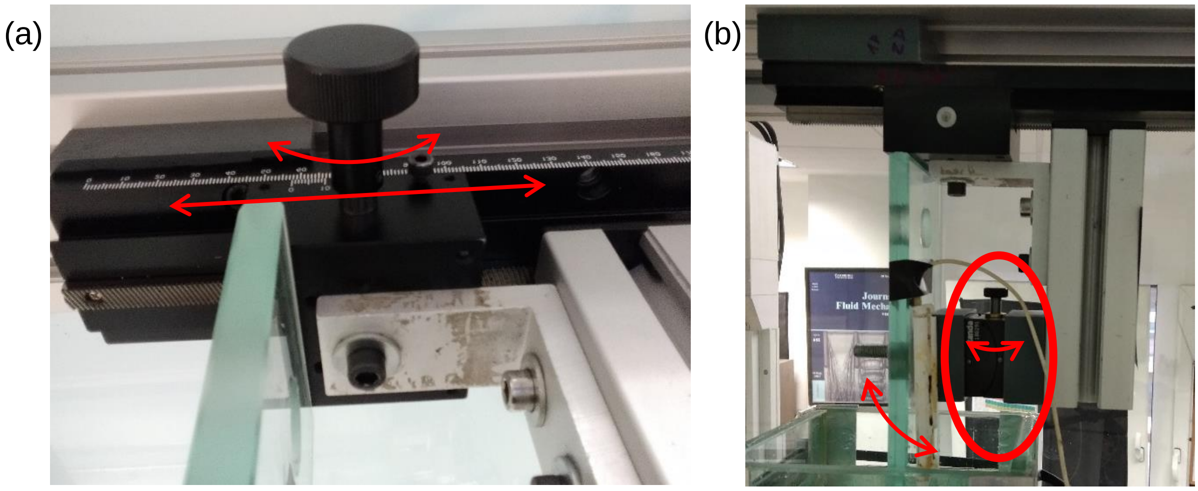

Figure 3.6: (a) Rack and pinion mechanism for wall horizontal displacement, (b) Angle control system for verticality assurance.

3.2.2. Liquids and injectors selection

Concerning fluid properties, our aim was to replicate the reference cases from Cano-Lozano et al. [18], thus the selected fluids were the ones described in Table 3.2. From the expressions of Bond and Galileo numbers and the aforementioned liquid properties (see Table 3.2) and assuming several hypotheses that will be described in the following, the bubble and nozzle diameters are calculated and shown in Table 3.3.

Case	Liquid	Mo	Bo	Ga	D (mm)	d (mm)
19	T05	$6.2 \cdot 10^{-6}$	4.0	100.8	2.97	1.98
22	T11	$9.9 \cdot 10^{-6}$	5.0	59.61	3.30	2.76
26	T11	$9.9 \cdot 10^{-6}$	10.0	100.25	4.67	7.78

Table 3.3: Bubble and injector diameters based on characteristic properties of the flow conditions of the reference cases by Cano-Lozano et al. [18].

Bubbles were detached from an injector at the centre of the tank bottom. As described in the previous table, different bubble volumes were to be analysed, what provided the need for multiple air injection devices. The default solution for this was a simple brass nozzle, as shown in Figure 3.7 (left). These nozzles offered valid results for the smaller bubbles tested (rectilinear and zigzagging regimes) although this was not the case for the largest ones (spiralling regime); the reasoning for this fact is explained in the following.

Assuming quasi-static conditions, the diameters of the nozzles could be calculated using Fritz volume hypothesis [15] (see Equation 1.2, where the injector diameter is calculated as $d = \sqrt[3]{\rho g D^3/6\sigma}$). For the bubbles in the spiral regime the calculated nozzle diameter as for Fritz volume hypothesis was too large, surpassing the surface tension limit of the fluid used in the reference case. This would have meant that air would not have come out of the nozzle, but the fluid would have come into the air line, as described by Clift et al. [17] by Laplace equation under static conditions (see Equation 1.3).

In these situations, simple nozzles were replaced by superhydrophobic substrates. For this purpose, a superhydrophobic coat of Rustoleum® NeverWet™ was applied to a flat injector with a narrow orifice. This substance prevents water from covering the orifice so that air can fill all the treated area, creating large quasi-static bubbles. Although this solution offers the possibility to produce several different bubble sizes without the need for multiple different injectors, the appearance of many counterpoints relegated the hydrophobic method only for the largest bubbles, when there was no other possibility. The long drying time, the fast attrition rate (especially quick when using poorly watered mixtures) and the difficulties found in performing the requested hydrophobic area with enough precision were the main drawbacks that motivated our preference for the nozzle method.

Hence, the control parameter for these larger bubbles was the treated area diameter (d, equivalent to the nozzle diameter in the rest of cases). As explained previously, instead of using Fritz volume hypothesis, we applied the correlation by Rubio-Rubio et al. depicted in Figure 1.1 [16] along with the fluid properties to achieve the necessary treated area (see Table 3.3).

Figure 3.7: Different nozzles used in different experiments, from left to right: 2.35 mm diameter nozzle, 2 mm diameter nozzle, 1 mm orifices for hydrophobic treatment (x 2).

Another parameter that had to be modified due to the use of hydrophobic substrates was the studied fluid, as silicon oils are not repelled by these substances, but water-based mixtures are. As a solution, a glycerol-water mixture was prepared in a similar manner to previous experiments in order to obtain an identical Morton number to the one of the target silicon oil. Three-dimensional fits for density, viscosity and surface tension of glycerol-water mixtures were accomplished for changing temperature and composition as for the data in the tables provided by [35] – [36] – [37] (see Figure 3.8). In order to validate these results, tests of different compositions were performed under controlled temperature and the critical fluid properties (surface tension and kinematic viscosity) were empirically measured. The results showed remarkable differences compared to the data extracted from the literature and the executed fits, especially regarding surface tension, hence the definite mixture was based on the measured properties of the tests and then checked for the target Morton number. These contradictions motivated even more our preference for the nozzle method in those cases where it was possible, as silicon oils' properties can be much more easily controlled.

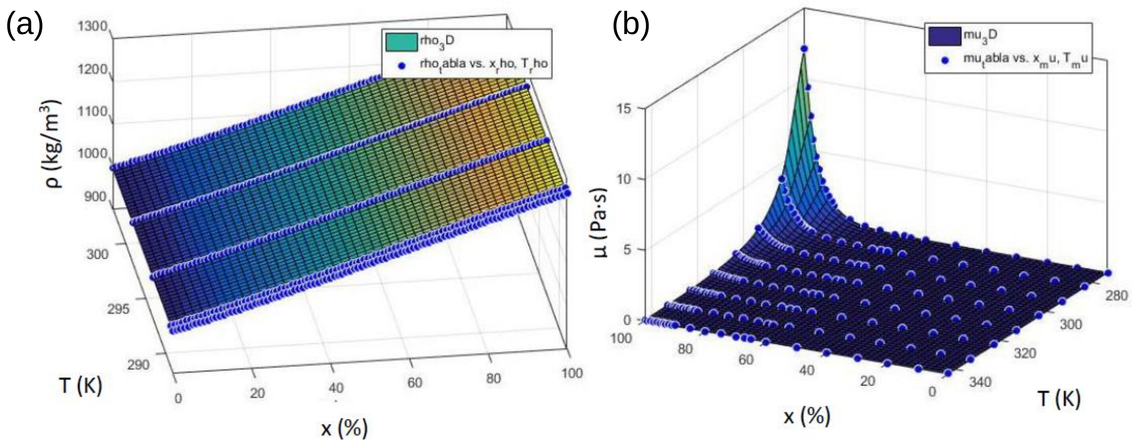

Figure 3.8: Interpolation of data from used to calculate (a) density, ρ and (b) dynamic viscosity, μ for variable concentration (x) and temperature (T).

From what has been exposed hitherto, surface tension has been found to be a critical parameter for an accurate case reproduction, hence it was precisely checked and measured during every set of experiments.

The main problem regarding surface tension in our experiments concerned the water fraction of the mixture. This water came from a general deposit which had been cleaned with some type of surfactant substance, what decreased water surface tension

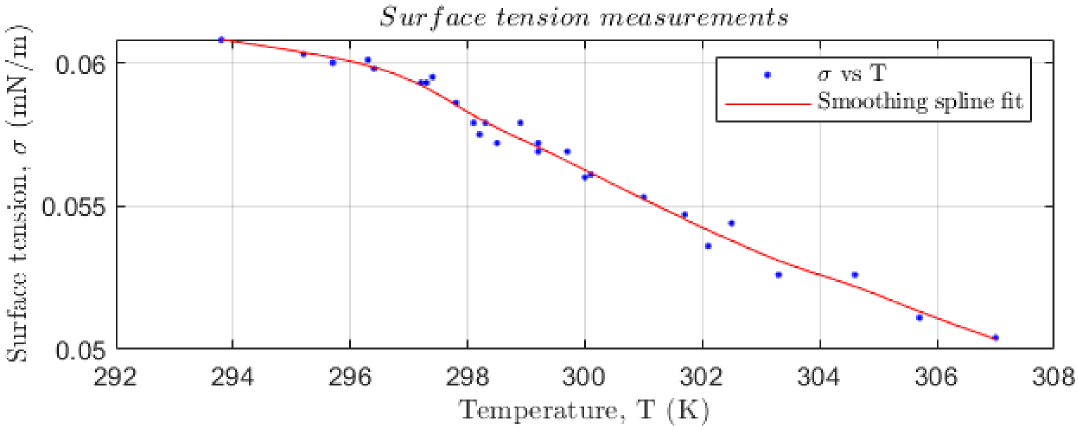

Figure 3.9: Smoothing spline fitting of experimental data for a 72.5% glycerol – 27.5% tap water mixture's surface tension.

to values around 50 mN/m, 29 % lower than our assumptions considering clean tap water (around 70 mN/m). The solution we proposed conveyed keeping the correlations from tabulated data for density and viscosity, which became eventually remarkably similar to our measurements, and performing a new correlation for surface tension. For this purpose, we obtained new surface tension data for our mixture using a calibrated tensiometer and executed a new bidimensional fit for surface tension vs temperature, as shown in Figure 3.9.

(a)

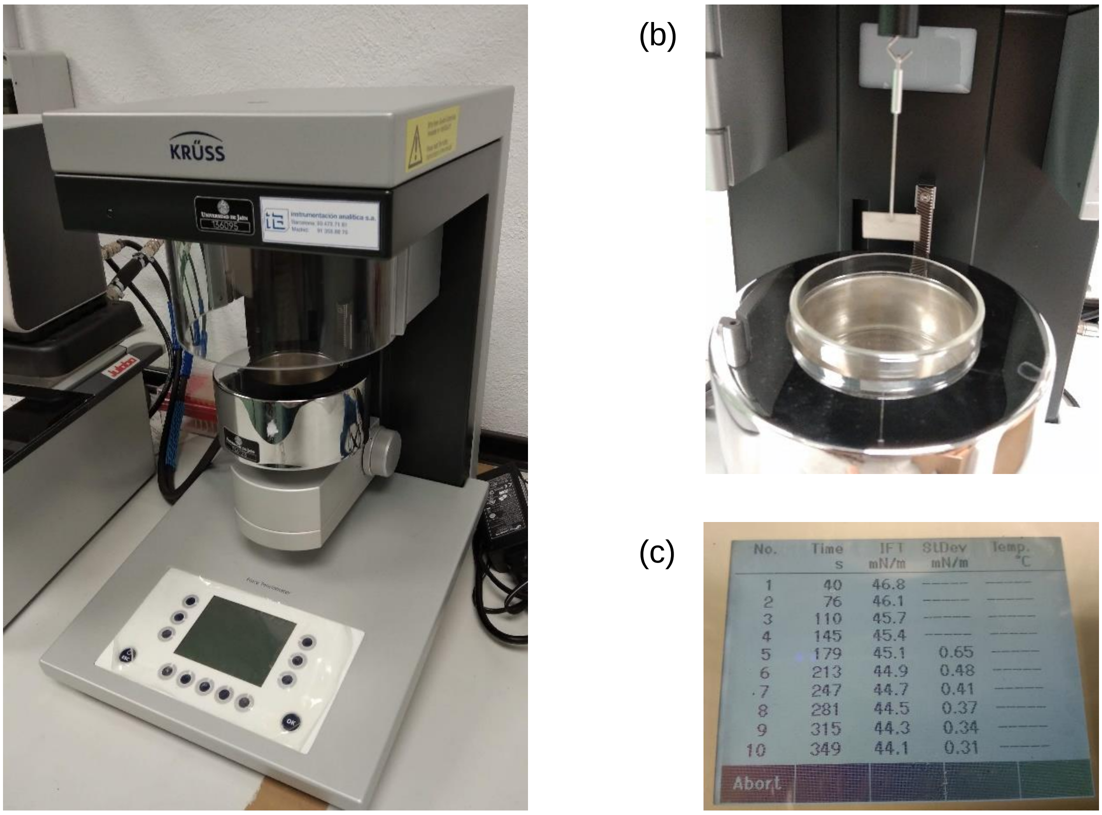

Figure 3.10: (a) KRÜSS Force tensiometer – K20, (b) Wilhelmy plate for surface tension measurement, (c) Example of surface tension measurement.

The surface tension data was measured with a KRÜSS Force Tensiometer – K20, shown in Figure 3.10 (a). The measuring method was Wilhelmy plate method, which consist of slightly submerging a plate of perfectly known dimensions (Figure 3.10 b) in the liquid of unknown properties. The tensiometer will measure the minimum necessary force that it takes to extract the plate of the liquid, thus obtaining a value of surface tension. Ten tests are performed and an average value is provided with a standard deviation under 0.1 mN/m, as shown in Figure 3.10 (c).

Some surface tension measurements were verified using a simple experiment based on a simplification of Tate's law [38] – [39]. This law defines "Tate Volume" (V_T) as the volume of a drop formed in a sufficiently small orifice from a balance of buoyancy and capillary forces with a departure contact angle in the region of 90° such that:

$$V_T = \frac{\pi d_o \sigma}{(\rho_l - \rho_g) g} \rightarrow \sigma \approx \frac{mg}{\pi d_o}$$

Equation 3.1: Tate's law, surface tension estimation in the case of a single drop coming out of an injector.

Where d_o refers to the outer diameter of the liquid injector, σ is the liquid's surface tension, m is the mass of one drop and ρ_g and ρ_l are the density of the gas (air, negligible) and liquid respectively.

Figure 3.11: Experimental set-up for surface tension assurance based on Tate's law.

In our experiment, we would fill a small tank with an undetermined amount of liquid, letting it drain drop by drop through a small centred orifice where we would place a hypodermic needle of known inner and outer diameter. The amount of liquid in the tank would be enough for the pressure gradient due to emptying to be negligible. We would let the tank empty until a sufficient amount of liquid for it to be weighted on a common scale had been collected. While the tank emptied, we would count how many drops came out of the tank and then we would apply Equation 3.1 as for the average weight of all the drops (weight of the collected liquid $m_T \cdot g$ divided over the number of drops n_d).

$$\sigma \approx \frac{m_T g / n_d}{\pi d_o}$$

Equation 3.2: Simplification of Tate's law as for our experiment, estimation of surface tension in the case of multiple drops coming out of an injector based on the average weight of one drop.

This methodology may present large errors in case of using a single drop. However, we would count up to 130 to 200 drops, what led us to a reasonable drop average weight and provided results really close to expected for all types of fluids. Here is an example of the methodology for the water – glycerol mixture used in the spiralling regime experiments.

Water – Glycerol (72.5 % GLYC) Temperature: 26.7ºC			
Experiment		**Surface tension**	
n_d	183	**Fitted value**	56.408 mN/m
m_T	3.84 g	**Experimental (Tate's law)**	51.576 mN/m
Needle gauge	18	**Absolute deviation**	0.00483 mN/m
d_o	1.27 mm	**Relative deviation**	8.566 %

Table 3.4: Results of simplified Tate's law experiment for surface tension estimation of a mixture of glycerol (72.5 %) and water (27.5 %) at 26.7ºC.

3.2.3. Summary of performed experiments

Summarizing, we performed six types of experiments by changing the bubble size (hence the liquid and Bo, Ga, Re, Mo) and the distance to the wall (L). This way, we were able to analysed the three principal regimes (rectilinear, zigzagging and spiralling paths) at three different wall distances. The properties of every analysed bubble can be found in the following tables:

Case	Liquid	ρ (kg/m^3)	μ (mPa·s)	σ (mN/m)	D (mm)	d (mm)
I	T11	923.04	9.60	20.00	3.075 - 3.194	2.35
II	Glycerol-water mixture 72.5%	1183.50-1184.50	55.29-57.00	18.80-19.89	6.344 - 10.894	14.60
III	T05	913.00	4.565	19.70	2.675 - 2.812	2.00

Table 3.5: Problem variables for the performed tests: liquid properties, bubble diameter and nozzle diameter.

Note in Table 3.5 that a different fluid was used apart from the aforementioned silicon oils, precisely a glycerol-water mixture for the spiralling regime. The reason for not using silicon oil was its capillary length, which can be calculated as for Equation 3.3, where σ is the surface tension of the fluid interface, g is the gravitational acceleration and ρ is the density of the fluid [16].

$$l_\sigma = \sqrt{\frac{\sigma}{\rho g}}$$

Equation 3.3: Capillary length of a fluid

The minimum Bond number to reach the spiralling regime required an inlet of 7.784 mm, while the capillary length of the original silicon oil is 1.48 mm, providing a maximum injector diameter of 2.96 mm, what means that a larger nozzle would have led to the bubble not forming, but the liquid coming into the air line. For this reason we decided to use a small orifice covered by a repelling substance that would let us create large bubbles [16]. However, the found oleophobic treatments did not suit the experimental conditions, so we opted for a hydrophobic one (which would not repel T11 but would repel a water-based mixture of similar properties. This mixture was selected for the same Morton number as the corresponding silicon oil (T11), although this target could not be operatively achieved due to unpredictable changes in the laboratory conditions, especially temperature.

Case	Regime	Bo		Ga		Mo		Re
		target	real	target	real	target	real	real
I	rectilinear	5.0	4.4	59.61	54.4	$9.9\cdot10^{-6}$	$9.8\cdot10^{-6}$	54.3
II	spiralling	10.0	8.3-24.4	100.25	97.1-215.7	$9.9\cdot10^{-6}$	$6.1\cdot10^{-6}$-$7.0\cdot10^{-6}$	86.9-153.9
III	planar zigzag	4.0	3.3	100.8	88.4	$6.2\cdot10^{-6}$	$6.2\cdot10^{-6}$	-

Table 3.6: Experimental parameters describing the performed tests: regime and dimensionless numbers.

Note also that the conditions of the fluids present slight changes compared to the data provided by Zenit et al. [33] and the fluid supplier. The fluid properties shown in Table 3.5 were measured parallelly to the experiments to discard severe differences to target due to the uncertain laboratory conditions and their susceptibility to temperature changes.

3.2.4. High-speed images acquisition

With the installation previously described the wanted conditions could be satisfactorily achieved, hence the next step comes to data acquisition. For these experiments high speed imaging techniques were utilized. Two cameras (FASTCAM SA1.1 and FASTCAM MINI AX200 respectively) were installed around the tank, each of them opposite to one of the tank's surfaces and orthogonally to each other (see Figure 3.12). This arrangement provided images both in the plane of the wall (we will refer to it as PLANE 1 in the following) and in the perpendicular one (PLANE 2), achieving a full knowledge of the bubble movement. Furthermore, cameras were synchronized and checked for correct alignment at the beginning of every set of experiments to guarantee that the acquired data was reliable (each set involved 4 to 5 experiments with identical conditions to assure repetitiveness of the results). A Sigma MACRO 105 mm F2.8 EX DG OS lens was chosen for each camera. This model was selected because it provided enough focusing depth so that the captured images remained focused even though the bubbles moved away from the initially focused position. The achieved spatial resolution ranged from 17.79 to 36.31 μm per pixel.

(a) (b) (c)

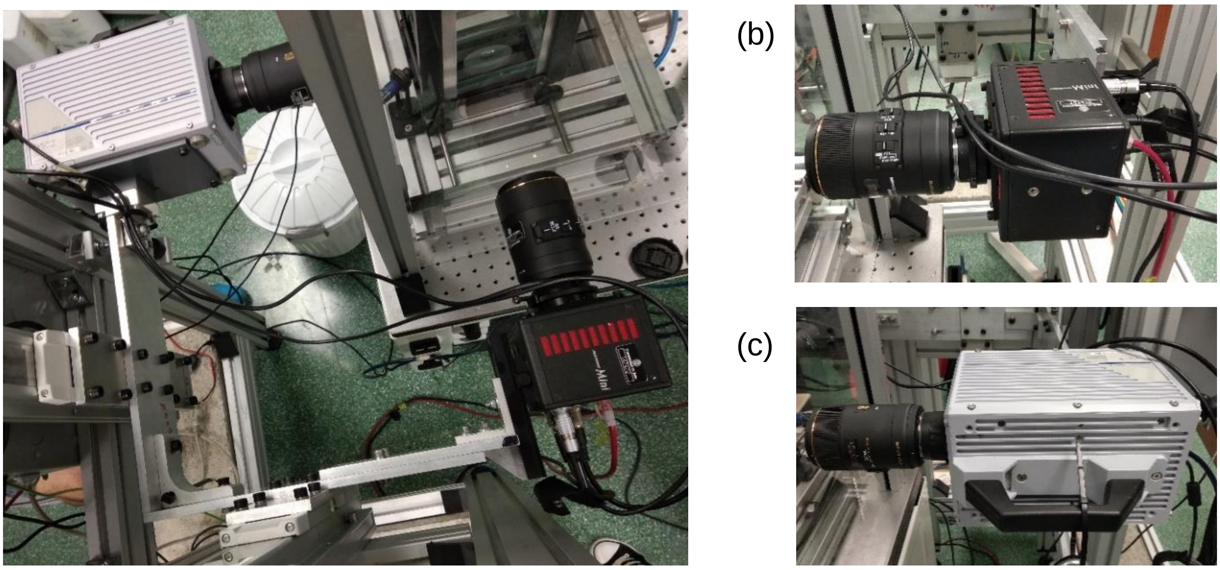

Figure 3.12: (a) Cameras relative position, placed perpendicularly to each other, both mounted with their respective Sigma MACRO 105 mm F2.8 EX DG OS lens, (b) Model FASTCAM MINI AX200, (c) Model FASTCAM SA1.1.

(a) (b)

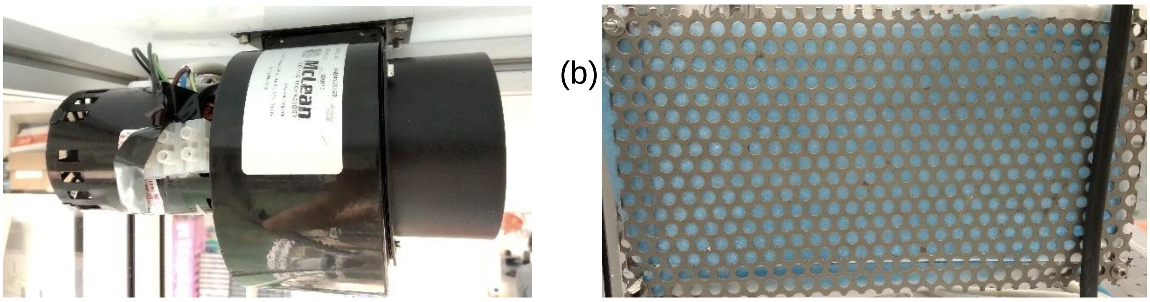

Figure 3.13: (a) Fan and (b) filtered air inlet for temperature changes mitigation.

Experiments were recorded at speeds of 2000 to 3000 frames per second (fps), thus a direct source of light was necessary opposite to the cameras for providing sufficient contrast for the recorded images. In this way, bubbles obstruct light and their shadow can be captured. Two 1200 x 300 mm^2 LED lamps were constructed using LED stripes and 300 W drivers for this purpose (Figure 3.14). These electronic devices perturbed fluid temperature due to a fast heat dissipation, hence a fan and a filtered air inlet was installed on the coverage of the experimental facility to provide a more constant temperature (see Figure 3.13).

(a) (b)

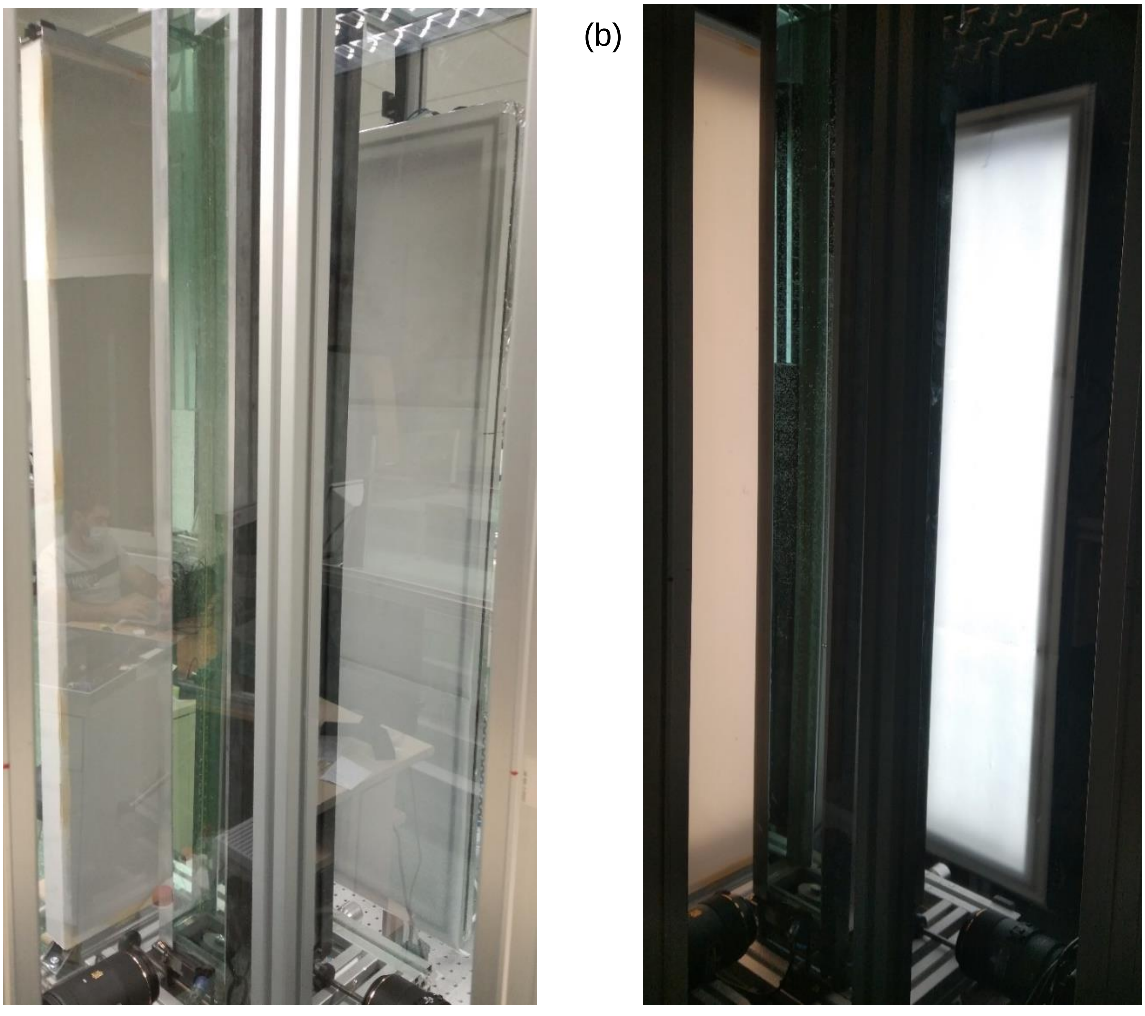

Figure 3.14: LED lamps (a) OFF and (b) ON, placed opposite to the cameras.

The rise of the bubble was captured by moving the cameras vertically at the same time. This task was developed utilizing an AC servomotor and two linear guides. The cameras were installed on the linear guides using a steel plate which provided the necessary separation and orientation, while the motor provided the necessary torque for them to move along the guides. This motor was controlled using a SMC LECSA2-S4 driver and the software MELSOFT MR Configurator 2 Version 1 [40]. This software enabled us to program the wanted position, velocity and acceleration of the cameras along time and download this information into the servomotor driver. Activating the driver's automatic mode, we could control the beginning of the program execution using digital inputs connected to a triple toggle switch station.

(a)

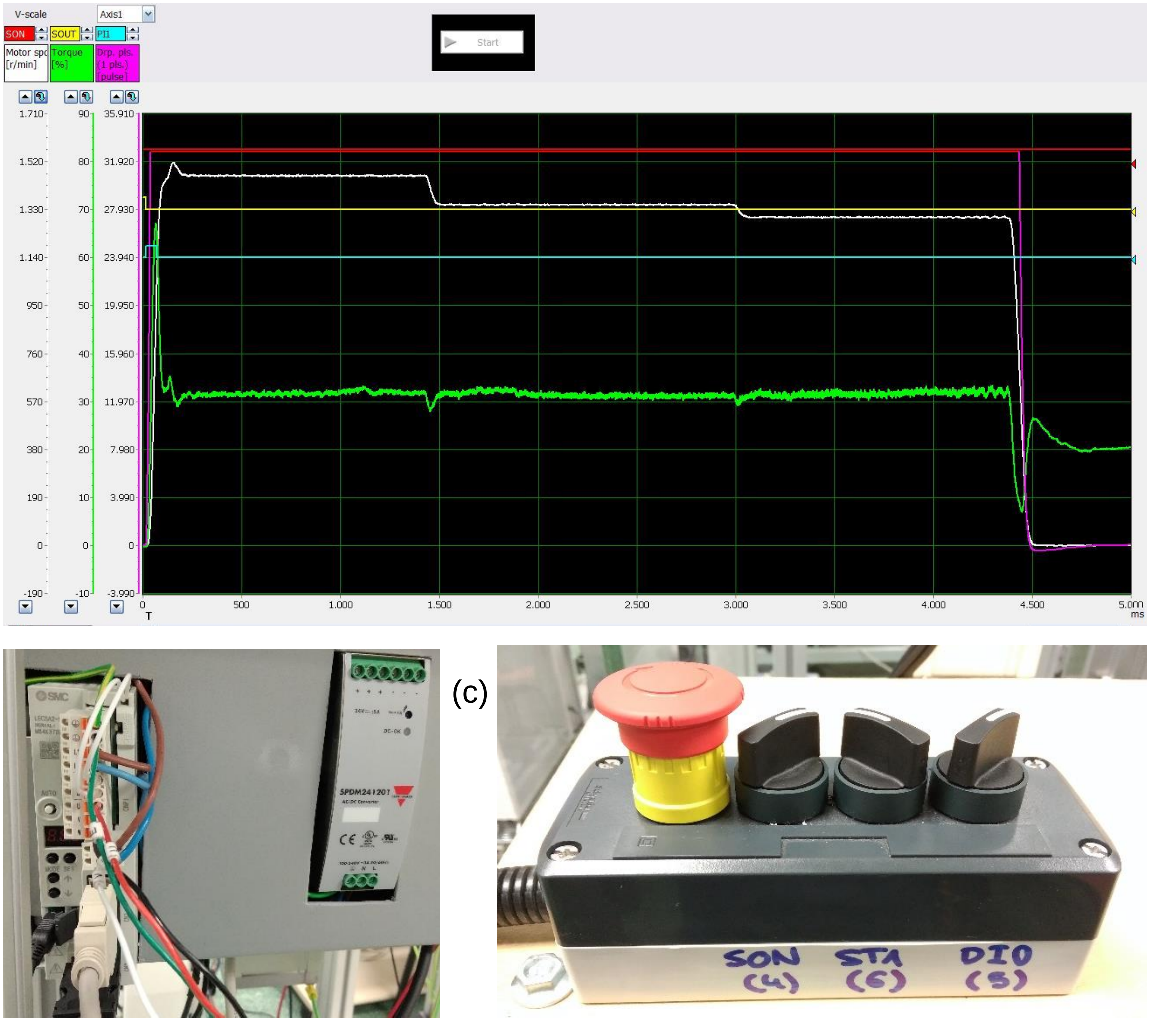

(b) (c)

Figure 3.15: (a) Graph showing motor movement control (velocity control in white, program activation input in blue, resulting torque in green), (b) Servomotor driver LECSA2-S4 and programmable controller (PLC), (c) Triple toggle switch station for motor control.

Figure 3.15 (a) shows the result of motor control. In this example (which can be found as an appendix for a more detailed command description), initial values of acceleration, deceleration and constant rising velocity are loaded into the program in the first place. Then, a command number of pulses must be introduced under a gain of 10 μm/pulse for the desired rising displacement. When all variables are initialized, motor movement is started by signal PI1 (blue), which is activated by bubble detachment. Motor accelerates at the specified pace until reaching the target velocity. Nevertheless, this velocity may not be ideal for all the trajectory, especially for large bubbles, whose deformation, hence deceleration, is remarkable. For this reason, this example shows that new velocities and command positions can be introduced in the middle of the trajectory, providing that the motor either fully stops and restarts a new movement or (like in this case) only decelerates until reaching the new command velocity. Figure 3.15 (a) shows a trajectory of 1 m height divided in three sections characterized by three different velocities (white). This system made bubble recording easy and quick, which allowed us to perform at least five repetitions of each case (three different bubbles at three different wall distances) to assure reproducibility.

To ensure that the captured images corresponded to the bubble trajectory and to avoid blank frames, a photodiode sensor was installed and connected both to the cameras and the motor driver (see Figure 3.16). This signal was activated when the bubble passed in front of the sensor, hence both recording and cameras movement could be programmed to begin at the same instant when bubbles detached from the nozzle. For this purpose, emitter and receiver had to be placed opposite to each other

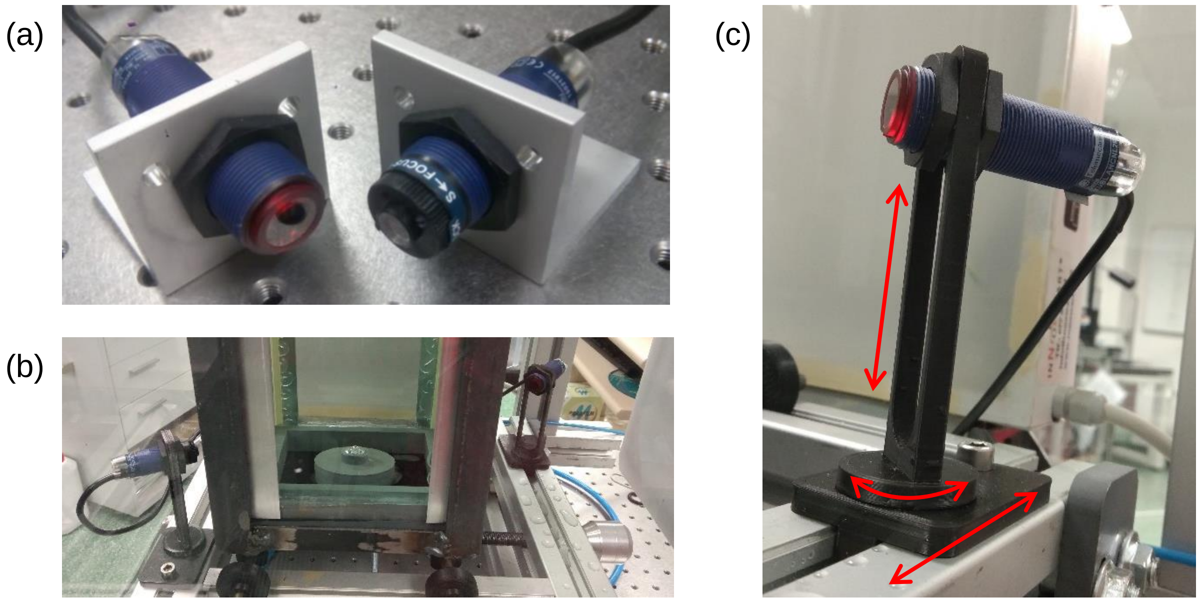

Figure 3.16: (a) Photodiode emitter (right) and receiver (left), (b) Emitter and receiver relative position at platform corners, (c) Support twisting device for sensor positioning.

and cutting the bubble at detachment. However, they could not be placed in front of the cameras, as they would have created a shadow impeding images acquisition. For this reason, a twisting device was fabricated using additive manufacturing techniques, allowing to place emitter and receiver in opposite corners of the base platform, where they caused no light obstruction.

These linear guides were mounted on a weighted structure created specifically for this experiment around the experimental facility. The structure incorporated plastic levelling feet that allowed to assure the vertical movement of the cameras (see Figure 3.17 a, b).

(a) (b) (c)

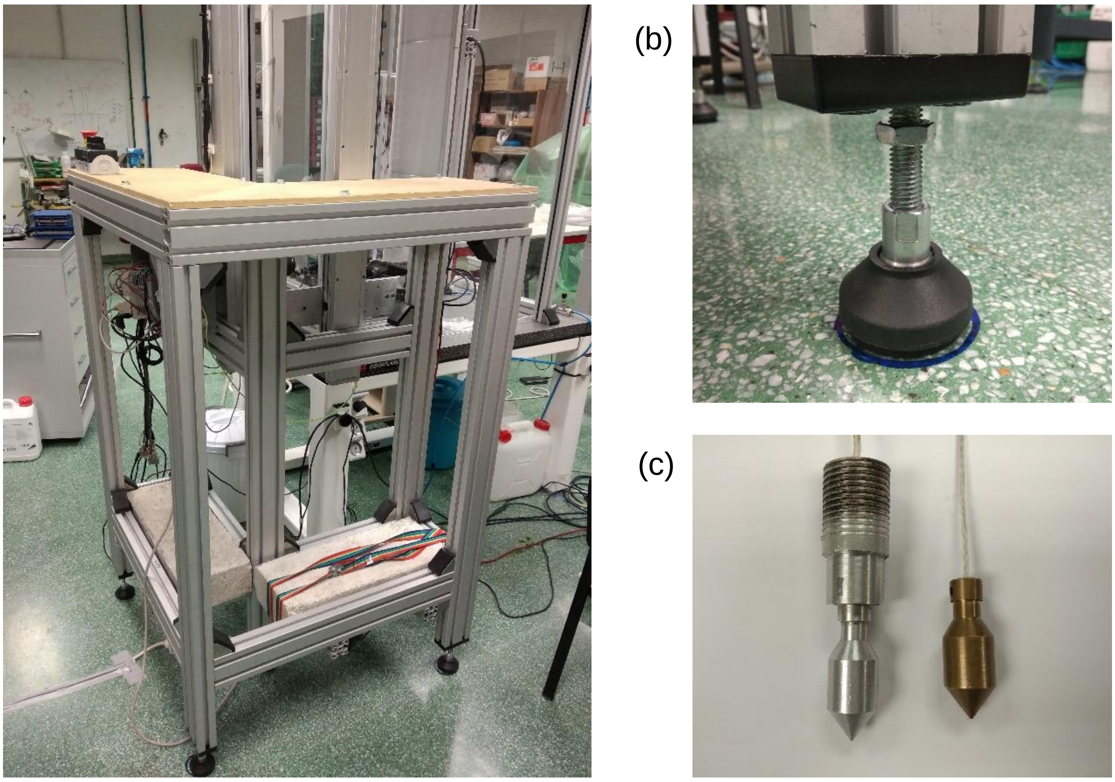

Figure 3.17: (a) Structure for cameras and motor support and movement, (b) Plastic levelling feet, (c) Plumb bobs used for verticality assurance.

Once placed in the position that offered the maximum spatial resolution when recording, concrete blocks were added to the base of the structure, assuring minimum displacement from its optimal location. Verticality tests were performed by recording a hanging plumb bob opposite to each camera while levelling the structure's feet until no movement of the plumb line could be appreciated along the trajectories of any of the cameras (Figure 3.17 c).

3.3. Data processing

Each experiment offered as a result a set of consecutives images on each plane (4000 to 5457 frames on PLANE 1 and 7800 to 8800 frames on PLANE 2, differences are due to the limited memory of the cameras). These images were digitally treated using an in-house MATLAB® code (see Appendix B for further details in utilized functions and commands).

The first step came to initializing the experiment conditions, hence writing into the program the values for video name, number of frames, recording velocity, recorded plane, spatial resolution provided by the camera, wall distance L^*, size of the air nozzle and used fluid.

After that, the routine consisted on the application of several segmentations to every image consecutively. This segmentation will isolate the bubble’s shadow so that its shape and position can be precisely determined, as shown in Figure 3.18 (f). To achieve the desired contour an adaptive threshold is applied that creates a mask containing the brighter sections of the image. Nevertheless, the bubble’s shape will appear as a dark area, hence this mask must be inverted. The mask is slightly dilated to avoid the volume minimization described in Bongiovanni et al. [29] and then the rest of the dark areas (mainly at borders, rectangles showing video information coming from the image acquisition program) are eliminated. Finally, the bright hole that appears inside the bubble due the reflection of rays coming from the light source [29] must be filled so that the complete frontal area of the bubble is considered in the rest of the analysis.

Once the mask is applied to an image, more than one bright area may appear, thus it must be filtered and only the bubble area must be selected. The filters applied limit solidity, area (in pixels) and major axis length of the bright areas present in the masked image so that every bubble recorded can be detected regardless of its shape, size or deformation. After the area of interest is isolated, the routine automatically extracts from the image the information for the bubble’s boundaries, area and centroid coordinates of the frontal area (in pixels). All this information is translated into millimetres applying the provided spatial resolution, allowing us to calculate the volume as an average of the revolution in 2π radians around the centroid axis of each half of

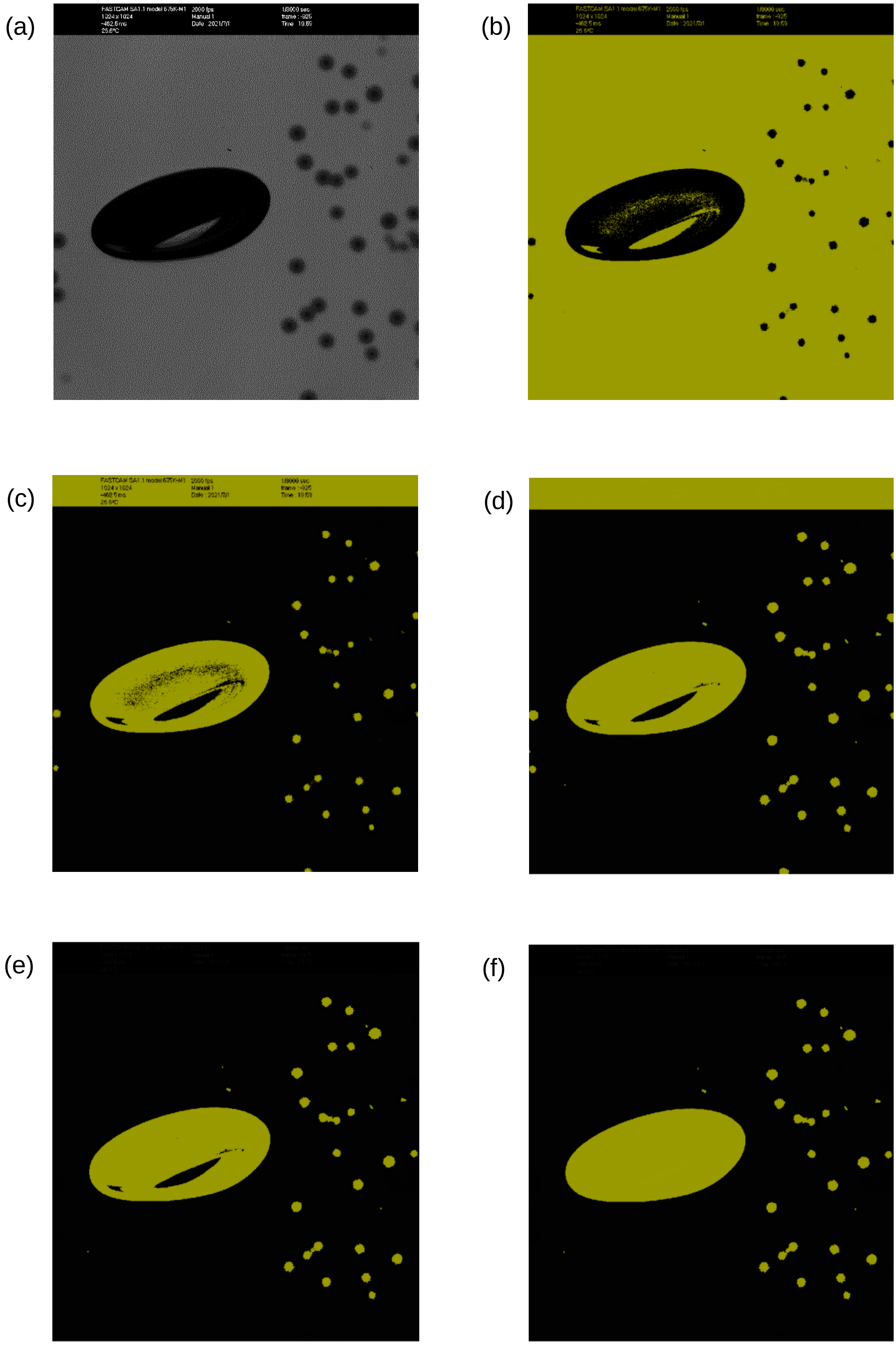

Figure 3.18: Image segmentation process from (a) original to (b) dividing threshold, (c) mask inversion, (d) mask dilation, (e) elimination of borders and (f) holes filling.

the contour, which is a fair approximation as long as bubbles are considered axisymmetric. After that, the bubble centroid can be calculated considering an average between the information of both planes.

When the complete set of frames has finished the previous processes, the centroid trajectory must be corrected. As the full bubble movement is recorded at once, by rising the motor along with it, the detected centroid will have only barely moved, it will always be contained in a reduced range of coordinates because the relative velocity between the motor and the bubble is kept at its minimum to avoid blank frames and guarantee that the bubble appears in every recorded image. Thus, in order to calculate the accurate position of the bubble at every instant, the position of the motor guides at the same moment must be added to the centroid vertical coordinate. These positions could be easily extracted from the servomotor software, as shown previously in Figure 3.15 (a). A data set of 11526 points in five seconds are recorded and a smoothing spline is used as means of interpolation. As the recordings are perfectly synchronized with the motor movement, time can be used as independent variable for the motor positions interpolation.

Eventually, the diameter is calculated using the equation for the volume of a sphere so that the dimensionless parameters describing the problem can be derived and compared to target. Finally, all the obtained data is saved for future treatment and explicatory graphs generation. A summarizing block diagram of the full digital imaging process can be found in Figure 3.19.

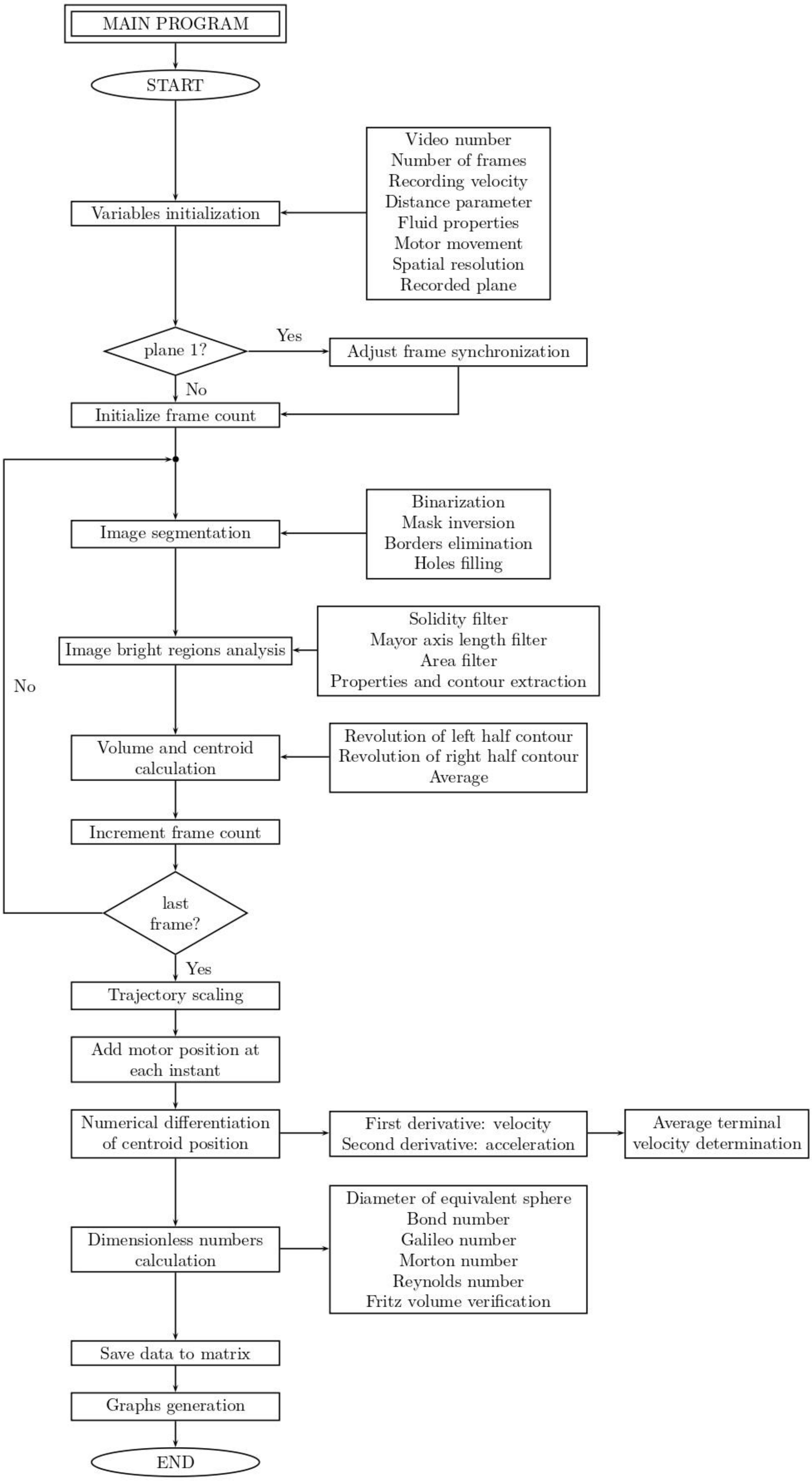

Figure 3.19: Main MATLAB® routine and subprograms flow diagram, commands details in Appendix B.

4. OBSERVED RESULTS

In this section we will analyse the observed bubble properties and trajectories as well as the derived velocities and accelerations. We will compare the case without the wall to the references cases by in Cano-Lozano et al. [18] and then we will observe the main differences induced by the presence of the wall and the distance parameter L^*. This parameter was set to three different values, namely 1, 2 and 4, so that the limit of the wall influence could be approximated.

4.1. Case I: rectilinear regime

For the bubbles in the rectilinear regime (reference case 22 in [18]) the experiments offered results like in Figure 4.1, where a clear migration away from the wall can already be observed even with a bare eye. These experiments are characterized by target dimensionless numbers Bo = 5.0, Ga = 59.61, Mo = $9.9 \cdot 10^{-6}$ and L^* = {1, 2, 4}.

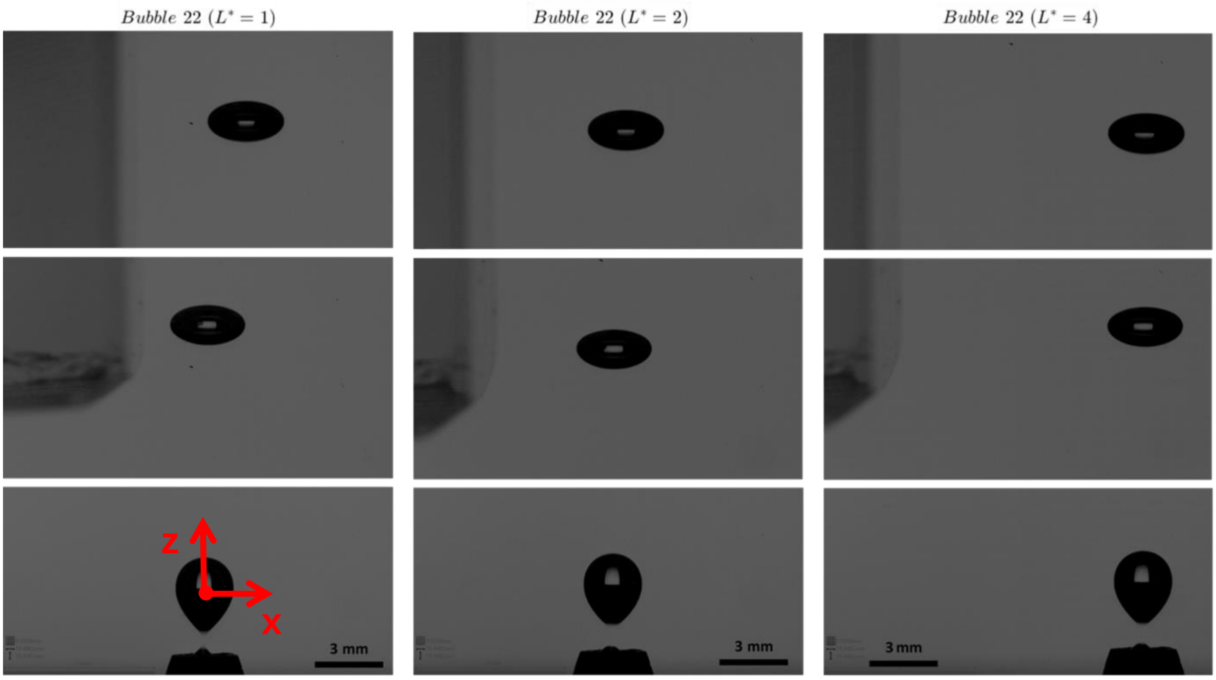

Figure 4.1: Experiments for case I: rectilinear path at different values of L^*, namely 1, 2 and 4 (left to right).

After processing the full trajectories, the paths shown in Figure 4.2 were obtained. We will only report cases where the bubble is affected by the wall, as rectilinear bubbles have been deeply studied and observed in previous researches, like references [11] – [13] – [18] – [20] and have no further interest in this sense. For this reason, the rectilinear case without wall was only used as a validation of the experimental procedure.

To simplify these experiments, only one plane was recorded (PLANE 1, perpendicular to the wall), as no movement was expected or observed in the orthogonal direction. Hence, the trajectories are shown in Figure 4.2 attending to dimensionless coordinates $x^* = x/D$ and $z^* = z/D$, where the bubble equivalent diameter, D, has been used as characteristic length.

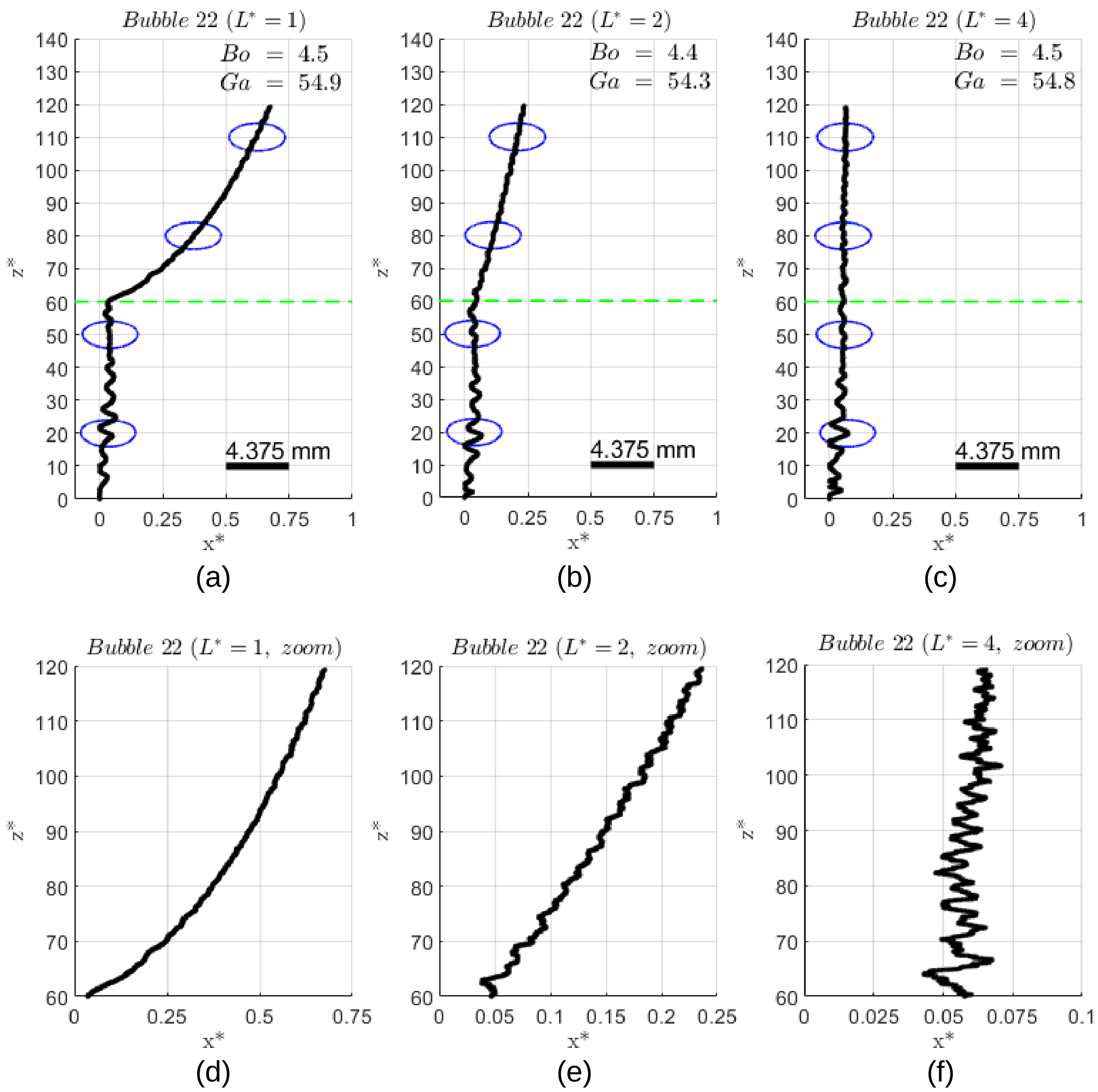

Figure 4.2: Trajectories of bubble 22 (rectilinear regime), together with the bubble contour at certain positions for L^* 1, 2 and 4 (a, b, c respectively). Note that centroid trajectories are depicted in black, while some bubble contours at different heights are shown in blue and the green dashed lines mark the beginning of the wall presence. Zoom of trajectories for wall influence area, indicating maximum bubble displacement at the end of the trajectory (d, e, f). The bubble size is indicated by the scale bar.

Figure 4.2 shows a similar behaviour in the three cases: the bubbles tend to migrate away from the solid surface. The results also report that the proximity of the wall affects remarkably the amplitude of this migration, increasing it and accomplishing a horizontal movement of up to 0.7D while rising only a distance of 60D at the closest value of L^* tested (1) while this value is reduced by a third when L^* is doubled and no significant displacement can be observed when L^* is 4.

Maximum bubble horizontal displacement at $z^* \approx 120$		
$L^* = 1$	**$L^* = 2$**	**$L^* = 4$**
0.67581 D	**0.23622 D**	**0.06541 D**

Table 4.1: Maximum bubble horizontal displacement at $z^* \approx 120$

Finally, an additional result that can be observed is that the migration away from the surface is finite. As shown in Figure 4.2 (a), the horizontal movement of the bubble is not straight, but curvilinear, indicating that it will reach an end at some point and the bubble will continue its rise rectilinearly or maybe in some other path still to be determined. The improvements developed in the experimental facility lately will allow us to repeat these tests for a height of 240D (180D from the beginning of the wall interaction), so the derived trajectories may be completed after the bubbles stops migrating away from the wall in future works. This phenomenon cannot be observed clearly in the cases represented in Figure 4.2 (b) and (c), so repeating these cases will be even of more interest, allowing us to determine whether the migration is finite for these values of L^* too.

Note also that the wall was placed at a height of around 60D for these cases. In numerical simulations of this problem developed by the group, a 60D height has been found to be the lowest position guaranteeing that the target bubble has reached its terminal velocity and has fully developed its path along its movement (rectilinear stability). For a clearer understanding of the wall influence, it was critical that its effect was limited to the region where these conditions were satisfied.

After the trajectories were determined, a centred differentiation was performed in order to determine the bubbles' terminal velocity, which has been made dimensionless with $\sqrt{gD}$, as obtained in section 2, providing a dimensionless comparison, as shown in Figure 4.3.

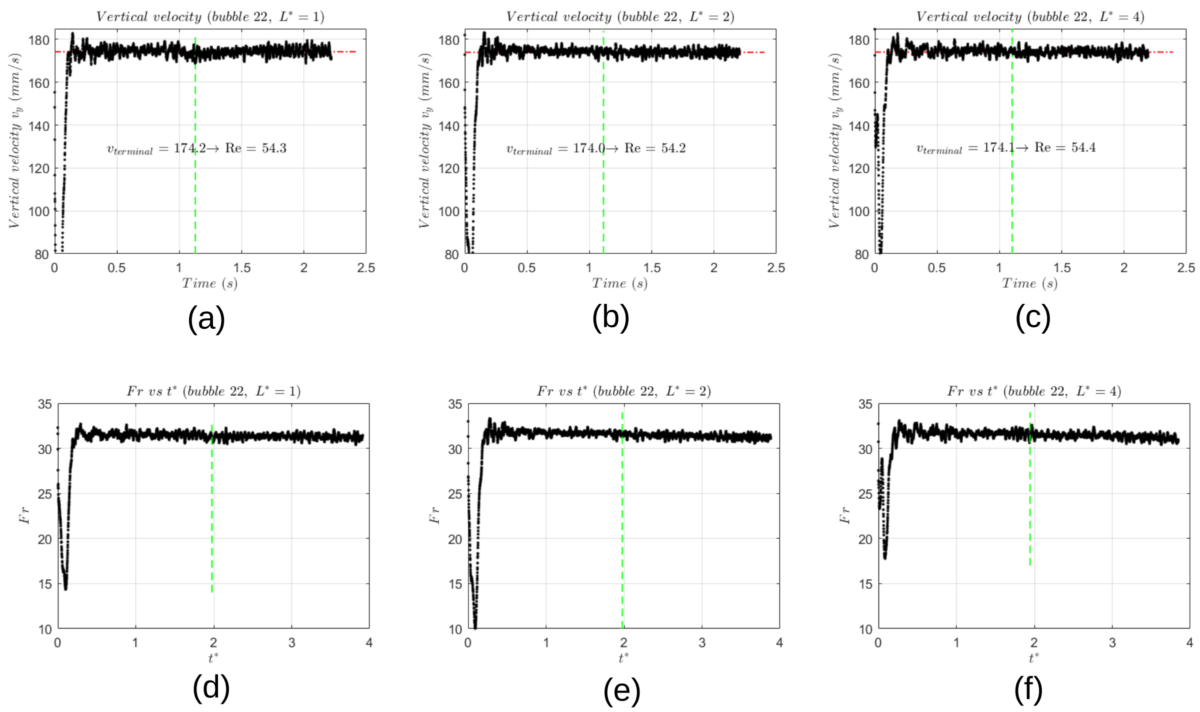

Figure 4.3: Rectilinear regime. Vertical velocity (upper row) and dimensionless vertical velocity $\boldsymbol{Fr = v/\sqrt{gD}}$ (bottom row) as a function of time (made dimensionless as $\boldsymbol{t^* = t/\sqrt{D/g}}$) for L* = 1 (a and d), L* = 2 (b and e) and L* = 4 (c and f). Dashed vertical lines indicate the time at which the bubble reaches the wall.

Figure 4.3 (a to c) shows that the influence of the wall in the terminal velocity of the bubble is negligible, as no oscillations of this value where found in the transition from the beginning of the surface interaction. Note also that the shape of this graphs, showing a remarkably constant value for velocity, are really similar to the reference case (see Figure 1.5). From these results we can also validate that the bubbles had fully developed their paths when the presence of the wall commences, as they show completely constant velocities for a time long enough before this happens. However, when representing Froude number as a dimensionless indicator of velocity (Figure 4.3 d to f), we can appreciate a slight deceleration at the end of the trajectory, especially steep when the wall starts interacting. This deceleration is almost negligible (Froude number is reduced in less than 2%), so we can conclude that the bubble's vertical velocity is almost not affected by the presence of the wall.

Case	$L^* = 1$	$L^* = 2$	$L^* = 4$
Terminal velocity (mm/s)	174.2	174.0	174.1
Terminal Reynolds number	54.3	54.2	54.4
Terminal Froude number	31.3	31.4	31.3

Table 4.2: Summary of vertical velocity indicators for case I (rectilinear regime) and different values of L^*.

Another validation of the terminal velocity (based on Reynolds number, Re = Fr · Ga) can be found in the bibliography, as described by Clift et al. [17]. Figure 4.4 shows a correlation between Reynolds, Morton and Eotvos (equivalent to Bond) numbers. These three parameters can fully describe the problem of a bubble freely rising inside a still liquid (see Equation 2.3), so the correlation will provide a theoretic value for Reynolds number which can be compared to the empirical ones.

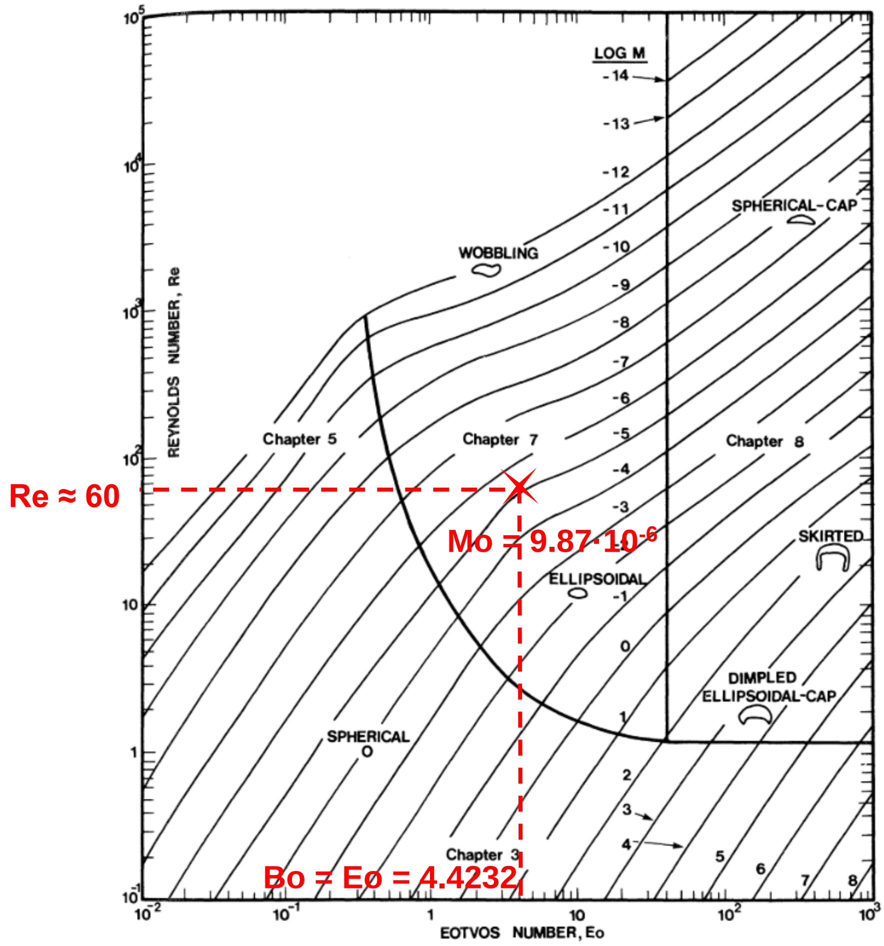

Figure 4.4: Shape regimes for bubbles and drops in unhindered gravitational motion through liquids from Clift et al. [17], theoretical value for Reynolds number for reproduced conditions of bubble 22 without solid wall.

The results indicate that the reproduced values are below the theoretical ones, as the case could not be precisely reproduced (for example, the used nozzle's diameter was 2.35 mm instead of the necessary value of 2.75 mm due to manufacturing reasons). Still, the maximum relative deviations are of the order of 10%, a value quite reasonable for experimental procedures. Thus, we can conclude that even though the case tested is not identical to the wanted one, we are still in the rectilinear regime (even in a more stable case) and the behaviour of the bubble is similar to that expected.

Case	I (experimental)	I (numerical by [18])	Relative deviation numerical (%)	I (theoretic by [17])	Relative deviation theoretic (%)
Bo	4.4	5.0	11.54%	4.4	-
Mo	$9.8 \cdot 10^{-6}$	$9.9 \cdot 10^{-6}$	0.30%	$9.8 \cdot 10^{-6}$	-
Re	54.3	<59.61	<8.89%	60.0	9.48%

Table 4.3: Comparison between numerical and theoretic values of Reynolds number to empirical ones for bubble 22 (rectilinear regime).

Horizontal velocity results are also of great interest, as the horizontal movement caused by the wall is the main novelty introduced in this work. It must be noted that the high spatial resolution achieved when recording (approximately 18 to 36 μm per pixel, depending on the case) introduced much noise in the results after performing the differentiation, hence several filters where tested. In a similar way to that reported by Will et al. [41], the filters tested where applied to the trajectory and then the filtered trajectory was differentiated to compute the velocity values, allowing us to verify that the trajectory was not being distorted by the filter; if the velocity had been directly filtered we would not have been able to detect this problem. Our first approach was to apply a Gaussian kernel because this technique is especially recommended when having to perform differentiations, as it provides high order derivability. Furthermore, a Gaussian kernel had offered satisfying results in [41], where a similar case to ours was analysed (with solid particles instead of bubbles) but it was discarded in our study due to a strong distortion of the trajectories. Eventually, it was found that a moving average filter provided the best noise elimination in velocity while maintaining trajectories almost unaltered.

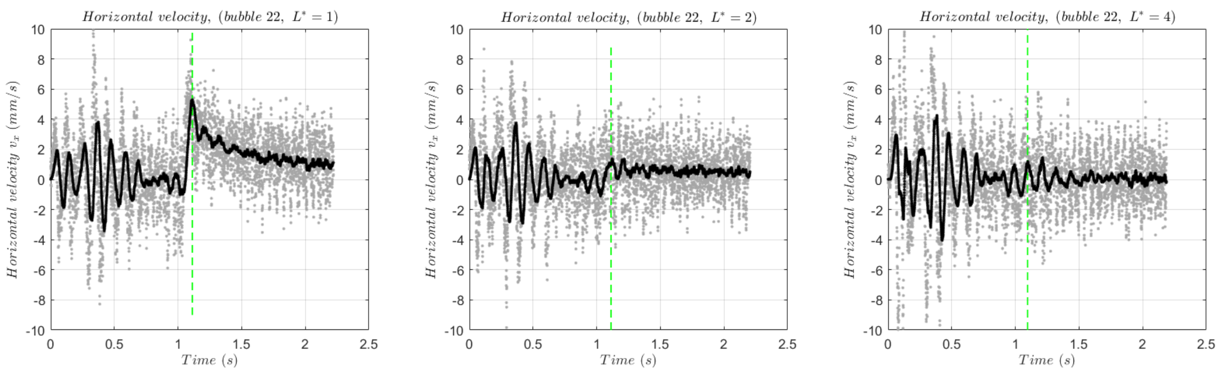

(a) (b) (c)

Figure 4.5: Horizontal velocity of bubble 22 (rectilinear regime) for L* 1, 2 and 4 (left to right). Note that untreated centroid velocity values are depicted in grey, while black dots stand for the filtered results and the green dashed lines mark the beginning of the wall presence.

As shown by Figure 4.5, the bubble slightly oscillates around its vertical axis while developing its path in every case. When the wall appears, the bubble experiences a positive velocity (moves rapidly away from the wall) which can be observed especially clearly for L^*=1. For the rest of the rise, the horizontal velocity decreases but keeps a positive (although small) average value, what indicates it does not stop moving away from the wall in the recorded trajectory, while on a very slow rate. These observations agree with the results obtained from the numerical simulations.

Finally, acceleration values were also calculated in order to obtain the force acting on the bubble. They were computed by applying a second differentiation, but this showed no further interest having found a nearly constant value for velocities, thus providing null results (see Figure 4.6). Furthermore, the force can be more accurately obtained from the numerical calculations, once the simulations are validated.

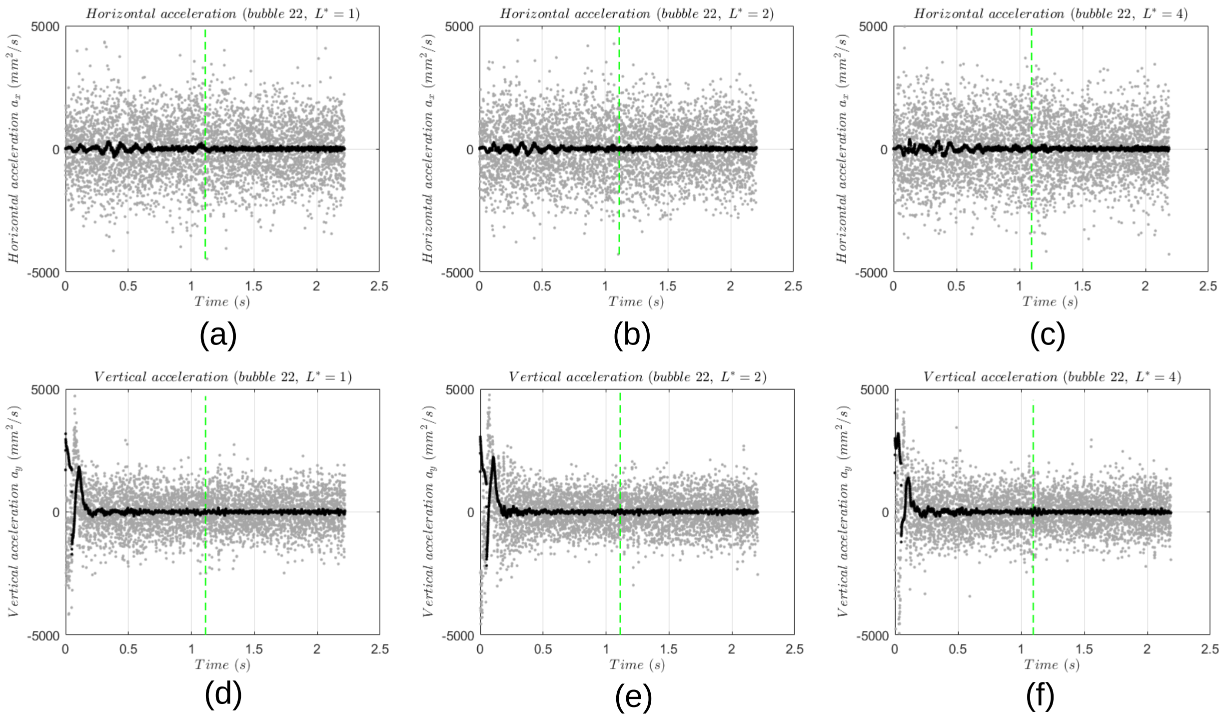

Figure 4.6: Horizontal (top row) and vertical (bottom row) bubble acceleration for experiments in the rectilinear regime (case I, bubble 22) for different values of L^*: 1 (a, d), 2 (b, e) and 4 (c, f).

4.2. Case II: spiralling (helical) regime

As explained before, no experiments for a spiralling bubble have been found to be reported in literature. For this reason, we will first explore the case without the wall and then we will add it and compare to the reference. The experiments were performed using a superhydrophobic injector and a mixture of water and glycerol (27.5 – 72.5 %) in order to replicate case 26 from the reference paper [18].

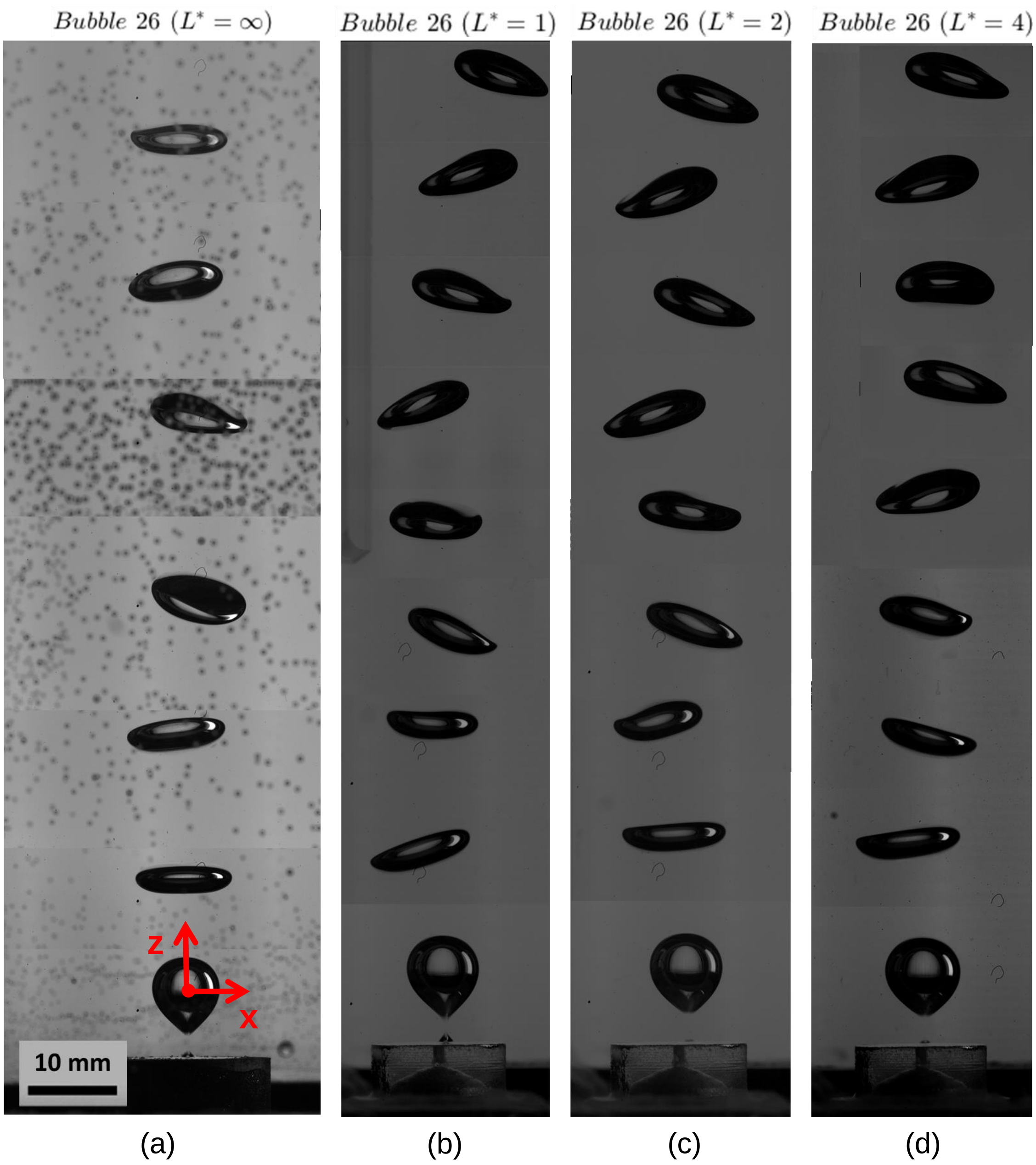

Figure 4.7: Experiments for case II, spiralling path at different values of L*: infinity (no wall), 1, 2 and 4 (left to right). Real images taken from the high-speed movies recorded in PLANE 1 (perpendicular to wall, xz).

Figure 4.7 shows the images obtained from the camera recording PLANE 1 (xz), where the wall is placed at the left of the bubble in b, c and d. Strong shape changes can be appreciated as well as a small migration away from the wall in b. In opposition to these images, Figure 4.8 depicts the images taken in the perpendicular direction (PLANE 2, yz). In this case, no impact by the wall can be observed, although the shapes of the bubbles are similar to the previous cases.

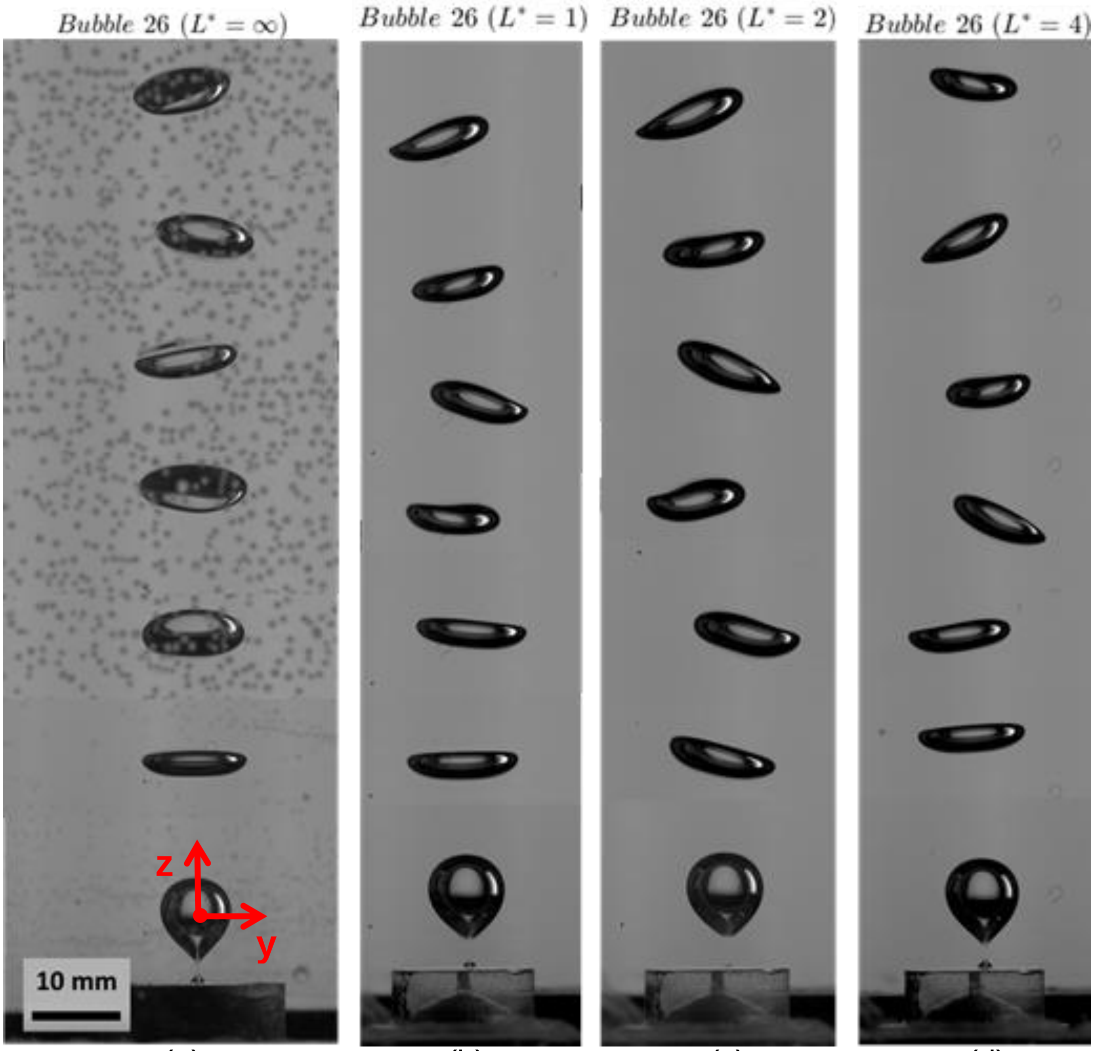

Figure 4.8: Experiments for case II, spiralling path at different values of L*: infinity (no wall), 1, 2 and 4 (left to right). Real images taken from the high-speed movies recorded in PLANE 2 (parallel to wall, yz).

The following figures shows how the bubble behaves for three values of L^* (in black) and how this behaviour changes in absence of a vertical surface (in blue). Note that some of the depicted trajectories do not start at pinch off, but at a higher position, due to the limitation of frames that could be recorded in the camera memory.

The first pictures, (FIGURE) describe the real data extracted from the high-speed videos on each plane, while FIGURE shows a three-dimensional reconstruction of the trajectories. Note that these graphs show the trajectory of the bubble's centroid, extracted from the high-speed images as an average of the frontal area centroid obtained on each recorded plane.

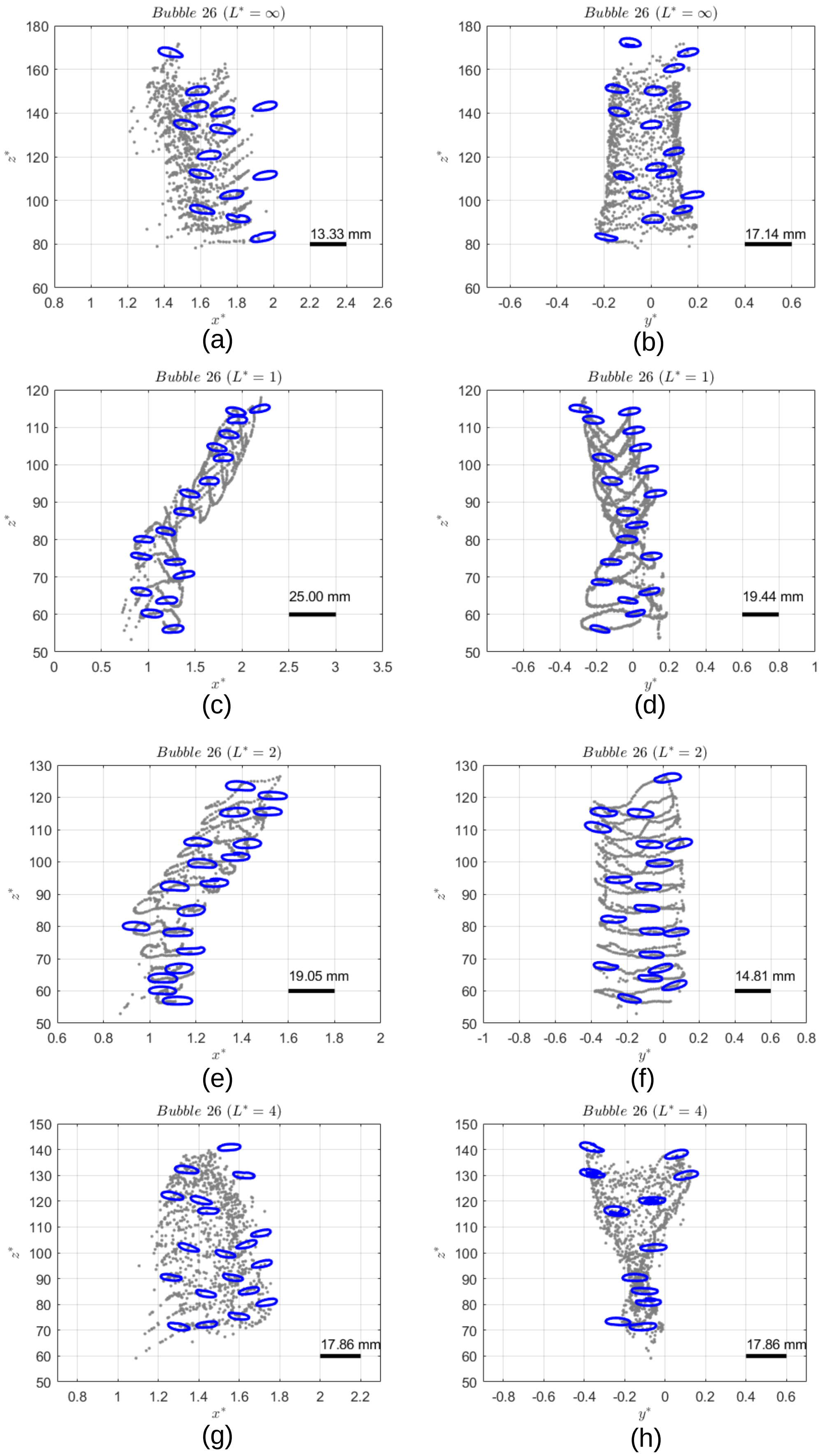

Figure 4.9: Centroid trajectories of the recorded bubbles in case II (spiralling path) for different values of L*: infinity or no wall (a, b), 1 (c, d), 2 (e, f) and 4 (g, h), non-dimensional values (in grey). Shown together, the bubble contour at certain positions at different heights (in blue).

The first observation that should be made is that the desired spiralling path has been achieved, as shown by Figure 4.10, depicting the dimensional trajectory performed in each case. Similarly to the previous rectilinear bubble, a clear migration away from the wall can be distinguished, especially in those cases were the proximity to the wall is maximum. This condition becomes especially apparent when we plot the trajectories with wall (in black) together with the free-rise one (in blue) and noting that the part of the trajectory where the influence of the wall has not appeared yet is depicted in grey.

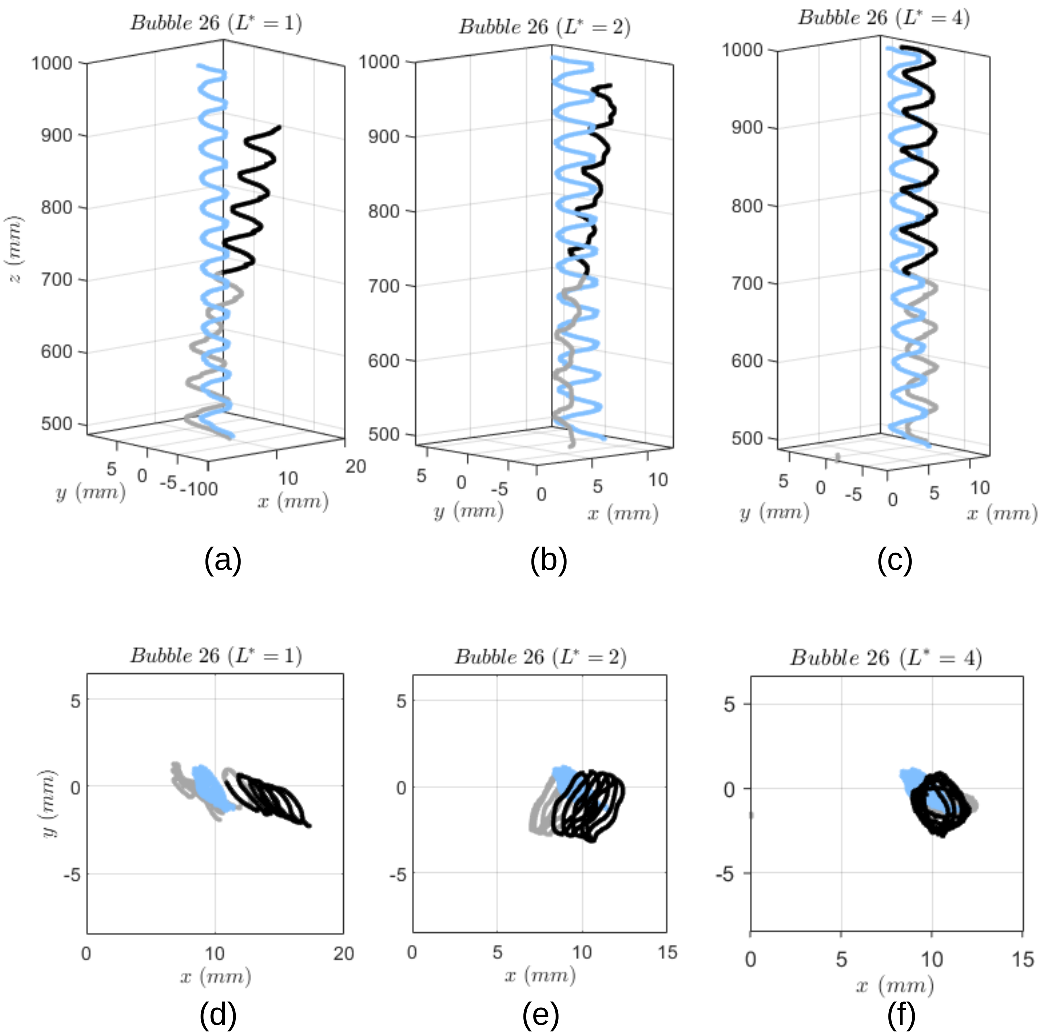

Figure 4.10: Paths of tested bubbles in case II (spiralling path) for different values of L^* (1, 2 and 4 left to right), dimensional values (in grey: below wall and black: above wall) and comparison to case without wall (blue); three-dimensional trajectory (a to c) and top view (d to f).

Note also that the wall was placed at a height of around 85D to 90D for these cases (see Figure 4.11). In numerical simulations of this problem developed by the group, this height has been found to be the lowest position guaranteeing that the target bubble has reached its terminal velocity and has fully developed the spiral path along its movement. For a clearer understanding of the wall influence, it was critical that its effect was limited to the region where these conditions were satisfied.

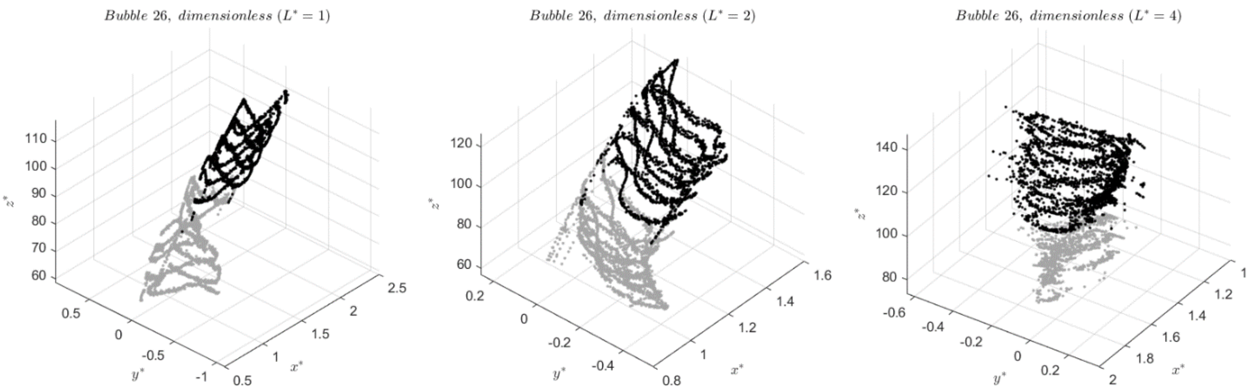

Figure 4.11: Dimensionless trajectories for bubbles in case II (spiralling path) for different values of L* (1, 2 and 4 left to right); in grey (below wall) and black (above wall).

It is important to remark that only the centre of the trajectory appears to be modified due to the presence of the wall, as no changes have been appreciated in the spiral period or radius. The shape of the observed spiral is not as round and stable as what simulations in literature have reported [25] (see Figure 4.12), but these differences are probably due to the changing laboratory conditions and the impossibility to keep them perfectly controlled. For instance, the liquid may be contaminated or the hydrophobic substrate may degrade and form a smaller bubble than predicted.

Regarding velocity, the same method selected for the rectilinear paths has been applied in this case, obtaining the results depicted by the graphs below. The expected behaviour as for the reference case was a quasi-permanent rise velocity that slightly decreases and begins to oscillate when the spiralling movement commences. The red dashed-dotted lines in Figure 4.13 confirm this condition, indicating the average terminal velocity during the oscillations. It can be observed that this value is lower than the stable velocity reached during the first half second of the trajectory

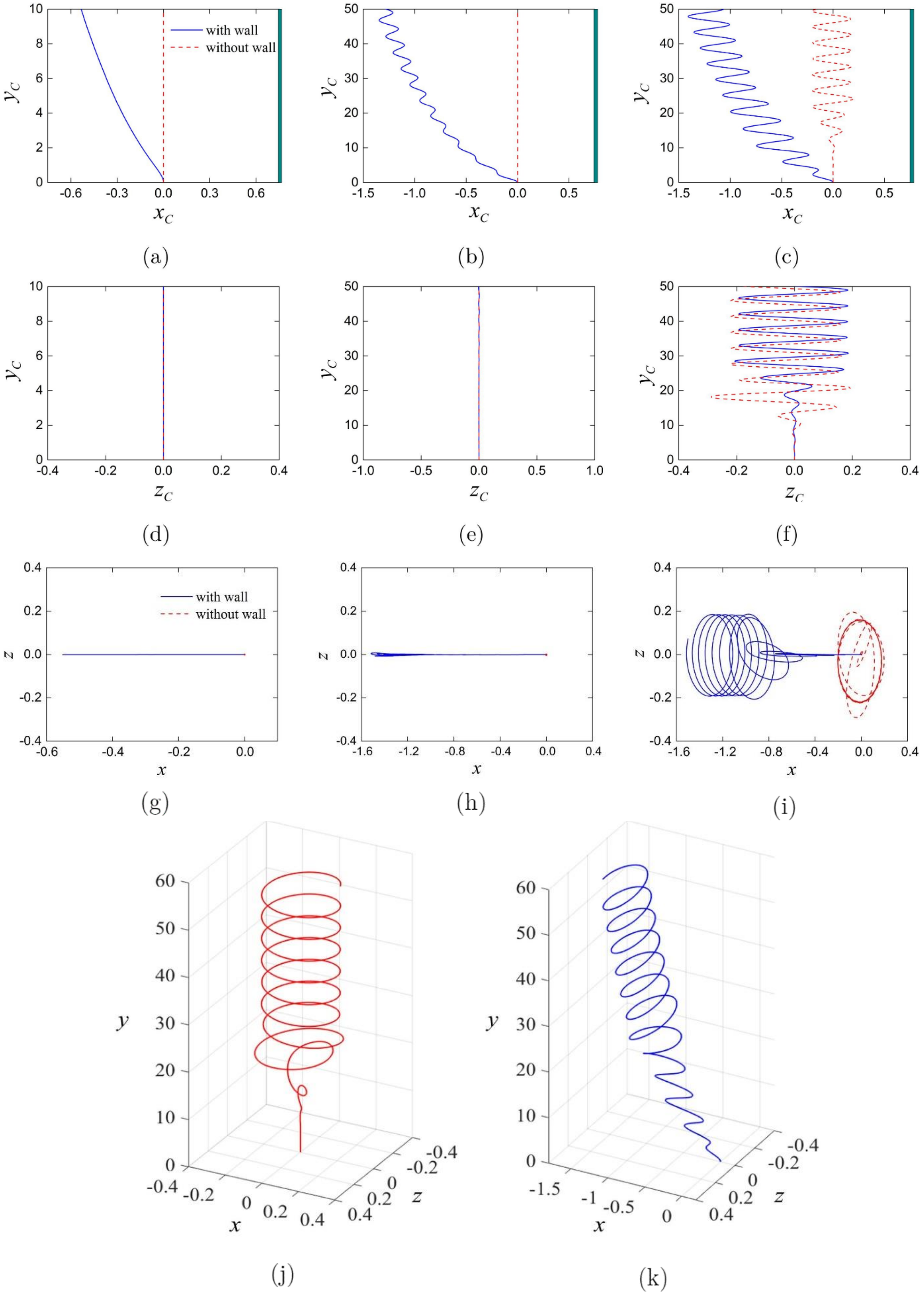

Figure 4.12: Variation of x_C (a, b, c) and z_C (d, e, f) along the vertical path of the bubbles in Zhang et al. [25] released with (solid lines) and without (dashed lines) the wall and top view (g, h, i). The Galilei numbers in each case are (a), (d) =Ga 0.57, (b), (e) =Ga 63.36, and (c), (f) =Ga 90.51. The wall is denoted by the dark cyan region. Pictures j and k depict the three-dimensional trajectories of single bubble for Ga = 90.51 with (k) and without (j) the vertical wall.

No clear impacts of the wall on the rising velocity can be observed, as the trend and average values are of the same order in all cases. However, the wall appears to increase stability and reduce oscillations amplitude, as pointed by Zhang et al. [25], but this is no conclusive because their case study was different, as they imposed the wall interference before the stable path had fully developed (see Figure 4.12).

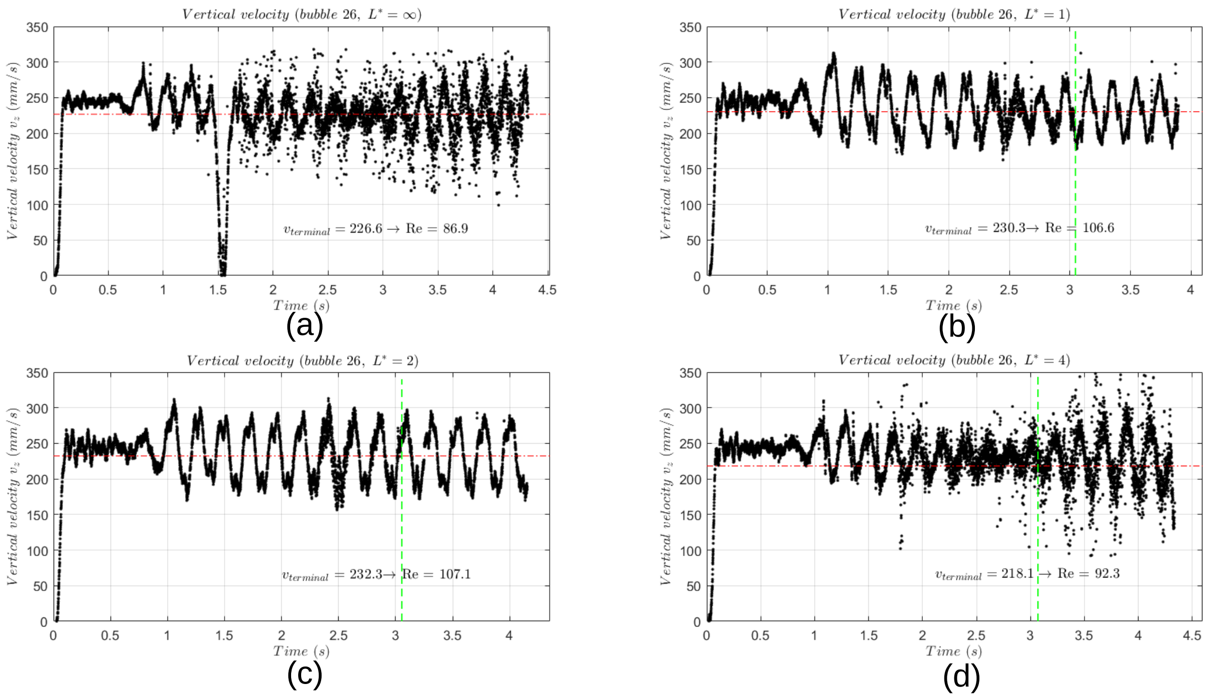

Figure 4.13: Spiralling regime. Vertical velocity as a function of time for L* = 1 (a and d), L* = 2 (b and e) and L* = 4 (c and f). Dashed vertical lines indicate the time at which the bubble reaches the wall.

The following figure will depict Froude number as an indicator of velocity. In the rectilinear case this plot could show more clearly the slight deceleration produced by the wall. Due to the higher amplitude oscillations, this phenomenon is even less appreciable in the spiralling case, so we can conclude that the bubble's velocity is almost not affected by the presence of the wall.

Case	$L^* = \infty$	$L^* = 1$	$L^* = 2$	$L^* = 4$
Terminal velocity (mm/s)	226.6	230.3	232.3	218.1
Terminal Reynolds number	86.9	106.6	107.1	92.3

Table 4.4: Summary of vertical velocity indicators for case II (spiralling regime) and different values of L*.

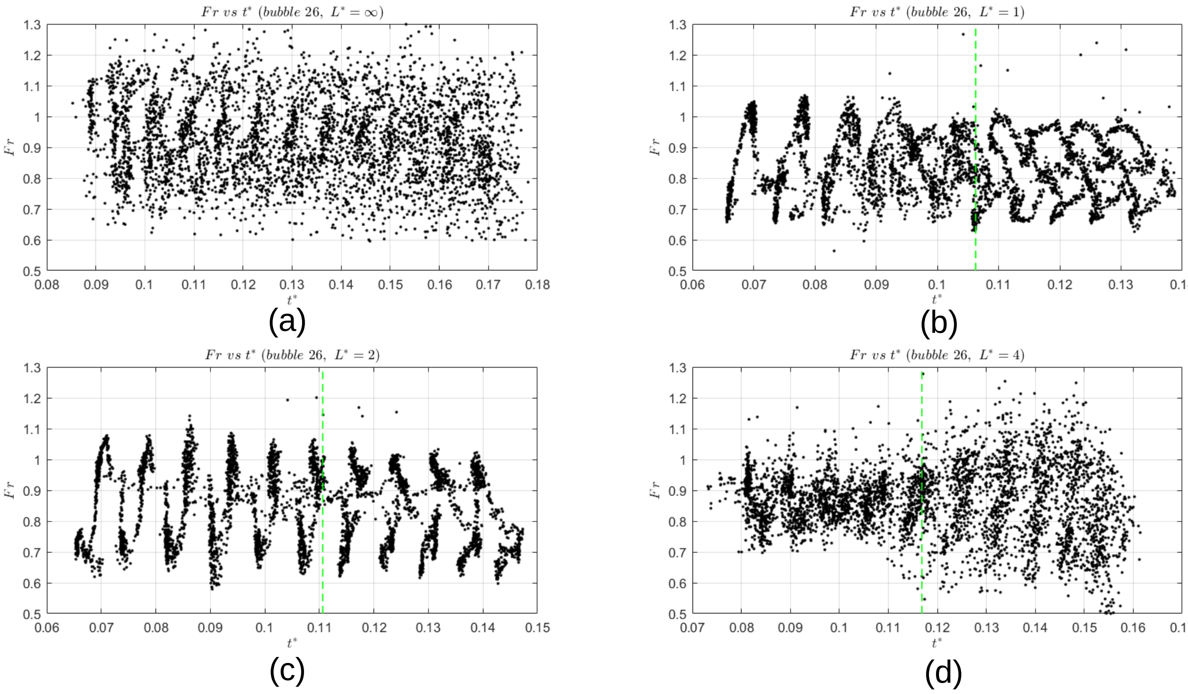

Figure 4.14: Spiralling regime. Dimensionless vertical velocity $\boldsymbol{Fr} = \boldsymbol{v}/\sqrt{\boldsymbol{gD}}$ as a function of time (made dimensionless as $\boldsymbol{t}^* = \boldsymbol{t}/\sqrt{\boldsymbol{D}/\boldsymbol{g}}$) for L* = 1 (a and d), L* = 2 (b and e) and L* = 4 (c and f). Dashed vertical lines indicate the time at which the bubble reaches the wall.

The validation of the terminal velocity by Clift et al. [17] will be applied to the spiralling bubbles too. Figure 4.15 shows a correlation between Reynolds, Morton and Eotvos (equivalent to Bond) numbers, which can fully describe the problem of a bubble freely rising inside a still liquid, providing a theoretic value for Reynolds number which can be compared to the empirical ones.

Case	Π (experimental)	Π (numerical by [18])	Relative deviation numerical (%)	Π (theoretic by [17])	Relative deviation theoretic (%)
Bo	8.3-24.395	10.0	16.67-143.95 %	8.3-24.395	-
Mo	$6.1\text{-}7.0 \cdot 10^{-6}$	$9.9 \cdot 10^{-6}$	29.39-38.08 %	$6.1\text{-}7.0 \cdot 10^{-6}$	-
Re	86.9-153.9	<100.25	13.29-55.55 %	110.0-128.0	<47.25%

Table 4.5: Comparison between numerical and theoretic values of Reynolds number to empirical ones for bubble 22 (rectilinear regime).

The results indicate that the reproduced values are far from the theoretical ones, as the case could not be precisely reproduced. We can conclude that, even though the case tested is very different to the wanted one, we are still in the spiralling regime and the behaviour of the bubble is similar to that expected, with an ellipsoidal to wobbling shape.

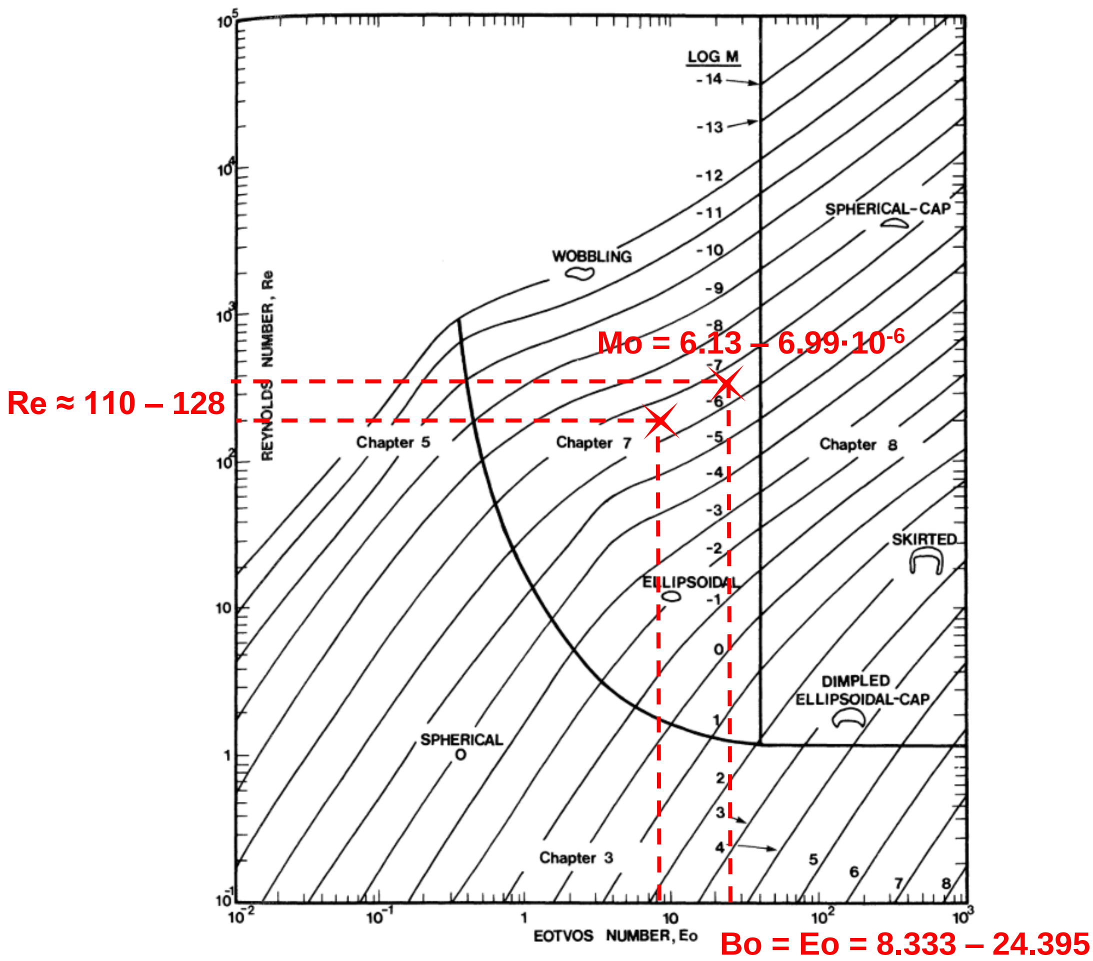

Figure 4.15: Shape regimes for bubbles and drops in unhindered gravitational motion through liquids from Clift et al. [17], theoretical value for Reynolds number for reproduced conditions of bubble 26 without solid wall.

Finally, horizontal velocity in PLANE 1 was analysed to explore the effect of the wall. Although the graphic results do not offer a clear positive tendency (Figure 4.16), the numerical values performed again an average positive constant horizontal velocity.

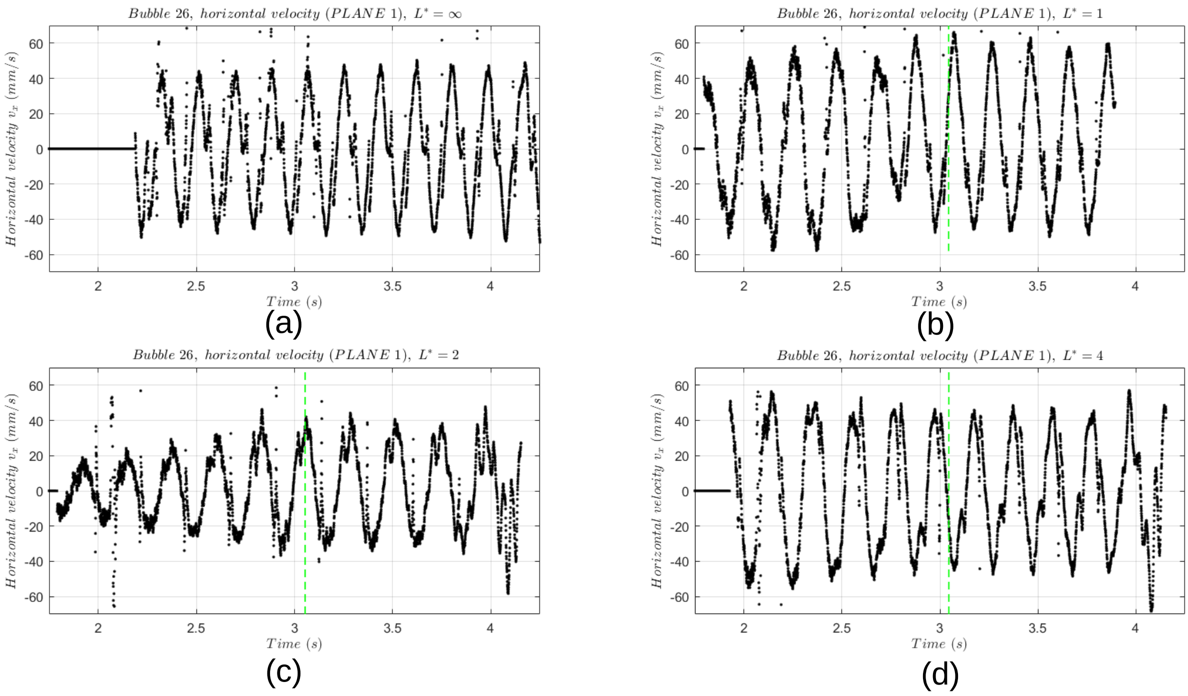

Figure 4.16: Horizontal wall-normal velocity for bubbles in the spiralling regime at different values of L^* (infinity or no wall, 1, 2 and 4, left to right and top to bottom).

Even though the previous picture may show a small impact on the migration velocity due to the wall, Figure 4.17 provides near-zero values for acceleration, hence a permanent migration pace.

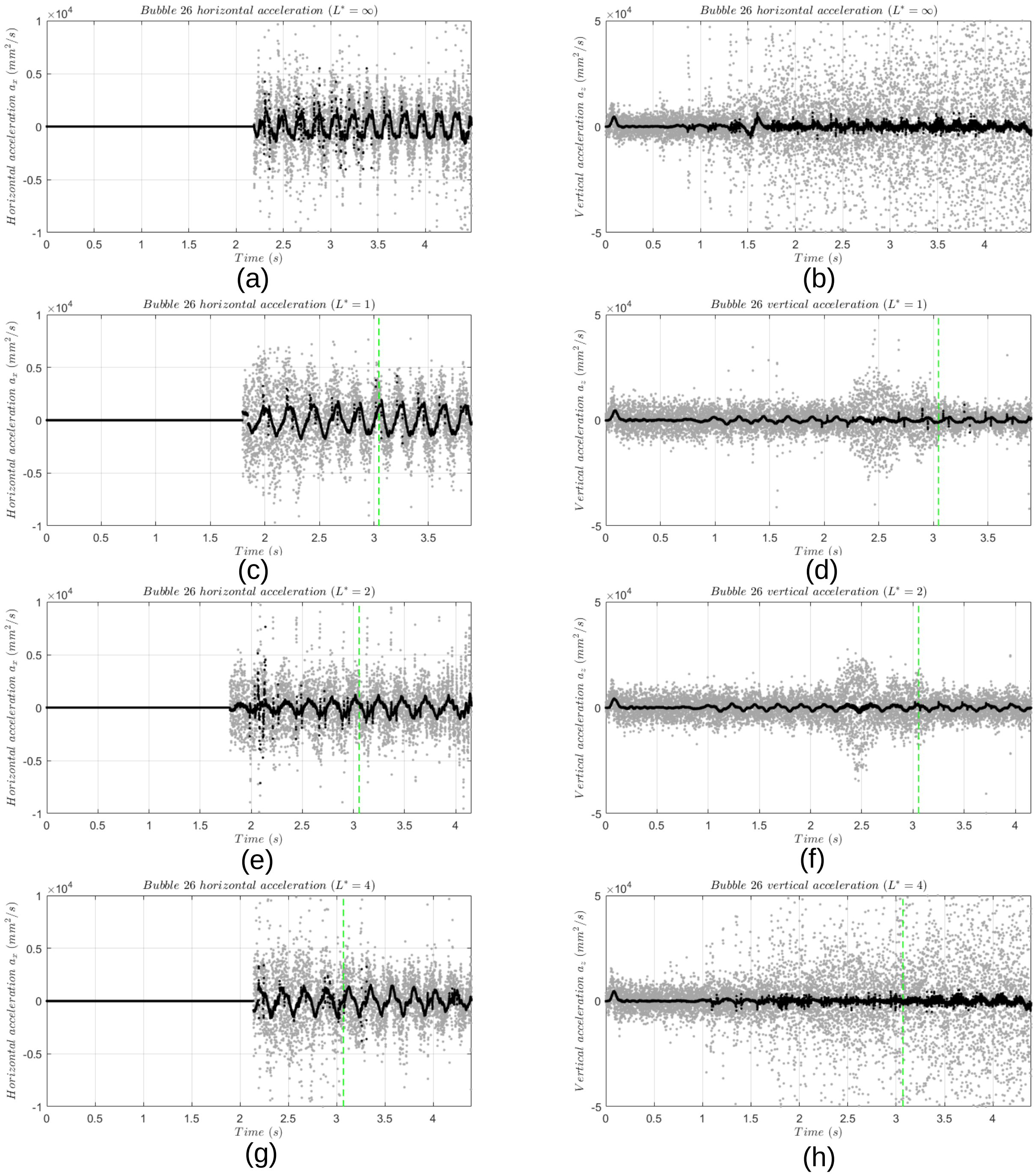

Figure 4.17: Horizontal (top row) and vertical (bottom row) bubble acceleration for experiments in the spiralling regime (case II, bubble 26) for different values of L^*: infinity or no wall (a, b), 1 (c, d), 2 (e, f) and 4 (g, h).

4.3. Case III: planar zigzagging regime

Finally, we performed experiments directed to find a bubble freely rising while performing a planar zigzag trajectory. For this purpose, we replicated reference case 19 in Cano-Lozano et al. [18], what involved the so-called T05 silicon oil and an injector diameter of approximately 2 mm (see Table 3.3). The capillary length of this fluid is 1.48 mm, indicating a maximum inlet diameter of 2.95 mm, which is larger than target so the experiment is theoretically feasible. However, it was not possible to perform these experiments properly. The inlet size was so close to the capillary limit that, after the formation of a few stable bubbles, the liquid started to drain into the air line, inhibiting the possibility to record these trajectories.

In some occasions, more bubbles were able to be formed, what allowed us to perform some recordings, but the instability of the process difficulted cameras and motor control, as the bubbling process never reached complete stability and progressively slowed down every time until hitting the surface tension limit.

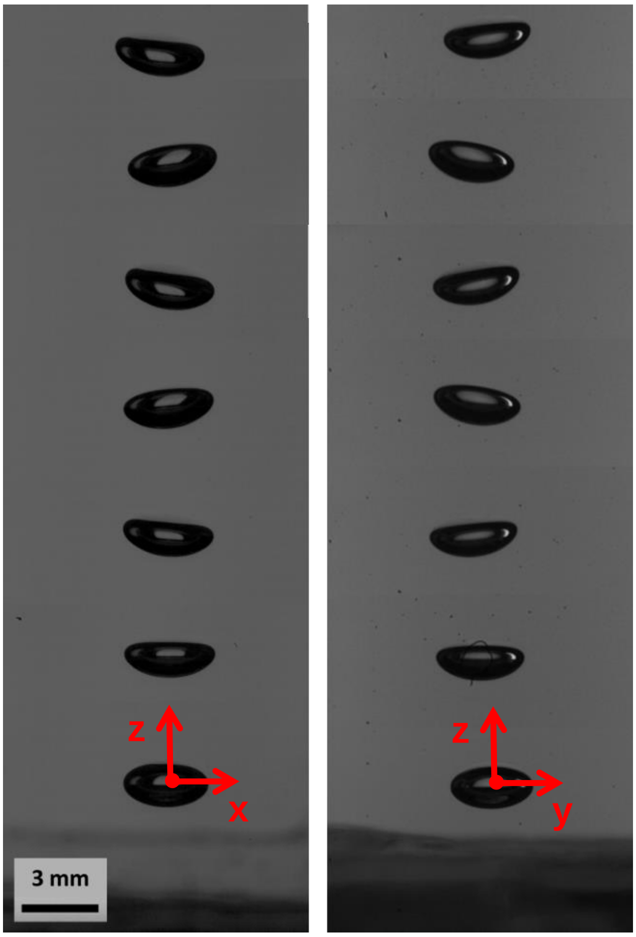

(a) (b)

Figure 4.18: Case III, planar zigzagging regime, reproduction of bubble 19 from the reference paper [18]. Recordings of (a) PLANE 1 (xz, perpendicular to wall) and (b) PLANE 2 (yz, parallel to wall).

Based on these few recordings, we performed a qualitative analysis that indicated that the bubble followed the desired planar zigzagging path. Nevertheless, this zigzagging plane was usually neither of the recorded ones, in other words, the bubble's horizontal displacement happened in a different random plane every time. We could not acknowledge this condition with the information extracted from the high-speed videos, as displacement could be observed in both planes, but we confirmed it by performing a top-view recording. In future works, the characterization of this zigzagging plane will be of immense interest, as its relative position with the vertical surface will definitely affect its influence. The possibility to control the zigzagging plane or to easily twist the wall perpendicularly to it could be of great use too, as it would enable for an easier comparison to numerical simulations (where the wall is usually perpendicular to the zigzagging plane, like such from [25] and those performed by the group).

5. CONCLUSION AND FUTURE WORK

The present work involved different cases of bubbles rising in a still liquid in the proximity of a vertical solid surface. These cases were experimentally tested, recorded and post-processed, extracting information about the followed paths and trajectories and characterizing their movement using several dimensionless parameters.

The experiments required a highly sophisticated experimental facility which was designed *ad hoc* in order to fulfil all the experiment necessities, such as a tank tall enough for the bubbles' paths to develop, a camera driving mechanism or a coverage to avoid liquid soiling. The experiments covered three different air nozzles (of several types and sizes) and three distinct values for wall – bubble distance, what enabled us to observe the three main regimes described in the reference case [18].

The case involving a planar zigzagging bubble could not be studied deeply due to operative reasons, but a broad analysis was performed around rectilinear and spiralling bubbles. Both cases performed the expected behaviour when no wall was introduced, deviating from the initial path when it was close enough. It was observed that the closer the wall was placed, the further the bubbles migrated away from the wall.

In the near future, several aspects that this work could not cover are expected to be improved. For instance, different techniques will be tested in order to achieve stability in the bubbling process of the zigzagging case, such as air injection via a syringe pump or changing the fluid with a water-based mixture in order to use a superhydrophobic substrate (similarly to what was implemented in the spiralling case). Recent findings regarding chemical oleophobic substrates based on nanocomposites have been reported by Ma et al. [42], opening the possibility to create large bubbles from small nozzles (just like what happened using hydrophobic substances) but without the need to use a polar water-based fluid, but the original non-polar silicon oil, which is much more effective in repelling surfactants and would provide more ideal laboratory conditions [11].

Furthermore, different bubble diameters could be tested in the three regimes in order to cover other regions of the Ga-Bo plane, what would help determine the relevance of bubble size in the problem and how the wall affects the transition between regimes. This will facilitate the comparison to numerical simulations, such as those by Zhang et al. [25] or the ones performed by the group, which involve exactly the same cases as the reported in this work. With the combination of this work and the simulations performed by the group, we expect to completely characterize the problem of a bubble rising in the proximity of a wall by the determination of the effects involved in bubbles' dynamics, hence in lift and drag forces [11] – [27].

This work will be extended as a PhD thesis which will regard further aspects in the field of multiphase flows. Firstly, after characterizing the bubble's behaviour under the effect of a solid surface, it will be of great significance to confine the bubbles between two walls, observing how this condition may stabilize or destabilize its movement and how it may affect bubble's dynamics. This study will be extended to a confined bubble swarm, where interaction between bubbles and phenomena of coalescence are predominant.

Secondly, the influence of surface elasticity will be analysed, with the focus on possible applications concerning biological flows. Elastic membranes of known elastic modulus will be used as solid wall and pulsating motion will be applied to them, thus perturbating the bubble movement.

Finally, one last interesting configuration is the study of the bubble motion inside non-uniform streams characterized by shear. In this sense, the direction and magnitude of the lift force around the bubble is essential. However, only few works exist regarding this topic due to the complex nature of these kind of experiments and the absence of precise numerical models until recent times. For this reason, our work will have the aim to describe bubble motion under shear flow under wide ranges of flow conditions.

REFERENCES

[1] J. Rodríguez-Rodríguez, A. Sevilla, C. Martínez-Bazán, and J. M. Gordillo, "Generation of Microbubbles with Applications to Industry and Medicine," *Annu. Rev. Fluid Mech.*, vol. 47, no. 1, pp. 405–429, Jan. 2015, doi: 10.1146/annurev-fluid-010814-014658.

[2] R. Bolaños Jimenez, "Dynamics of bubble formation in cylindrical and planar geometries," Universidad de Jaén, Jaén, 2011.

[3] R. Hernández-Martínez, S. Valdivia-Rivera, J. Betto-Sagahon, A. Coreño-Alonso, O. Tzintzun-Camacho, and M. A. Lizardi-Jiménez, "Solubilization and removal of petroleum hydrocarbons by a native microbial biomass in a bubble column reactor," *Rev. Mex. Ing. Química*, vol. 18, no. 1, pp. 181–189, Jan. 2019, doi: 10.24275/UAM/IZT/DCBI/REVMEXINGQUIM/2019V18N1/HERNANDEZ.

[4] X. Frank, N. Dietrich, J. Wu, R. Barraud, and H. Z. Li, "Bubble nucleation and growth in fluids," *Chem. Eng. Sci.*, vol. 62, no. 24, pp. 7090–7097, Dec. 2007, doi: 10.1016/J.CES.2007.08.030.

[5] J. B. Zhang, J. Wu, S. Poncin, M. Hamelin, and H. Z. Li, "Microscale Investigation of Anaerobic Biogas Production under Various Hydrodynamic Conditions," *Environ. Sci. Technol.*, vol. 46, no. 16, pp. 8698–8704, Aug. 2012, doi: 10.1021/ES3013722.

[6] Y. Matsumoto, J. S. Allen, S. Yoshizawa, T. Ikeda, and Y. Kaneko, "Medical ultrasound with microbubbles," *Exp. Therm. Fluid Sci.*, vol. 29, no. 3, pp. 255–265, Mar. 2005, doi: 10.1016/J.EXPTHERMFLUSCI.2004.05.008.

[7] S. A. Bhattacharya, A. Paul, S. Bhattacharya, B. G. Prajapati, and A. A. Paul, "A Conceptual Review on Micro Bubbles Dual Functional Cationic Solid Lipid Nano Particles Of Anticancer Drug View project Development of bioadhesive topical formulations View project A Conceptual Review on Micro Bubbles," 2017, Accessed: Aug. 13, 2021. [Online]. Available: http://biomedres.us/submit-manuscript.php.

[8] D. B. R. Kenning and V. H. Del Valle M, "Fully-developed nucleate boiling: Overlap of areas of influence and interference between bubble sites," *Int. J. Heat Mass Transf.*, vol. 24, no. 6, pp. 1025–1032, Jun. 1981, doi:

10.1016/0017-9310(81)90133-2.

[9] D. M. Mueth, G. F. Debregeas, G. S. Karczmar, P. J. Eng, S. R. Nagel, and H. M. Jaeger, “Signatures of granular microstructure in dense shear flows,” *Nat. 2000 4066794*, vol. 406, no. 6794, pp. 385–389, Jul. 2000, doi: 10.1038/35019032.

[10] H. Chanson, *Air Bubble Entrainment in Free-Surface Turbulent Shear Flows*. Bath: Academic Press, 1996.

[11] J. Magnaudet and I. Eames, “The Motion of High-Reynolds-Number Bubbles in Inhomogeneus Flows,” *Annu. Rev. Fluid Mech.*, vol. 32, pp. 659–708, 2000.

[12] C. Estepa-Cantero, “Experimental study of the influence of a vertical wall on a rising bubble,” Universidad de Jaén, 2019.

[13] J. C. Cano-Lozano, P. Bohorquez, and C. Martínez-Bazán, “Wake instability of a fixed axisymmetric bubble of realistic shape,” *Int. J. Multiph. Flow*, vol. 51, pp. 11–21, 2013, doi: 10.1016/j.ijmultiphaseflow.2012.11.005.

[14] H. N. Oğuz and A. Prosperetti, “Dynamics of bubble growth and detachment from a needle,” *J. Fluid Mech.*, vol. 257, pp. 111–145, 1993, doi: 10.1017/S0022112093003015.

[15] W. Fritz, “Berechnung des Maximalvolumes von Dampfblasen,” *Phys. Zeitschr*, vol. 36, pp. 379–384, 1935, [Online]. Available: https://ci.nii.ac.jp/naid/10015401785.

[16] M. Rubio-Rubio, R. Bolaños-Jiménez, C. Martínez-Bazán, J. C. Muñoz-Hervás, and A. Sevilla, “Superhydrophobic substrates allow the generation of giant quasi-static bubbles,” *J. Fluid Mech.*, vol. 912, pp. 1–14, 2021, doi: 10.1017/jfm.2020.1098.

[17] R. Clift, J. R. Grace, and M. E. Weber, *Bubbles, Drops, and Particles*. 1978.

[18] J. C. Cano-Lozano, C. Martínez-Bazán, J. Magnaudet, and J. Tchoufag, “Paths and wakes of deformable nearly spheroidal rising bubbles close to the transition to path instability,” *Phys. Rev. Fluids*, vol. 1, no. 5, pp. 1–30, 2016, doi: 10.1103/PhysRevFluids.1.053604.

[19] P. G. Saffman, “On the rise of small air bubbles in water,” *J. Fluid Mech.*, vol. 1, no. 3, pp. 249–275, 1956, doi: 10.1017/S0022112056000159.

[20] B. Yang, A. Prosperetti, and S. Takagi, “The transient rise of a bubble subject to shape or volume changes,” *Phys. Fluids*, vol. 15, no. 9, pp. 2640–2648, 2003, doi: 10.1063/1.1592800.

[21] D. Bhaga and M. E. Weber, “Bubbles in viscous liquids: shapes, wakes and velocities,” *J. Fluid Mech.*, vol. 105, pp. 61–85, 1981, doi: 10.1017/S002211208100311X.

[22] J. Lee and H. Park, “Wake structures behind an oscillating bubble rising close to a vertical wall,” *Int. J. Multiph. Flow*, vol. 91, pp. 225–242, 2017, doi: 10.1016/j.ijmultiphaseflow.2017.02.004.

[23] H. Jeong and H. Park, “Near-wall rising behaviour of a deformable bubble at high Reynolds number,” *J. Fluid Mech.*, vol. 771, pp. 564–594, 2015, doi: 10.1017/jfm.2015.191.

[24] A. W. G. De Vries, A. Biesheuvel, and L. Van Wijngaarden, “Notes on the path and wake of a gas bubble rising in pure water,” *Int. J. Multiph. Flow*, vol. 28, no. 11, pp. 1823–1835, 2003, doi: 10.1016/S0301-9322(02)00036-8.

[25] Y. Zhang, S. Dabiri, K. Chen, and Y. You, “An initially spherical bubble rising near a vertical wall,” *Int. J. Heat Fluid Flow*, vol. 85, p. 108649, Oct. 2020, doi: 10.1016/J.IJHEATFLUIDFLOW.2020.108649.

[26] P. Shi, R. Rzehak, D. Lucas, and J. Magnaudet, “Hydrodynamic forces on a clean spherical bubble translating in a wall-bounded linear shear flow,” *Phys. Rev. Fluids*, vol. 5, no. 7, pp. 1–38, 2020, doi: 10.1103/PhysRevFluids.5.073601.

[27] W. L. Shew, S. Poncet, and J.-F. Pinton, “Force measurements on rising bubbles,” *J. Fluid Mech.*, vol. 569, pp. 51–60, Dec. 2006, doi: 10.1017/S0022112006002928.

[28] Y. Fu and Y. Liu, “Experimental study of bubbly flow using image processing techniques,” *Nucl. Eng. Des.*, vol. 310, pp. 570–579, 2016, doi: 10.1016/j.nucengdes.2016.10.044.

[29] C. Bongiovanni, A. Dominguez, and J. P. Chevaillier, “Understanding images of bubbles,” *Eur. J. Phys.*, vol. 21, no. 6, pp. 561–570, 2000, doi: 10.1088/0143-0807/21/6/307.

[30] Nobuyuki Otsu, “A Threshold Selection Method from Gray-Level Histograms,” *IEEE Trans. Syst. Man Cybern*, vol. 9, no. 1, pp. 62–66, 1979.

[31] D. Bradley and G. Roth, “Adaptive Thresholding using the Integral Image,” *J. Graph. Tools*, vol. 12, no. 2, pp. 13–21, Jan. 2011, doi: 10.1080/2151237X.2007.10129236.

[32] P. D. Wellner, “Adaptive Thresholding for the DigitalDesk,” 1993. doi: 10.1.1.709.2632.

[33] R. Zenit and J. Magnaudet, “Path instability of rising spheroidal air bubbles: A shape-controlled process,” *Phys. Fluids*, vol. 20, no. 6, 2008, doi: 10.1063/1.2940368.

[34] Y. Tagawa, S. Takagi, and Y. Matsumoto, “Surfactant effect on path instability of a rising bubble,” *J. Fluid Mech*, vol. 738, p. 124, 2014, doi: 10.1017/jfm.2013.571.

[35] C. S. Miner and N. N. Dalton, “Physical Properties of Glycerine and Its Solutions,” *J. Am. Pharm. Assoc. (Scientific ed.)*, vol. 42, no. 5, p. 326, May 1953, doi: 10.1002/JPS.3030420524.

[36] K. Takamura, H. Fischer, and N. R. Morrow, “Physical properties of aqueous glycerol solutions,” *J. Pet. Sci. Eng.*, vol. 98–99, pp. 50–60, Nov. 2012, doi: 10.1016/j.petrol.2012.09.003.

[37] Productos Químicos Monterrey, “Hoja de datos de seguridad para sustancias químicas,” 1998. [Online]. Available: http://iio.ens.uabc.mx/hojas-seguridad/cloruro-de-sodio.pdf.

[38] T. Tate Esq., “XXX. On the magnitude of a drop of liquid formed under different circumstances,” *London, Edinburgh, Dublin Philos. Mag. J. Sci.*, vol. 27, no. 181, pp. 176–180, Mar. 1864, doi: 10.1080/14786446408643645.

[39] S. di Bari and A. J. Robinson, “Experimental study of gas injected bubble growth from submerged orifices,” *Exp. Therm. Fluid Sci.*, vol. 44, pp. 124–137, Jan. 2013.

[40] SMC Corporation, “AC Servo Motor Driver LECSA Series Operation Manual.” pp. 1–419, 2018.

[41] J. B. Will, V. Mathai, S. G. Huisman, D. Lohse, C. Sun, and D. Krug,

"Kinematics and dynamics of freely rising spheroids at high Reynolds numbers," *J. Fluid Mech.*, vol. 912, pp. 1–46, 2021, doi: 10.1017/jfm.2020.1104.

[42] T. Ma, J. Ma, C. Yang, J. Zhang, and J. Cheng, "Robust, Multiresponsive, Superhydrophobic, and Oleophobic Nanocomposites via a Highly Efficient Multifluorination Strategy," *ACS Appl. Mater. Interfaces*, vol. 13, no. 24, pp. 28949–28961, 2021, doi: 10.1021/acsami.1c07048.

APPENDIX A: MELSOFT MR Configurator 2 code example for motor movement

```
SPN(1465)
STA(50)
STB(150)
SYNC(1)
MOVI(35000)
SPN(1350)
MOVIA(35000)
STB(500)
SPN(1300)
MOVIA(30000)
TIM(4000)
SPN(500)
MOVI(-100000)
STOP
```

APPENDIX B: MATLAB® codes for image data processing

B.1. Main code for trajectories and volumes determination

B.1.1. Function for fluid selection

```
function [f,rho,mu,sigma,x] = seleccion_fluido
    fl = menu('SELECTION OF FLUID', 'Silicon oil
(T11)','Silicon oil (T05)', 'Glycerol - Water mixture');
    switch fl
        case 1
            f='T11';
            rho = 0.935*1000; % kg/m^3
            mu = 0.00935; % Pa/s
            sigma = 20.1e-3; % N/m
            x = 100; %
        case 2
            f='T05';
            rho = 0.913*1000; % kg/m^3
            mu = 0.004565; % Pa/s
            sigma = 19.7e-3; % N/m
            x = 100; %
        case 3
            f='GLYCEROL-WATER';
            [x,rho,sigma,mu]=glyc_water_prop;
    end
end
```

B.1.1.1. Function for water-glycerol mixtures properties calculation

```
function [x,rho,sigma,mu]=glyc_water_prop
    clear
    clc
    g = 9.81;
    datos;
    [model_rho, ~] = FIT_rho_3D(x_rho, T_rho, rho_tabla);
    [model_mu, ~] = FIT_mu_3D(x_mu, T_mu, mu_tabla);
    [fitresult, ~] = sigma_fit(sigma_data);
    incog = menu('MAIN FLUID UNKNOWN', 'Composition', 'Fluid
properties','None');
    switch incog
        case 1
            t = input('Enter temperature of the fluid
mixture(°C): '); %°C
            T = t+273.15;
            d_tob = menu('BUBBLE SIZE','small (24)','medium
(25)','large (26)');
            Mo = 9.9*1e-6;
            switch d_tob
                case 1
                    Bo = 7;
```

```
                Ga = 76.72;
            case 2
                Bo = 8.5;
                Ga = 88.74;
            case 3
                Bo = 10;
                Ga = 100.25;
        end
        x=0.01;
        sigue=1;
        while sigue
            rho = model_rho(x,T);
            mu = model_mu(x,T);
            sigma=feval(fitresult,T);
            sigma_Mo = (g*(mu^4)/Mo/rho)^(1/3);

            if abs(sigma - sigma_Mo)<=1e-3
                d1=((Bo*sigma/g/rho)^0.5); % m
                d2=(((Ga*mu/rho)^2)/g)^(1/3); % m
                err = abs(d1-d2)/d1*100;
                if abs(d1-d2)<=1e-6
                    sigue=0;
                    clc
                    dm=(d1+d2)/2; % m
                    d_orif=(dm^3)*rho*g/6/sigma*1e3; % mm
                    fprintf('Concentration = %2g%%
weigth\nDiameter of orifice = %2g mm\nError =
%2g%%\n',x,d_orif,err);
                else
                    if x<100
                        x=x+0.001;
                    else
                        disp('ERROR: no values found for
diameter');
                        sigue=0;
                    end
                end
            else
                if x<100
                    x=x+0.01;
                else
                    disp('ERROR: no values found for
surface tension');
                    sigue=0;
                end
            end
        end
    case 2
        t = input('Enter temperature of the fluid
mixture(°C): '); %°C
        T = t+273.15;
```

```
            x = 72.5; %depends on mixture composition!
            rho = model_rho(x,T);
            mu = model_mu(x,T);
            sigma=feval(fitresult,T);
        case 3
            x=[];rho=[];sigma=[];mu=[];
    end
end
```

B.1.1.2. Function for iterpolation of viscosity data (theorical)

```
function [fitresult, gof] = FIT_mu_3D(x_mu, T_mu, mu_tabla)
%% Fit: 'mu_3D'.
[xData, yData, zData] = prepareSurfaceData( x_mu, T_mu,
mu_tabla );

% Set up fittype and options.
ft = 'cubicinterp';

% Fit model to data.
[fitresult, gof] = fit( [xData, yData], zData, ft ,
'Normalize', 'on');
```

B.1.1.3. Function for interpolation of density data (theorical)

```
function [fitresult, gof] = FIT_rho_3D(x_rho, T_rho,
rho_tabla)
%% Fit: 'rho_3D'.
[xData, yData, zData] = prepareSurfaceData( x_rho, T_rho,
rho_tabla );

% Set up fittype and options.
ft = fittype( 'poly33');

% Fit model to data.
[fitresult, gof] = fit( [xData, yData], zData, ft,
'Normalize', 'on' );
```

B.1.1.4. Function for interpolation of surface tension data (empirical)

```
function [fitresult, gof] = sigma_fit(sigma_data)
%% Fit: 'sigma_fit'.
T=sigma_data(:,2);
s=sigma_data(:,3)/1000;
[xData, yData] = prepareCurveData( T, s );

% Set up fittype and options.
ft = fittype( 'smoothingspline' );
opts = fitoptions( 'Method', 'SmoothingSpline' );
opts.Normalize = 'on';
opts.SmoothingParam = 0.984490460570475;
```

```
% Fit model to data.
[fitresult, gof] = fit( xData, yData, ft, opts );

% Plot fit with data.
subplot( 2, 1, 1 );
h = plot( fitresult, xData, yData);
title('$$Surface~tension~measurements$$','Interpreter','latex'
);
legend( h, '\(\sigma\)~vs~T', 'Smoothing~spline~fit',
'Location', 'NorthEast', 'Interpreter', 'latex' );
% Label axes
xlabel( 'Temperature,~T~(K)', 'Interpreter', 'latex' );
ylabel( 'Surface~tension,~\(\sigma\)~(mN/m)', 'Interpreter',
'latex' );
grid on

% Plot residuals.
subplot( 2, 1, 2 );
h = plot( fitresult, xData, yData, 'residuals');
title('$$Surface~tension~measurements$$~residuals',
'Interpreter', 'latex' );
legend( h, 'Smoothing~spline~fit~(residuals)', 'Zero Line',
'Location', 'NorthEast', 'Interpreter', 'latex' );
% Label axes
xlabel( 'Temperature,~T~(K)', 'Interpreter', 'latex' );
ylabel( 'Surface~tension,~\(\sigma\)~(mN/m)', 'Interpreter',
'latex' );
grid on
```

B.1.2. Function for inlet device selection

```
%INLET DATA
function d_tob = seleccion_tobera
    tob = menu('INLET SELECTION', 'small nozzle (19)', 'medium
nozzle (22)', 'large orifice (26)');
    switch tob
        case 1
            d_tob = 2.00;
        case 2
            d_tob = 2.35;
        case 3
            d_tob = 14.60;
    end
end
```

B.1.3. Function for bubble edge detection

```
function [bw,cont,properties] = deteccion_filo(imagen)
    clc
    X=imread(imagen);
    bw = img_binario(X);
```

```
    bw=bwpropfilt(bw,'Solidity', [0.5,1]);
    bw=bwpropfilt(bw, 'MajorAxisLength', [0, 700]);
    bw=bwareafilt(bw,[15000,145000]);
    properties=regionprops(bw,'Area','Centroid');
    [cont,~]=bwboundaries(bw);
end
```

B.1.3.1. Function for image binarization

```
function [BW,maskedImage] = img_binario(X)
% Threshold image - adaptive threshold
BW = imbinarize(X, 'adaptive', 'Sensitivity', 1.00000,
'ForegroundPolarity', 'bright');

% Invert mask
BW = imcomplement(BW);


% Clear borders
BW = imclearborder(BW);

% Fill holes
BW = imfill(BW, 'holes');

% Create masked image.
maskedImage = X;
maskedImage(~BW) = 0;
end
```

B.1.4. Functions for volume calculation

B.1.4.1. Volume of 2D trajectories

```
function vol = calc_vol(cont, esc)
z_max = min(cont{1}(:,1));
x_min = min(cont{1}(:,2));
x_max = max(cont{1}(:,2));
x_centroid = round((x_max+x_min)/2);
cont_izq = 0;
cont_dcha = 0;
izq_x = [];
izq_z = [];
dcha_x = [];
dcha_z = [];
for k=1:length(cont{1}(:,1))
    if (cont{1}(k,2)) <= x_centroid
        cont_izq = cont_izq+1;
        izq_x(cont_izq) = cont{1}(k,2);
        izq_z(cont_izq) = cont{1}(k,1);
    else
        cont_dcha = cont_dcha+1;
```

```
        dcha_x(cont_dcha) = cont{1}(k,2);
        dcha_z(cont_dcha) = cont{1}(k,1);
    end
end
borde_i = [sortrows(izq_x);sortrows(izq_z)];
borde_d = [sortrows(dcha_x);sortrows(dcha_z)];
borde_i(1,:) = abs(borde_i(1,:)-x_centroid)*esc;
borde_d(1,:) = abs(borde_d(1,:)-x_centroid)*esc;
borde_i(2,:) = abs(borde_i(2,:)-z_max)*esc;
borde_d(2,:) = abs(borde_d(2,:)-z_max)*esc;
vol_d = abs(pi*trapz(borde_i(2,:),borde_i(1,:).^2));
vol_i = abs(pi*trapz(borde_d(2,:),borde_d(1,:).^2));
vol = 0.5*(vol_d+vol_i);
end
```

B.1.4.2. Volume of 3D trajectories

```
function [vol,cent3] = calc_vol_3(cont1,cont2, esc)
% cont 1
if size(cont2)>size(cont1)
    cont2 = imresize(cont2,size(cont1));
else
    cont1 = imresize(cont1,size(cont2));
end
z_max1 = min(cont1(:,1));
x_min1 = min(cont1(:,2));
x_max1 = max(cont1(:,2));
x_centroid1 = round((x_max1+x_min1)/2);
cont_izq = 0;
cont_dcha = 0;
izq_x = [];
izq_z = [];
dcha_x = [];
dcha_z = [];
for k=1:length(cont1(:,1))
    if (cont1(k,2)) <= x_centroid1
        cont_izq = cont_izq+1;
        izq_x(cont_izq) = cont1(k,2);
        izq_z(cont_izq) = cont1(k,1);
    else
        cont_dcha = cont_dcha+1;
        dcha_x(cont_dcha) = cont1(k,2);
        dcha_z(cont_dcha) = cont1(k,1);
    end
end
borde_i1 = [sortrows(izq_x);sortrows(izq_z)];
borde_d1 = [sortrows(dcha_x);sortrows(dcha_z)];
borde_i1(1,:) = abs(borde_i1(1,:)-x_centroid1)*esc{1};
borde_d1(1,:) = abs(borde_d1(1,:)-x_centroid1)*esc{1};
borde_i1(2,:) = abs(borde_i1(2,:)-z_max1)*esc{1};
borde_d1(2,:) = abs(borde_d1(2,:)-z_max1)*esc{1};
```

```
vol_d1 = abs(pi*trapz(borde_i1(2,:),borde_i1(1,:).^2));
vol_i1 = abs(pi*trapz(borde_d1(2,:),borde_d1(1,:).^2));
vol1 = 0.5*(vol_d1+vol_i1);
% cont 2
z_max2 = min(cont2(:,1));
x_min2 = min(cont2(:,2));
x_max2 = max(cont2(:,2));
x_centroid2 = round((x_max2+x_min2)/2);
cont_izq = 0;
cont_dcha = 0;
izq_x = [];
izq_z = [];
dcha_x = [];
dcha_z = [];
for k=1:length(cont2(:,1))
    if (cont2(k,2)) <= x_centroid2
        cont_izq = cont_izq+1;
        izq_x(cont_izq) = cont2(k,2);
        izq_z(cont_izq) = cont2(k,1);
    else
        cont_dcha = cont_dcha+1;
        dcha_x(cont_dcha) = cont2(k,2);
        dcha_z(cont_dcha) = cont2(k,1);
    end
end
borde_i2 = [sortrows(izq_x);sortrows(izq_z)];
borde_d2 = [sortrows(dcha_x);sortrows(dcha_z)];
borde_i2(1,:) = abs(borde_i2(1,:)-x_centroid1)*esc{2};
borde_d2(1,:) = abs(borde_d2(1,:)-x_centroid1)*esc{2};
borde_i2(2,:) = abs(borde_i2(2,:)-z_max2)*esc{2};
borde_d2(2,:) = abs(borde_d2(2,:)-z_max2)*esc{2};
%rescaling
sz=[size(borde_d1,2),size(borde_i1,2),size(borde_d2,2),size(bo
rde_i2,2)];
borde_d1=imresize(borde_d1,[2,min(sz)]);
borde_i1=imresize(borde_i1,[2,min(sz)]);
borde_d2=imresize(borde_d2,[2,min(sz)]);
borde_i2=imresize(borde_i2,[2,min(sz)]);
% average
rx=borde_d1(1,:)+borde_i1(1,:);
ry=borde_d2(1,:)+borde_i2(1,:);
vol_i1 = abs(pi*trapz(borde_i1(2,:),rx.*ry));
vol_d1 = abs(pi*trapz(borde_d1(2,:),rx.*ry));
vol_i2 = abs(pi*trapz(borde_i2(2,:),rx.*ry));
vol_d2 = abs(pi*trapz(borde_d2(2,:),rx.*ry));
vol = 0.25*(vol_i1+vol_d1+vol_i2+vol_d2);
end
```

B.1.5. Function for fitting of motor position

```
function [p,y,mu]=motor_pos_fit(motor,time)
```

```
max_t=find(motor(:,1)>=max(time*1000),1);
mot_pos=motor(5:max_t,1:7:8);
t=mot_pos(:,1);
y=mot_pos(:,2);
 [p, gof] = createFit_motor_spline(t, y);
fit=feval(p,t);
figure(1)
title('Spline fit - motor position');
ylabel('Vertical position y (mm)');
xlabel('Time (ms)');
plot(t,y,'.');
hold on
plot(t,fit,'k--');
hold off
```

B.1.5.1. Function for spline fit generation around motor position values

```
function [fitresult, gof] = createFit_motor_spline(time, y)
%% Fit: 'untitled fit 1'.
[xData, yData] = prepareCurveData( time, y );

% Set up fittype and options.
ft = fittype( 'smoothingspline' );

% Fit model to data.
[fitresult, gof] = fit( xData, yData, ft );

% Plot fit with data.
figure( 'Name', 'untitled fit 1' );
h = plot( fitresult, xData, yData );
legend( h, 'y vs. time', 'untitled fit 1', 'Location',
'NorthEast', 'Interpreter', 'none' );
% Label axes
xlabel( 'time', 'Interpreter', 'none' );
ylabel( 'y', 'Interpreter', 'none' );
grid on
```

B.2. Routines for graphs plotting

B.2.1. 2D graphs

```
function
showgraphs(d,cent,velx,vely,accx,accy,time,carp,cam,dist,area,
vol,eps,v_term,h_wall,wall_index,Re)
g = 9.81;
%Trajectory
figure(2)
box on
plot(cent(:,1),cent(:,2),'.k');
title('$$Bubble~trajectory$$','Interpreter','latex');
```

```
xlabel('$$Horizontal~position~x~(mm)$$','Interpreter','latex')
;
ylabel('$$Vertical~position~y~(mm)$$','Interpreter','latex');
axis equal
grid on
savefig([carp,'01_traj_C',num2str(cam),'.fig']);
saveas(gcf,[carp,'01_traj_C',num2str(cam),'.png']);
%Trajectory (dimensionless)
d=d*1000;
figure(3)
box on
X=cent(:,1)./d';Y=cent(:,2)./d';
plot(X,Y,'.k');
title('$$Bubble~trajectory~(dimensionless)$$','Interpreter','l
atex');
xlabel('$$Dimensionless~horizontal~position~X~(x/d)$$','Interp
reter','latex');
ylabel('$$Dimensionless~vertical~position~Y~(y/d)$$','Interpre
ter','latex');
switch dist
    case 'no wall'
        S=20;
    case '1D'
        S=1;
    case '2D'
        S=2;
    case '4D'
        S=4;
    otherwise
        S=input('dist. adim.: ');
end
pared_1=[-S,h_wall/mean(d,'omitnan')];
pared_2=[-S,140];
mark_1=[-S,h_wall/mean(d,'omitnan')];
mark_2=[max(X)+S/5,h_wall/mean(d,'omitnan')];
hold on
if ~strcmp(dist,'no wall')
    if cam==1
       plot([pared_1(1),pared_2(1)],[pared_1(2),pared_2(2)],'-
c', 'Linewidth', 3);
    end
    axis([min(X)-
S/5,max(X)+S/5,h_wall/mean(d,'omitnan'),140]);
    grid on

savefig([carp,'00_zoom_traj_dimensionless_C',num2str(cam),'.fi
g']);

saveas(gcf,[carp,'00_zoom_traj_dimensionless_C',num2str(cam),'
.png']);
end
```

```
axis([min(X)-S/5,max(X)+S/5,0,140]);
hold on
if ~strcmp(dist,'no wall')
    plot([mark_1(1),mark_2(1)],[mark_1(2),mark_2(2)],'--g',
'Linewidth', 1);
end
grid on
savefig([carp,'02_traj_dimensionless_C',num2str(cam),'.fig']);
saveas(gcf,[carp,'02_traj_dimensionless_C',num2str(cam),'.png'
]);
wall_time=time(find(cent(:,2)>h_wall,1));
wall_1=[wall_time,ceil(min(cent(:,1)))-1];
wall_2=[wall_time,ceil(max(cent(:,1)))];
figure(4)
box on
plot(time,cent(:,1),'.k');
title('$$Bubble~trajectory~-
~time~(x~vs~t)$$','Interpreter','latex');
ylabel('$$Horizontal~position~x~(mm)$$','Interpreter','latex')
;
xlabel('$$Time~(s)$$','Interpreter','latex');
grid on
hold on
if ~strcmp(dist,'no wall')
    plot([wall_1(1),wall_2(1)],[wall_1(2),wall_2(2)],'--g',
'Linewidth', 1);
end
savefig([carp,'03_traj_xt_C',num2str(cam),'.fig']);
saveas(gcf,[carp,'03_traj_xt_C',num2str(cam),'.png']);
figure(5)
box on
plot(time,cent(:,2),'.k');
title('$$Bubble~trajectory~-
~time~(y~vs~t)$$','Interpreter','latex');
ylabel('$$Vertical~position~y~(mm)$$','Interpreter','latex');
xlabel('$$Time~(s)$$','Interpreter','latex');
wall_2=[wall_time,ceil(max(cent(:,2)))];
grid on
hold on
if ~strcmp(dist,'no wall')
    plot([wall_1(1),wall_2(1)],[wall_1(2),wall_2(2)],'--g',
'Linewidth', 1);
end
savefig([carp,'04_traj_yt_C',num2str(cam),'.fig']);
saveas(gcf,[carp,'04_traj_yt_C',num2str(cam),'.png']);
%Velocity
figure(6)
box on
plot(time,velx,'.k');
title('$$Bubble~horizontal~velocity$$','Interpreter','latex');
```

```
ylabel('$$Horizontal~velocity~v_x~(mm/s)$$','Interpreter','lat
ex');
xlabel('$$Time~(s)$$','Interpreter','latex');
wall_1=[wall_time,ceil(min(velx))-1];
wall_2=[wall_time,ceil(max(velx))];
grid on
hold on
if ~strcmp(dist,'no wall')
    plot([wall_1(1),wall_2(1)],[wall_1(2),wall_2(2)],'--g',
'Linewidth', 1);
end
axis([0,4.5,-100,100]);
savefig([carp,'05_vel_x_t_C',num2str(cam),'.fig']);
saveas(gcf,[carp,'05_vel_x_t_C',num2str(cam),'.png']);
figure(7)
box on
plot(time,vely,'.k');
title('$$Bubble~vertical~velocity$$','Interpreter','latex');
ylabel('$$Vertical~velocity~v_y~(mm/s)$$','Interpreter','latex
');
xlabel('$$Time~(s)$$','Interpreter','latex');
wall_1=[wall_time,ceil(min(vely))-1];
wall_2=[wall_time,ceil(max(vely))];
grid on
hold on
if ~strcmp(dist,'no wall')
    plot([wall_1(1),wall_2(1)],[wall_1(2),wall_2(2)],'--g',
'Linewidth', 1);
end
hold on
plot([0,max(time)+0.2],[v_term,v_term],'-.r');
axis([0,4.5,0,300]);
text(time(wall_index)-1,v_term-75,['$v_{terminal}$ =
',num2str(v_term),'$ \rightarrow$ Re =
',num2str(mean(Re,'omitnan'))],'Interpreter','Latex','FontSize
',11);
savefig([carp,'06_vel_y_t_C',num2str(cam),'.fig']);
saveas(gcf,[carp,'06_vel_y_t_C',num2str(cam),'.png']);
figure(7)
hold off
box on
plot(time,vely./sqrt(g*d*1000),'.k');
title('$$Bubble~vertical~velocity~(dimensionless,~Re/Ga)$$','I
nterpreter','latex');
ylabel('$$Re/Ga$$','Interpreter','latex');
xlabel('$$Time~(s)$$','Interpreter','latex');
wall_1=[wall_time,ceil(min(vely))-1];
wall_2=[wall_time,ceil(max(vely))];
grid on
hold on
if ~strcmp(dist,'no wall')
```

```
    plot([wall_1(1),wall_2(1)],[wall_1(2),wall_2(2)],'--g',
'Linewidth', 1);
end
savefig([carp,'061_Re-Ga_y_t_C',num2str(cam),'.fig']);
saveas(gcf,[carp,'061_Re-Ga_y_t_C',num2str(cam),'.png']);
figure(7)
hold off
box on
plot(time,Re,'.k');
title('$$Re~vs~time~(bubble~vertical~velocity,~dimensionless)$
$','Interpreter','latex');
ylabel('$$Re$$','Interpreter','latex');
xlabel('$$Time~(s)$$','Interpreter','latex');
wall_1=[wall_time,ceil(min(vely))-1];
wall_2=[wall_time,ceil(max(vely))];
grid on
hold on
if ~strcmp(dist,'no wall')
    plot([wall_1(1),wall_2(1)],[wall_1(2),wall_2(2)],'--g',
'Linewidth', 1);
end
savefig([carp,'062_Re_y_t_C',num2str(cam),'.fig']);
saveas(gcf,[carp,'062_Re_y_t_C',num2str(cam),'.png']);
%Acceleration
figure(8)
box on
plot(time,accx,'.k');
title('$$Bubble~horizontal~acceleration$$','Interpreter','late
x');
ylabel('$$Horizontal~acceleration~a_x~(mm^2/s)$$','Interpreter
','latex');
xlabel('$$Time~(s)$$','Interpreter','latex');
wall_1=[wall_time,ceil(min(accx))-1];
wall_2=[wall_time,ceil(max(accx))];
hold on
if ~strcmp(dist,'no wall')
    plot([wall_1(1),wall_2(1)],[wall_1(2),wall_2(2)],'--g',
'Linewidth', 1);
end
grid on
axis([0,4.5,-10000,10000]);
savefig([carp,'07_acc_x_t_C',num2str(cam),'.fig']);
saveas(gcf,[carp,'07_acc_x_t_C',num2str(cam),'.png']);
figure(9)
box on
plot(time,accy,'.k');
title('$$Bubble~vertical~acceleration$$','Interpreter','latex'
);
ylabel('$$Vertical~acceleration~a_y~(mm^2/s)$$','Interpreter',
'latex');
xlabel('$$Time~(s)$$','Interpreter','latex');
```

```
wall_1=[wall_time,ceil(min(accy))-1];
wall_2=[wall_time,ceil(max(accy))];
hold on
if ~strcmp(dist,'no wall')
    plot([wall_1(1),wall_2(1)],[wall_1(2),wall_2(2)],'--g',
'Linewidth', 1);
end
grid on
axis([0,4.5,-10000,10000]);
savefig([carp,'08_acc_y_t_C',num2str(cam),'.fig']);
saveas(gcf,[carp,'08_acc_y_t_C',num2str(cam),'.png']);
figure(10)
box on
plot(time,vol,'.k');
title('$$Volume~vs~time$$','Interpreter','latex');
ylabel('$$Volume~(mm^3)$$','Interpreter','latex');
xlabel('$$Time~(s)$$','Interpreter','latex');
wall_1=[wall_time,ceil(min(vol))-1];
wall_2=[wall_time,ceil(max(vol))];
hold on
if ~strcmp(dist,'no wall')
    plot([wall_1(1),wall_2(1)],[wall_1(2),wall_2(2)],'--g',
'Linewidth', 1);
end
grid on
savefig([carp,'09_vol_t_C',num2str(cam),'.fig']);
saveas(gcf,[carp,'09_vol_t_C',num2str(cam),'.png']);
figure(11)
box on
plot(time,area,'.k');
title('$$Area~vs~time$$','Interpreter','latex');
ylabel('$$Area~(mm^2)$$','Interpreter','latex');
xlabel('$$Time~(s)$$','Interpreter','latex');
wall_1=[wall_time,ceil(min(area))-1];
wall_2=[wall_time,ceil(max(area))];
grid on
hold on
if ~strcmp(dist,'no wall')
    plot([wall_1(1),wall_2(1)],[wall_1(2),wall_2(2)],'--g',
'Linewidth', 1);
end
savefig([carp,'10_area_t_C',num2str(cam),'.fig']);
saveas(gcf,[carp,'10_area_t_C',num2str(cam),'.png']);
figure(12)
box on
plot(time,eps,'.k');
title('$$Deformation~vs~time$$','Interpreter','latex');
ylabel('$$Epsilon~(\varepsilon)$$','Interpreter','latex');
xlabel('$$Time~(s)$$','Interpreter','latex');
wall_1=[wall_time,0];
wall_2=[wall_time,(max(eps)+0.05)];
```

```
hold on
if ~strcmp(dist,'no wall')
    plot([wall_1(1),wall_2(1)],[wall_1(2),wall_2(2)],'--g',
'Linewidth', 1);
end
grid on
savefig([carp,'11_epsilon_t_C',num2str(cam),'.fig']);
saveas(gcf,[carp,'11_epsilon_t_C',num2str(cam),'.png']);
```

B.2.2. 3D graphs

```
function
showgraphs3D(d,cent,velx,vely,velz,accx,accz,time,carp,cam,dis
t,area,vol,eps,v_term,h_wall,wall_index,Re)
g = 9.81;
hold off
%% Trajectory
figure(1)
[r,~]=size(cent);
if strcmp(dist,'no wall')
    wall_index=r;
end
box on
plot3(cent(1:wall_index,1),cent(1:wall_index,2),cent(1:wall_in
dex,3),'.','Color',[0.65,0.65,0.65]);
hold on
plot3(cent(wall_index:r,1),cent(wall_index:r,2),cent(wall_inde
x:r,3),'.k');
title('$$Bubble~trajectory$$','Interpreter','latex');
xlabel('$$x~(mm)$$','Interpreter','latex');
ylabel('$$y~(mm)$$','Interpreter','latex');
zlabel('$$z~(mm)$$','Interpreter','latex');
xl=xlim;
yl=ylim;
difx=xl(2)-xl(1);
dify=yl(2)-yl(1);
if difx>dify
    ylim([yl(1)-(difx-dify)/2,yl(2)+(difx-dify)/2]);
else
    xlim([xl(1)-(dify-difx)/2,xl(2)+(dify-difx)/2]);
end
zlim([cent(find(cent(:,1)~=0,1),3),inf])
grid on
savefig([carp{1,2},'01_traj_C',num2str(cam),'.fig']);
saveas(gcf,[carp{1,2},'01_traj_C',num2str(cam),'.png']);
%% Trajectory (dimensionless)
d=d*1000;
figure(2)
box on
X=cent(:,1)./d';Y=cent(:,2)./d';Z=cent(:,3)./d';
```

```
plot3(X(1:wall_index),Y(1:wall_index),Z(1:wall_index),'.','Col
or',[0.65,0.65,0.65]);
hold on
plot3(X(wall_index:r),Y(wall_index:r),Z(wall_index:r),'.k');
title('$$Bubble~trajectory~(dimensionless)$$','Interpreter','l
atex');
xlabel('$$X~(x/d)$$','Interpreter','latex');
ylabel('$$Y~(y/d)$$','Interpreter','latex');
zlabel('$$Z~(z/d)$$','Interpreter','latex');
hold on
xl=xlim;
yl=ylim;
difx=xl(2)-xl(1);
dify=yl(2)-yl(1);
if difx>dify
    ylim([yl(1)-(difx-dify)/2,yl(2)+(difx-dify)/2]);
else
    xlim([xl(1)-(dify-difx)/2,xl(2)+(dify-difx)/2]);
end
zlim([Z(find(cent(:,1)~=0,1)),inf])
grid on
savefig([carp{1,2},'02_traj_dimensionless_C',num2str(cam),'.fi
g']);
saveas(gcf,[carp{1,2},'02_traj_dimensionless_C',num2str(cam),'
.png']);
%% Traj-time-horizontal from wall
wall_time=time(find(cent(:,3)>h_wall,1));
wall_1=[wall_time,ceil(min(cent(:,1)))-1];
wall_2=[wall_time,ceil(max(cent(:,1)))];
figure(3)
box on
plot(time,cent(:,1),'.k');
title('$$Bubble~trajectory~-
~time~(x~vs~t)$$','Interpreter','latex');
ylabel('$$x~(mm)$$','Interpreter','latex');
xlabel('$$Time~(s)$$','Interpreter','latex');
grid on
hold on
if ~strcmp(dist,'no wall')
    plot([wall_1(1),wall_2(1)],[wall_1(2),wall_2(2)],'--g',
'Linewidth', 1);
end
savefig([carp{1,2},'03_traj_xt_C',num2str(cam),'.fig']);
saveas(gcf,[carp{1,2},'03_traj_xt_C',num2str(cam),'.png']);
%% Traj-time-vertical
figure(4)
box on
plot(time,cent(:,3),'.k');
title('$$Bubble~trajectory~-
~time~(z~vs~t)$$','Interpreter','latex');
ylabel('$$z~(mm)$$','Interpreter','latex');
```

```
xlabel('$$Time~(s)$$','Interpreter','latex');
wall_2=[wall_time,ceil(max(cent(:,3)))];
grid on
hold on
if ~strcmp(dist,'no wall')
    plot([wall_1(1),wall_2(1)],[wall_1(2),wall_2(2)],'--g',
'Linewidth', 1);
end
savefig([carp{1,2},'04_traj_zt_C',num2str(cam),'.fig']);
saveas(gcf,[carp{1,2},'04_traj_zt_C',num2str(cam),'.png']);
%% Velocity-horizontal from wall
figure(5)
box on
plot(time,velx,'.k');
title('$$Bubble~horizontal~velocity$$','Interpreter','latex');
ylabel('$$Horizontal~velocity~v_x~(mm/s)$$','Interpreter','lat
ex');
xlabel('$$Time~(s)$$','Interpreter','latex');
wall_1=[wall_time,ceil(min(velx))-1];
wall_2=[wall_time,ceil(max(velx))];
grid on
hold on
if ~strcmp(dist,'no wall')
    plot([wall_1(1),wall_2(1)],[wall_1(2),wall_2(2)],'--g',
'Linewidth', 1);
end
axis([0,inf,-150,150]);
savefig([carp{1,2},'05_vel_x_t_C',num2str(cam),'.fig']);
saveas(gcf,[carp{1,2},'05_vel_x_t_C',num2str(cam),'.png']);
%% Velocity-horizontal parallel to wall
figure(6)
box on
plot(time,vely,'.k');
title('$$Bubble~horizontal~velocity$$','Interpreter','latex');
ylabel('$$Horizontal~velocity~v_y~(mm/s)$$','Interpreter','lat
ex');
xlabel('$$Time~(s)$$','Interpreter','latex');
wall_1=[wall_time,ceil(min(vely))-1];
wall_2=[wall_time,ceil(max(vely))];
grid on
hold on
if ~strcmp(dist,'no wall')
    plot([wall_1(1),wall_2(1)],[wall_1(2),wall_2(2)],'--g',
'Linewidth', 1);
end
savefig([carp{1,2},'06_vel_y_t_C',num2str(cam),'.fig']);
saveas(gcf,[carp{1,2},'06_vel_y_t_C',num2str(cam),'.png']);
%%
figure(7)
box on
plot(time,velz,'.k');
```

```
title('$$Bubble~vertical~velocity$$','Interpreter','latex');
ylabel('$$Vertical~velocity~v_z~(mm/s)$$','Interpreter','latex
');
xlabel('$$Time~(s)$$','Interpreter','latex');
wall_1=[wall_time,ceil(min(velz))-1];
wall_2=[wall_time,ceil(max(velz))];
grid on
hold on
if ~strcmp(dist,'no wall')
    plot([wall_1(1),wall_2(1)],[wall_1(2),wall_2(2)],'--g',
'Linewidth', 1);
end
hold on
plot([0,max(time)+0.2],[v_term,v_term],'-.r');
axis([0,inf,0,inf]);
text(time(wall_index)-1,v_term-75,['$v_{terminal}$ =
',num2str(v_term),'$ \rightarrow$ Re =
',num2str(mean(Re,'omitnan'))],'Interpreter','Latex','FontSize
',11);
savefig([carp{1,2},'07_vel_z_t_C',num2str(cam),'.fig']);
saveas(gcf,[carp{1,2},'07_vel_z_t_C',num2str(cam),'.png']);
figure(7)
hold off
box on
plot(time,velz./sqrt(g*d*1000),'.k');
title('$$Bubble~vertical~velocity~(dimensionless,~Re/Ga)$$','I
nterpreter','latex');
ylabel('$$Re/Ga$$','Interpreter','latex');
xlabel('$$Time~(s)$$','Interpreter','latex');
wall_1=[wall_time,ceil(min(velz))-1];
wall_2=[wall_time,ceil(max(velz))];
grid on
hold on
if ~strcmp(dist,'no wall')
    plot([wall_1(1),wall_2(1)],[wall_1(2),wall_2(2)],'--g',
'Linewidth', 1);
end
axis([0,inf,0,1.5]);
savefig([carp{1,2},'071_Re-Ga_z_t_C',num2str(cam),'.fig']);
saveas(gcf,[carp{1,2},'071_Re-Ga_z_t_C',num2str(cam),'.png']);
figure(7)
hold off
box on
plot(time,Re,'.k');
title('$$Re~vs~time~(bubble~vertical~velocity,~dimensionless)$
$','Interpreter','latex');
ylabel('$$Re$$','Interpreter','latex');
xlabel('$$Time~(s)$$','Interpreter','latex');
wall_1=[wall_time,ceil(min(velz))-1];
wall_2=[wall_time,ceil(max(velz))];
grid on
```

```
hold on
if ~strcmp(dist,'no wall')
    plot([wall_1(1),wall_2(1)],[wall_1(2),wall_2(2)],'--g',
'Linewidth', 1);
end
axis([0,inf,0,175])
savefig([carp{1,2},'072_Re_y_t_C',num2str(cam),'.fig']);
saveas(gcf,[carp{1,2},'072_Re_y_t_C',num2str(cam),'.png']);
%% Acceleration-horizontal from wall
figure(8)
box on
plot(time,accx,'.k');
title('$$Bubble~horizontal~acceleration$$','Interpreter','late
x');
ylabel('$$Horizontal~acceleration~a_x~(mm^2/s)$$','Interpreter
','latex');
xlabel('$$Time~(s)$$','Interpreter','latex');
wall_1=[wall_time,ceil(min(accx))-1];
wall_2=[wall_time,ceil(max(accx))];
hold on
if ~strcmp(dist,'no wall')
    plot([wall_1(1),wall_2(1)],[wall_1(2),wall_2(2)],'--g',
'Linewidth', 1);
end
grid on
axis([0,inf,-10000,10000]);
savefig([carp{1,2},'08_acc_x_t_C',num2str(cam),'.fig']);
saveas(gcf,[carp{1,2},'08_acc_x_t_C',num2str(cam),'.png']);
% close all

figure(9)
box on
plot(time,accz,'.k');
title('$$Bubble~vertical~acceleration$$','Interpreter','latex'
);
ylabel('$$Vertical~acceleration~a_z~(mm^2/s)$$','Interpreter',
'latex');
xlabel('$$Time~(s)$$','Interpreter','latex');
wall_1=[wall_time,ceil(min(accz))-1];
wall_2=[wall_time,ceil(max(accz))];
hold on
if ~strcmp(dist,'no wall')
    plot([wall_1(1),wall_2(1)],[wall_1(2),wall_2(2)],'--g',
'Linewidth', 1);
end
grid on
axis([0,inf,-50000,50000]);
savefig([carp{1,2},'09_acc_z_t_C',num2str(cam),'.fig']);
saveas(gcf,[carp{1,2},'09_acc_z_t_C',num2str(cam),'.png']);
%% Shape and volume
figure(10)
```

```
box on
plot(time,vol,'.k');
title('$$Volume~vs~time$$','Interpreter','latex');
ylabel('$$Volume~(mm^3)$$','Interpreter','latex');
xlabel('$$Time~(s)$$','Interpreter','latex');
wall_1=[wall_time,ceil(min(vol))-1];
wall_2=[wall_time,ceil(max(vol))];
hold on
if ~strcmp(dist,'no wall')
    plot([wall_1(1),wall_2(1)],[wall_1(2),wall_2(2)],'--g',
'Linewidth', 1);
end
grid on
savefig([carp{1,2},'10_vol_t_C',num2str(cam),'.fig']);
saveas(gcf,[carp{1,2},'10_vol_t_C',num2str(cam),'.png']);

figure(11)
box on
plot(time,area(:,1),'.k');
title('$$Area1~vs~time$$','Interpreter','latex');
ylabel('$$Area~(mm^2)$$','Interpreter','latex');
xlabel('$$Time~(s)$$','Interpreter','latex');
wall_1=[wall_time,ceil(min(area(:,1)))-1];
wall_2=[wall_time,ceil(max(area(:,1)))];
grid on
hold on
if ~strcmp(dist,'no wall')
    plot([wall_1(1),wall_2(1)],[wall_1(2),wall_2(2)],'--g',
'Linewidth', 1);
end
axis([0,inf,-50000,50000])
savefig([carp{1,2},'10_area1_t_C',num2str(cam),'.fig']);
saveas(gcf,[carp{1,2},'10_area1_t_C',num2str(cam),'.png']);
hold off
box on
plot(time,area(:,2),'.k');
hold on
title('$$Area2~vs~time$$','Interpreter','latex');
ylabel('$$Area~(mm^2)$$','Interpreter','latex');
xlabel('$$Time~(s)$$','Interpreter','latex');
wall_1=[wall_time,ceil(min(area(:,2)))-1];
wall_2=[wall_time,ceil(max(area(:,2)))];
grid on
hold on
if ~strcmp(dist,'no wall')
    plot([wall_1(1),wall_2(1)],[wall_1(2),wall_2(2)],'--g',
'Linewidth', 1);
end
savefig([carp{1,2},'10_area2_t_C',num2str(cam),'.fig']);
saveas(gcf,[carp{1,2},'10_area2_t_C',num2str(cam),'.png']);
```

```
figure(12)
box on
plot(time,eps(:,1),'.k');
title('$$Deformation~vs~time$$','Interpreter','latex');
ylabel('$$Epsilon1~(\varepsilon)$$','Interpreter','latex');
xlabel('$$Time~(s)$$','Interpreter','latex');
wall_1=[wall_time,0];
wall_2=[wall_time,(max(eps(:,1))+0.05)];
hold on
if ~strcmp(dist,'no wall')
    plot([wall_1(1),wall_2(1)],[wall_1(2),wall_2(2)],'--g',
'Linewidth', 1);
end
grid on
savefig([carp{1,2},'11_epsilon1_t_C',num2str(cam),'.fig']);
saveas(gcf,[carp{1,2},'11_epsilon1_t_C',num2str(cam),'.png']);
hold off
box on
plot(time,eps(:,2),'.k');
title('$$Deformation~vs~time$$','Interpreter','latex');
ylabel('$$Epsilon2~(\varepsilon)$$','Interpreter','latex');
xlabel('$$Time~(s)$$','Interpreter','latex');
wall_1=[wall_time,0];
wall_2=[wall_time,(max(eps(:,2))+0.05)];
hold on
if ~strcmp(dist,'no wall')
    plot([wall_1(1),wall_2(1)],[wall_1(2),wall_2(2)],'--g',
'Linewidth', 1);
end
grid on
savefig([carp{1,2},'11_epsilon2_t_C',num2str(cam),'.fig']);
saveas(gcf,[carp{1,2},'11_epsilon2_t_C',num2str(cam),'.png']);

hold off
close all
end
```

B.3. Routine for horizontal velocity filtering

```
% moving average filter
% first open figures 2, 5 and 7 and load data cent, time
carp='C:\Users\cecil\Google
Drive\copia_seg_HDD\Cámara\IMAGES\T11\4D\vid_5_C1\';
x=cent(:,1);
y=cent(:,2);
windowSize = 100;
b = (1/windowSize)*ones(1,windowSize);
a = 1;
xf = filter(b,a,x);
X=x'./(d*1000);
Y=y'./(d*1000);
```

```
XF=xf'./(d*1000);
figure(1)
hold on
plot(XF,Y,'.r')
legend('Input Data','Wall','Wall position','Filtered Data')
savefig([carp,'02_traj_FILTERED_C',num2str(cam),'.fig']);
saveas(gcf,[carp,'02_traj_FILTERED_C',num2str(cam),'.png']);
velxF=gradient(xf',1/fps);
figure(2)
hold on
plot(time,velxF,'.r')
legend('Input Data','Wall position','Filtered Data')
savefig([carp,'05_vel_x_t_FILTERED_C',num2str(cam),'.fig']);
saveas(gcf,[carp,'05_vel_x_t_FILTERED_C',num2str(cam),'.png'])
;
accxF=gradient(velxF',1/fps);
figure(3)
hold on
plot(time,accxF,'.r')
legend('Input Data','Wall position','Filtered Data')
savefig([carp,'07_acc_x_t_FILTERED_C',num2str(cam),'.fig']);
saveas(gcf,[carp,'07_acc_x_t_FILTERED_C',num2str(cam),'.png'])
;
close all
```